

Electrospun Nanofibers with Tunable Electrical Conductivity

by

Yuxi Zhang

B.S., Chemical Engineering & B.S., Materials Science and Engineering,
University of California at Berkeley, 2007
M.S., Chemical Engineering Practice, Massachusetts Institute of Technology, 2010

SUBMITTED TO THE DEPARTMENT OF CHEMICAL ENGINEERING IN PARTIAL
FULFILLMENT OF THE REQUIREMENTS FOR THE DEGREE OF

DOCTOR OF PHILOSOPHY

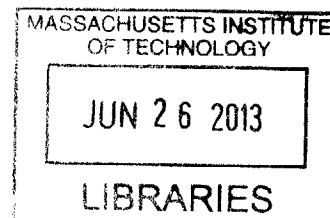
AT THE

MASSACHUSETTS INSTITUTE OF TECHNOLOGY

May 2013

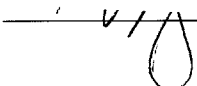
©2013 Yuxi Zhang. All Rights Reserved

ARCHIVES



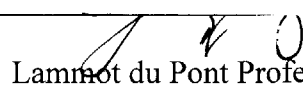
The Author hereby grants to MIT permission to reproduce and to distribute publicly paper and electronic copies of this thesis document in whole or in part in any medium now known or hereafter created.

Signature of Author



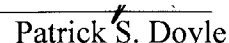
Department of Chemical Engineering
May 2013

Certified by



Gregory C. Rutledge
Lamont du Pont Professor of Chemical Engineering
Thesis Supervisor

Accepted by


Patrick S. Doyle
Professor of Chemical Engineering
Chairman, Committee for Graduate Students

Electrospun Nanofibers with Tunable Electrical Conductivity

by

Yuxi Zhang

Submitted to the Department of Chemical Engineering on May 23rd, 2013

in Partial Fulfillment of the Requirements for the Degree of

DOCTOR OF PHILOSOPHY

Abstract

Electrospinning is a convenient method to produce nanofibers with controlled diameters on the order of tens to hundreds of nanometers. The resulting nonwoven fiber mats are light-weight, highly porous, and have high specific surface areas around 1 to 100 m²/g. Combined with the high electrical conductivity of intrinsically conductive polymers, conductive electrospun fiber mats are promising for a variety of applications, such as multifunctional textiles, resistance-based sensors, flexible reversibly hydrophobic surfaces, organic photovoltaics, scaffolds for tissue engineering, and conductive substrates for surface functionalization and modification.

Intrinsically conductive polymers, such as polyaniline (PAni), however, are relatively hard to process compared to most other polymers. They have fairly rigid backbones due to the high aromaticity, and are usually available only in relatively low molecular weight forms, so that the elasticity of their solutions is insufficient for it to be electrospun directly into fibers.

Considerable amount of recent work has been reported trying to make electrospun polymeric nanofibers with intrinsically conductive polymers or composites. However, a large fraction of the work only showed the morphology and did not characterize the actual performance of these fibers, nor did they test the variability of the fibers and mats from a wide range of processing conditions and resulting structures. Therefore, this thesis aims to make a comprehensive study of the electrical tunability of electrospun fibers with intrinsically conductive polymers and its composites, to establish a clear processing-structure-property relationship for these fibers and fiber mats, and to test the resultant fibers with the targeted applications such as gas sensing.

We have first developed a reliable method to characterize fiber electrical conductivity using interdigitated electrodes (IDE) and high-impedance analyzers with contact-resistance corrections, and applied to electrospun conductive polymer nanofibers. This method was shown to be reliable and sensitive, as opposed to some of the other methods that have been reported in literature.

Facing with the challenge of overcoming the relatively low elasticity of the conductive polymer solutions to achieve electrospinnability, we have fabricated electrospun fibers of PAni and poly(3,4-ethylenedioxythiophene) (PEDOT), blended with poly(ethylene oxide) (PEO) or poly(methyl methacrylate) (PMMA) over a range of compositions. Pure PAni (doped with (+)-camphor-10-sulfonic acid (HCSA)) fibers were successfully fabricated for the first time by co-

axial electrospinning and subsequent removal of the PMMA shell by dissolution. This allowed for the pure electrospun PANi/HCSA fibers to be tested for electrical performances and its enhancement as well as gas sensing application.

The conductivities of the PANi-blend fibers are found to increase exponentially with the weight percent of doped PANi in the fibers, to as high as 50 ± 30 S/cm for as-electrospun fibers of 100% PANi/HCSA. This fiber conductivity of the pure doped PANi fibers was found to increase to 130 ± 40 S/cm with increasing molecular orientation, achieved through solid state drawing. The experimental results thus support the idea that enhanced molecular alignment within electrospun fibers, both during the electrospinning process and subsequent post-treatment, contributes positively to increasing electrical conductivity of conductive polymers. Using a model that accounts for the effects of intrinsic fiber conductivity (including both composition and molecular orientation), mat porosity, and the fiber orientation distribution within the mat, calculated mat conductivities are obtained in quantitative agreement with the mat conductivities measured experimentally. This correlation, along with the reliable method of fiber conductivity measurement by IDE, presents a way to resolve some of the inconsistencies in the literature about reporting electrical conductivity values of electrospun fibers and fiber mats.

Pure PANi fibers with different levels of doping were also fabricated by co-axial electrospinning and subsequent removal of the shell by dissolution, and shown to exhibit a large range of fiber electrical conductivities, increasing exponentially with increasing ratio of dopant to PANi. These fibers are found to be very effective nanoscale chemiresistive sensors for both ammonia and nitrogen dioxide gases, thanks to this large range of available electrical conductivities. Both sensitivity and response times are shown to be excellent, with response

ratios up to 58 for doped PAni sensing of ammonia and up to more than 10^5 for nitrogen dioxide sensing by undoped PAni fibers. The characteristic times for the gas sensing are shown to be on the order of 1 to 2 minutes. We have also developed a generic time-dependent reaction-diffusion model that accounts for reaction kinetics, reaction equilibrium, and diffusivity parameters, and show that the model can be used to extract parameters from experimental results and used to predict and optimize the gas sensing of fibers under different constraints without the need to repeat experiments under different fiber and gas conditions.

Thesis Supervisor: Gregory C. Rutledge
Lammot du Pont Professor of Chemical Engineering

Thesis Committee Members:

Karen K. Gleason
Alexander and I. Michael Kasser Professor of Chemical Engineering

T. Alan Hatton
Ralph Landau Professor of Chemical Engineering
Director, David H. Koch School of Chemical Engineering Practice

Harry L. Tuller
Professor of Ceramics and Electronic Materials in Materials Science and Engineering
Director, Crystal Physics and Electroceramics Laboratory

Acknowledgments

I sincerely thank my advisor, Prof. Rutledge, for all the guidance, insights, and encouragements over the years. I want to also thank the other thesis committee members, Prof. Gleason, Prof. Hatton, Prof. Tuller, and Prof. Thomas, for their valuable input and helpful interactions over the course of this thesis work. Prof. V. Bulovic and Prof. S. Kim have also provided helpful insights in the early stages of the work.

I want to thank all Rutledge group members, past and present, namely Dr. Minglin Ma, Dr. Chia-Ling Pai, Dr. P.K. Bhattacharjee, Simon Choong, Dr. Matthew M. Mannarino, Xianwen Mao, Dr. Keith Forward, Dr. Jason Lee, Dr. Jung Ah Lee, Dr. Ying Yang, Dr. Indrani Bhattacharyya, Dr. Peng Yi, Dr. Liang Chen, Dr. Junmo Kim, Dr. Saptarshi Chattopadhyay, Dr. Sang Il Han, Dr. Fei Guo, Alex Bourque, David Nicholson, Wenda Tian, Dr. Erik Allen, Dr. Joe Lowery, Dr. Jian Yu, Dr. Sezen Buell, Dr. Ateeque Malani, Pedja D. Djuranovic, Dr. Sanghun Lee, Dr. Miguel Amat, and Dr. Vikrum K. Kuppa, for their support and company over all these years. I would also like to thank Dr. George Whitfield, Dr. Woo-chul Jung, Di Chen, Jaejin Kim, Dr. Sriram Vaddiraju, Dr. Miles Barr, Dr. Jingjing Xu, Dr. Dhiman Bhattacharyya, Dr. Asli Katmis, Dr. Steve Kooi, Dr. William DiNatale, Dr. Alex Hsieh, Dr. Andrea Centrone, Kittipong Saetia, Dr. Heon Ju Lee, Stephen P. Bathurst, Garrett Bruer, and everyone else who have helped me in one way or another in this thesis work.

I would like to express my gratitude to all my friends and family who have supported me all along, and to the funding from Institute for Soldier Nanotechnologies (ISN), under US Army contract ARO W911NF-07-D-0004.

Table of Contents

List of Figures	10
List of Tables	14
Chapter 1 Introduction.....	15
1.1 Electrospinning.....	15
1.2 Conductive Polymers	18
1.3 Motivation	21
1.4 Thesis Overview.....	26
Chapter 2 Characterization	27
2.1 Morphological and Structural Characterization	27
2.2 Electrical Conductivity Characterization	30
2.2.1 Four-point Probe	30
2.2.2 Interdigitated Electrodes	32
2.2.3 Contact Resistance Correction.....	35
2.2.4 Mat Electrical Conductivity Measurement	37
Chapter 3 Production of Electrospun Fibers.....	39
3.1 Fibers from Polymer Blends	41
3.2 Fibers by Coaxial Electrospinning	47
3.3 Fibers with Surface Coating	54

Chapter 4	Electrical Conductivities of Fibers and Mats.....	59
4.1	Conduction in Conductive Polymer Fibers.....	59
4.2	Experimental Fiber Electrical Conductivities.....	62
4.3	Electrical Conductivity and Molecular Orientation within Fibers.....	66
4.4	Mat Conductivity – Fiber Conductivity Correlations.....	69
4.4.1	Experimental Mat Electrical Conductivity.....	69
4.4.2	Mat Porosity.....	71
4.4.3	Fiber Orientation in Fiber Mats.....	71
4.4.4	Fiber Orientation Distribution Calculation.....	75
4.4.5	Mat-Fiber Conductivity Parity Plot & Discrepancies.....	77
Chapter 5	Gas Sensing by Electrospun Fibers.....	79
5.1	Gas Sensing Tests.....	79
5.2	Sensitivities and Response Times.....	82
5.2.1	Ammonia Sensing.....	82
5.2.2	Nitrogen Dioxide Sensing.....	87
5.3	Reaction-Diffusion Model for Gas Sensing by Fibers.....	91
5.3.1	Reaction Equilibrium.....	91
5.3.2	Response as a Function of Radial Electrical Conductivities.....	92
5.3.3	Time-Dependent Reaction-Diffusion Model.....	93
5.3.4	Equilibrium Determination from Steady-State Data.....	98
5.3.5	Application of the Model for Design Optimization.....	103

Chapter 6	Conclusions and Recommendations	109
6.1	Conclusions	109
6.2	Recommendations	112
Bibliography	114

List of Figures

Figure 1 Schematics of Typical Electrospinning Setup	16
Figure 2 Representative Scanning Electron Microscope Images of Electrospun Poly(trimethyl hexamethylene terephthalamide) (PA 6(3)T) Fibers with Different Fiber Diameters	17
Figure 3 Structures of Selected Intrinsically Conductive Polymers	18
Figure 4 Structures of Different Forms of PANi	20
Figure 5 Four-point Probe Setup.....	31
Figure 6 (a) Illustration of the interdigitated electrodes (IDE) and a magnified view of the fingers; (b) optical microscope image of electrospun PANi-PEO blend fibers deposited on IDE and hot-pressed	33
Figure 7 Typical Nyquist plot obtained from the Solartron impedance analyzer (for an aligned fiber sample of PANi-PMMA blend fibers with 7.7 wt% of PANi)	34
Figure 8 Sample Plot to Extrapolate the Contact Resistances from Measurements on Interdigitated Electrodes of Different Finger Spacings	36
Figure 9 Flow chart illustrating how material properties, processing parameters, and processing conditions affect the resultant fibers	40
Figure 10 Molecular structure of HCSA, one of the most efficient dopants for PANi	42
Figure 11 SEM images of PANi-PEO blend electrospun fibers with 11 wt% PANi in blend (left) and 20 wt% PANi in blend (right), PEO $M_w = 1,000,000$; taken under $2,500\times$ magnification (scale bar = $10\ \mu\text{m}$)	43
Figure 12 Structure of PEDOT-PSS Macromolecular Salt	46
Figure 13 Schematic of coaxial electrospinning and resultant core-shell jets	48
Figure 14 SEM images of electrospun PANi-PMMA core-shell fibers before (left) and after (right) dissolution of PMMA by isopropyl alcohol; taken under $12,000\times$ magnification (scale bar = $1\ \mu\text{m}$).....	49

Figure 15 DSC Results of (a) core-shell PANi fibers after removing shell; (b) pure PANi; (c) pure PMMA; (d) pure dopant HCSA; all measured between -40 and 160 °C and the horizontal axes are all from -50 and 200 °C.....	52
Figure 16 SEM images of electrospun PANi/HCSA fibers with different molar ratios of HCSA to PANi: [HCSA]/[PANi] = 0 (a); 0.5 (b); 0.75 (c); and 1.0 (d). All images taken after dissolution of PMMA shell and using 7,500× magnification (scale bar = 2 μm)	53
Figure 17 SEM image of electrospun polycaprolactone (PCL) fibers after in-situ solution polymerization with pyrrole and iron(III) chloride to form polypyrrole coatings.....	55
Figure 18 SEM images (scale bar 1μm, 10,000× magnification) of (a) as-electrospun PA 6(3)T fibers; (b) PA 6(3)T fibers CVD coated for 10min; (c) PEO fibers CVD coated for 5min; (d) PEO fibers CVD coated for 10min; all coatings were done at 80°C with PEDOT	56
Figure 19 SEM Image of Electrospun Polycaprolactone Fibers after Coating by Layer-by-layer Deposition.....	57
Figure 20 Typical dependence of electrical conductivity (logarithm) on conductive filler volume content	61
Figure 21 Electrical conductivity of as-electrospun polyaniline fibers (nominally doped with an equimolar amount of HCSA) as a function of the weight fraction of PANi in the blended fibers; the pure PANi fiber was obtained after dissolving the shell component (PMMA) of the core-shell fibers	62
Figure 22 (a) Illustration of molecular orientation of polyaniline in fibers; (b) polarized-FTIR result for PANi fibers stretched to a strain of 0.72, with parallel spectrum in grey and perpendicular spectrum in black	67
Figure 23 Electrical conductivity of the pure polyaniline fiber, as-spun and after solid-state drawing, as a function of molecular orientation within the fibers, as measured by polarized FTIR from aligned fiber bundles; the label next to each data point shows the corresponding nominal strain.....	68
Figure 24 Mat electrical conductivity of polyaniline fiber mats (as-electrospun, nominally doped with an equimolar amount of HCSA) as a function of the PANi weight fraction in the blended fibers; the pure PANi fiber mat was obtained after dissolving the shell component (PMMA) of the core-shell fibers.....	70
Figure 25 Definition of fiber orientation angle θ between across two electrodes with width L , separated by a gap δ . X denotes the position where the fiber makes contact with one of the	

electrodes. $\theta_{LB}(x)$ and $\theta_{UB}(x)$ denote the upper and lower bounds in orientation angle, beyond which a fiber located at position x does not make contact with the second electrode.....	73
Figure 26 Orientation correction factor for mat conductivity as a function of the measurement geometry (ratio of electrode length to electrode separation), assuming a uniform angular distribution of fibers in the plane of the mat.....	75
Figure 27 Correlation between dimensionless conductivity ratio (mat to fiber) and orientation distribution of fibers in the mat for samples with 20 wt% PANi blended with PEO. The insets show histograms of the angular orientation distribution for each sample from SEM image analysis. For each inset, the abscissa ranges from -90° to 90° , while the ordinate goes from 0 to 12000 counts	76
Figure 28 Parity plot of the experimentally-observed mat conductivity versus that calculated by the model for PANi-blend and PANi fibers	78
Figure 29 Illustration of gas sensing apparatus, including the tube furnace, the location of the interdigitated electrodes (IDE) (zoomed in), the mass flow controllers (MFC), the computer for LabView control and data collection and analyzer interface.....	80
Figure 30 Time response of drawn PANi fiber (450nm in diameter) under cyclic exposure of 500ppm of ammonia; superimposed line indicates the change in ammonia concentration from 0 to 500ppm	83
Figure 31 Time response of as-spun doped PANi fiber to different concentrations of NH_3 ; dotted line shows the change in NH_3 concentrations.....	85
Figure 32 Resistance modulation upon exposure of doped electrospun PANi fibers to different concentrations of ammonia gas.....	86
Figure 33 Time response of undoped PANi fiber to different concentrations of NO_2 ; dotted line shows the change in NO_2 concentrations.....	88
Figure 34 Resistance modulation upon exposure of undoped electrospun PANi fiber to different concentrations of NO_2 gas	90
Figure 35 Results of reaction-diffusion model showing the ratio of initial resistance to final resistance as a function of Damköhler number (Da) and dimensionless time (τ) for selected values of equilibrium constant (K). Calculations assume that no gaseous reactant or products are present in the fibers as the initial condition, and the conductivity of the fiber decreases linearly with the concentration of the reactant Φ	96

Figure 36 Equilibrium fraction of PANi doped (after partial dedoping by the gas) in the fibers derived from sensing responses at different ammonia concentrations 99

Figure 37 Comparison of experimental and fitted data for both as-spun and solid-drawn doped PANi fibers upon ammonia exposure with concentrations ranging from 10 to 700ppm 102

Figure 38 Reaction-diffusion model results at $K = 1.5$ using the experimental NH_3 sensing parameters; (a) a plot of resistance ratios as a function of τ for Da ranging from 10^{-4} to 10^2 ; (b) a plot of resistance ratios as a function of Da for τ ranging from 0 to 20 (increment of 0.5), the open and closed dots indicates the locations of the 620nm fiber and 450 nm fiber at $t = 60\text{s}$ respectively, and the arrows indicate the optimization directions. 108

List of Tables

Table 1 Conductivity Ranges of Common Materials.....	22
Table 2 Electrospun Conductive Polymers and Blends Previously Reported in Literature.....	23
Table 3 Processing conditions and fiber diameters of PANi-blend fibers	44
Table 4 Processing conditions and fiber diameters of PEDOT-blend fibers	45
Table 5 XPS Results showing Surface Compositions of Core-Shell Electrospun Fibers before and after Dissolution of Shell	50
Table 6 Diameter and Conductivity of As-spun PANi/HCSA Fibers after Removing Shell	64
Table 7 Electrical Conductivities of PANi Fibers after Stretching.....	65
Table 8 Characteristic Response Times of As-Spun and Solid-State-Drawn PANi/HCSA Fibers during Ammonia Exposure and Nitrogen Purge.....	84
Table 9 Characteristic Response Times of Undoped PANi Fibers during NO ₂ Exposure and Purge	89

Chapter 1 Introduction

1.1 Electrospinning

Electrospinning is a convenient method to produce nanofibers with controlled diameters on the order of tens to hundreds of nanometers.¹ The process involves the generation of a high electric field, on the order of 1 kV/cm, between a polymer fluid in a syringe with a capillary tip and a collector.² When the voltage reaches a critical value, the charge overcomes the surface tension of the polymer solution, and a jet is produced. The jet undergoes continuous stretching as it accelerates downfield toward the collector, thinning further at a very high strain rate, on the order of 1000 upon the onset of the whipping instability. Because of the high elasticity of the polymer solution, the electrically-charged jet is continuous as Rayleigh instability is suppressed, and undergoes a stretching and whipping process.³ A non-woven mat of fibers is thus deposited on the collector after the evaporation of the solvent. A schematic of the process is shown in Figure 1. The setup consists of a high-voltage power supply, a polymeric fluid supply pumped usually by a syringe pump, one high potential electrode and one collector electrode.

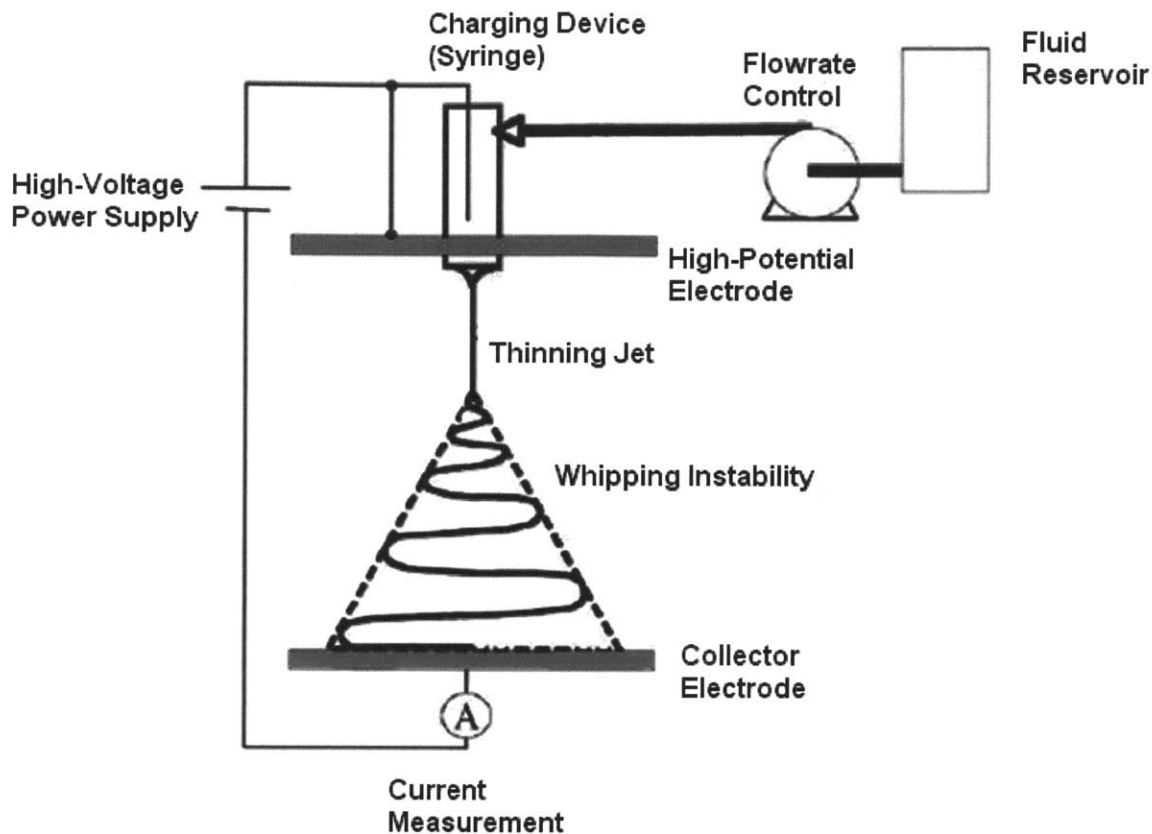


Figure 1 Schematics of Typical Electrospinning Setup^{4 5}

The resulting nonwoven fiber mats are light-weight and highly porous. The fibers in the mats have diameters in a controlled range from nanometers to micrometers, as demonstrated in scanning electron microscope images in Figure 2, and have high specific surface areas, around 1 to 100 m²/g. The balance between surface tension and charge repulsion at the jet surface has been used to explain the ultimate diameter of the fibers.⁶ The large surface area holds the promise of using these nanofibers for a variety of applications, such as highly sensitive sensors,⁷

efficient catalysts,⁸ high-performance filters,⁹ scaffolds for tissue engineering,¹⁰ superhydrophobic surfaces,¹¹ multifunctional textiles,¹² flexible reversible surfaces,¹³ organic photovoltaics,¹⁴ and substrates for surface functionalization and modification.¹⁵

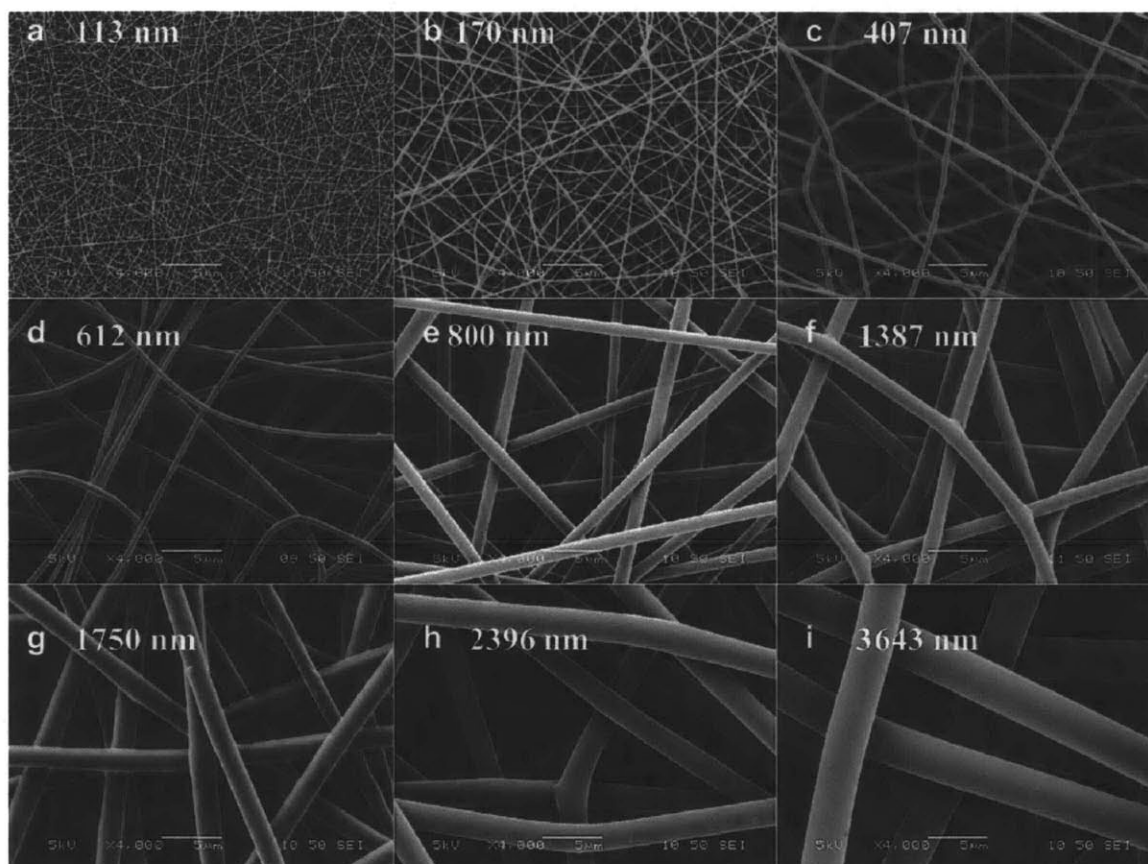


Figure 2 Representative Scanning Electron Microscope Images of Electrospun Poly(trimethyl hexamethylene terephthalamide) (PA 6(3)T) Fibers with Different Fiber Diameters¹⁶

1.2 Conductive Polymers

As most polymers are insulating, intrinsically conductive polymers (ICP) stand out for their unusual electrical properties, and have been a keen area of research interest for several decades.^{17 18} Common classes of ICP's include polyaniline (PAni), polypyrrole (PPy), polythiophene (PT), and polyacetylene (PA). Figure 3 shows some structures of ICP's.

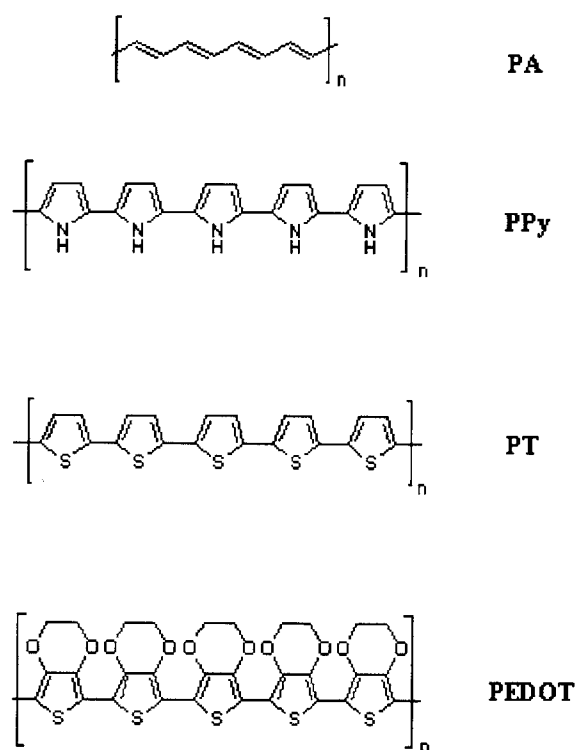
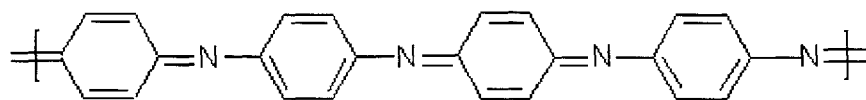
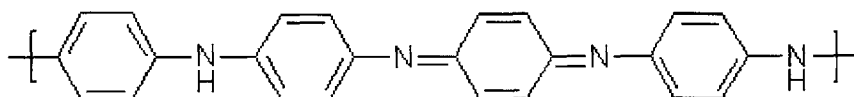


Figure 3 Structures of Selected Intrinsically Conductive Polymers

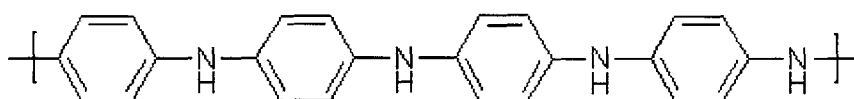
They typically have conjugated π -orbital structures, and can be doped, either chemically or electrochemically, from the insulating state through the semiconducting state to the metallic state. They can also be de-doped through these states, reversibly in many cases.¹⁹ During the doping and de-doping process, electrical properties are modulated. In most cases, doping occurs by partial oxidation of the π backbone system of the polymer.²⁰ Treatment of the polymer with vapors or solutions of oxidizing agents can readily accomplish doping and make the polymers conductive. In some cases such as polyaniline (PAni), doping can also take place simply by protonation of the emeraldine state of the polymer by vapors or solutions of acids. De-doping occurs equally simply from deprotonation by vapors or solutions of bases. Thus, these conducting polymers are likely to be highly sensitive to a variety of changes in the environment. Figure 4 shows the structures of different forms of PAni, which exhibits different electrical characteristics.



pernigraniline



emeraldine



leucoemeraldine

Figure 4 Structures of Different Forms of PANi

1.3 Motivation

Among all the interesting applications of electrospun fiber mats, quite a number of them call for the need to design nanofibers whose electrical conductivity can be tuned and modulated within the practical range of sensitivity.

Along with the research interest in the Institute for Soldier Nanotechnologies (ISN), one of the most discussed is to make multifunctional textiles that can serve as building blocks for clothing and other gear to provide soldier protection and survivability. This means that the fibers should be able to sense the changes in the environment (e.g. change in temperature, change in pH, physical damage, radiation, presence of certain gases or chemicals) and communicate signals through the fibers, i.e., to act as conductive molecular wires using resistance-based sensing.

Table 1 shows the conductivity ranges of a few common materials. Though metals undoubtedly have the highest conductivity, a common theme among the various applications is that they do not necessarily need the highest conductivity possible. Rather, they mostly require the conductivity to be tunable and capable of being modulated. While different applications require different conductivity ranges, it is generally desirable for sensors to have greater changes in conductivity when modulated but still maintain a high enough conductivity at base level for signals to be transduced.²¹ For most other applications, a conductivity of 100 to 1000 S/cm is sufficient, and usually higher conductivities in the range are desirable. However, they also rely on the material to be light-weight and flexible for the applications to be feasible, so the bulk of

the fibers should still be polymeric, and this usually presents an upper bound on the practical range of electrical conductivities achievable for these applications.

Table 1 Conductivity Ranges of Common Materials

Material	Conductivity (S/cm)
Metals	$\sim 10^5$
Carbon Black	~ 300
Conductive Polymers (Bulk Film) ²²	1 to 1500
Drinking Water	$\sim 10^{-2}$
Semiconductors	10^{-5} to 10^{-2}
Non-conductive Polymers (Bulk Film)	10^{-16} to 10^{-9}
Glass	10^{-16} to 10^{-12}

Therefore, conductive polymers and their composites are the most suitable candidates to produce electrospun fibers with tunable electrical conductivities.

Considerable amount of work has been reported recently trying to make electrospun polymeric nanofibers with conductive polymers or composites with conductive or semiconducting nanoparticles.²³ However, a large fraction of them only showed the morphology and did not characterize the actual performance of these fibers, as shown in a summary in Table 2. Careful consideration was not given to characterize electrical conductivities accurately.

Many of them also did not attempt to test the range of tunability in this kind of electrospun fibers.

For those who actually reported conductivity values (mostly fibers with conductive polymers blended with non-conductive polymers),^{24 25 26 27} the values are much lower (10^{-5} to 1 S/cm) than films that can be made without electrospinning (1 to 200 S/cm).²⁸

Table 2 Electrospun Conductive Polymers and Blends Previously Reported in Literature

System	Electrospun by	Conductivity Range (S/cm)	Comments
PAni in Sulfuric Acid	Reneker & Chun (1996)	~0.1	Conductivity estimated; Sensitive to the nature of PAni used
PAN coated with PPy	Huang et. al. (1997)	Not reported	In-situ solution polymerization on PAN fibers
PAni blend with PEO	Norris et.al. (2000)	$5 \times 10^{-4} \sim 0.1$	
PMMA coated with PAni	Dong et. al. (2004)	0.3	In-situ solution polymerization on PMMA fibers; Single value of conductivity
PAni-PS, PAni-PC, PAni-PEO blends	Wei et. al. (2005)	$4.1 \times 10^{-14} \sim 2.4 \times 10^{-13}$	Very low conductivities
PET coated with PAni	Kim & Dufour (2005)	Not reported	Sol-gel coating; only reported resistance
PAni-PS film	Zhu et. al. (2006)	$1.0 \times 10^{-5} \sim 1.4 \times 10^{-6}$	Film only, not electrospun
PPy blend with PEO	Chronakis et.al (2006)	$4.9 \times 10^{-8} \sim 1.2 \times 10^{-5}$	Low conductivities
PAni-PEO blend	Pinto et. al. (2007)	Not reported	Only mentioned resistance change to alcohol vapor exposure
PAni-PVP blend	Bishop-Haynes & Gouma	Not reported	Only mentioned resistance change to humidity and NO ₂ exposure

	(2007)		
PAni-PEO blend	Attout et.al. (2008)	Not reported	Only morphological studies
P3HT-PEO blend	Laforgue & Robitaille (2008)	1.0×10^{-3} ~0.30	
PAni blend with Poly(D,L-lactide)	McKeon et.al (2009)	0.0437	Only one blend ratio gave measurable conductivity
P3HT-Chloroform Core-Shell; P3HT-PCL blend	Lee et. al. (2009)	Not reported	Only morphological studies
PAni blend with PHB	Fryczkowski et.al. (2009)	Not reported	Only saying resistance level of 10^{-6} ohm
PMMA-P3HT Core- Shell	Kuo et.al. (2009)	1×10^{-6}	Single value of conductivity

Therefore, this thesis aims to make a comprehensive study of the electrical tunability of electrospun fibers with intrinsically conductive polymers and its composites, to establish a clear processing-structure-property relationship for these fibers and fiber mats, and to test the resultant fibers with the targeted applications such as gas sensing.

The objectives of the research were:

- (1) To establish a reliable and sensitive characterization method for the range of electrical conductivities applicable to the conductive electrospun nanofibers and nanoweb;

- (2) To investigate how different electrospinning methods and conditions affect the structure of the resulting fibers made with conductive polymers, through direct/core-shell electrospinning or with subsequent surface coatings;
- (3) To investigate the range of tunability of electrical conductivities of these intrinsically conductive polymer fibers;
- (4) To compare and contrast the properties of the fibers made using different approaches, and to investigate the applicability of combining some of the processing techniques.

1.4 Thesis Overview

This thesis is divided into six chapters. After the background and motivation that has already been presented in Chapter 1 so far, Chapter 2 is going to focus on the establishment of a reliable and sensitive characterization method for the all-important electrical conductivities of electrospun fibers and their porous mats, as well as to summarize the morphological and structural characterization methods utilized in the studies of the electrospun fibers and mats. Chapter 3 is discussing the various production methods used, including electrospinning from polymer blend solutions, coaxial electrospinning, and surface coating of electrospun fibers with conductive polymers, and showing how these methods require controlled processing conditions and result in different fiber structures. Chapter 4 presents the results and trends of electrical conductivities of these fibers, in both fiber conductivity and mat conductivity forms, and also proposes a model that permits the calculation of mat conductivity as a function of fiber conductivity, mat porosity and fiber orientation distribution. Chapter 5 centers on the application of the electrospun fibers as potent chemiresistive gas sensors, and presents a time-dependent reaction-diffusion model that can be used to extract physical parameters and to determine the optimal material design for the gas sensing application. The thesis then concludes in Chapter 6 with also recommendations for future work.

Chapter 2 Characterization

2.1 Morphological and Structural Characterization

As is common for features on the order of micrometers and below, the general features of electrospun fiber mat were observed under scanning electron microscope (SEM) directly. For the procedure, a small piece of the fiber or fiber mat sample was taped onto a double-sized copper tape and then sputter-coated with a layer of gold, about 2 to 3 nm in thickness, for imaging, using a Desk II sputter unit (Denton Vacuum LLC). The layer of gold coating by sputtering is needed if the sample is not conductive. The models JEOL JSM-6060, 6010LA, and 6700 (JEOL Ltd., Japan) were all used in the studies of fiber surface structures. Magnifications up to 20,000× have been used, and the resolution of the SEMs is about 10 nm for the smallest features.

The internal structures and surface layers of the fibers were inspected directly under transmission electron microscope (TEM). For lateral view, fibers were deposited directly onto the copper grid; for cross-sectional views of the fibers, they were embedded in epoxy resin and cut into slices of 60 to 100 nm thickness by cryo-microtome technique. The TEM being used is a JEOL 200CX and the Cryo-microtome is of Leica EM UC6 model.

Optical microscopy (Zeiss Axioskop2 MAT with AxioCam HRc) was also used to observe the optical images of the samples under a much smaller magnification than SEM or

TEM, up to 200×. This was done to observe the entirety of the samples as prepared, on certain substrates which are not easy to be observed under SEM or TEM. Although this cannot provide detailed structural information of the fibers, the optical microscope images are very useful for checking the alignment of fibers on substrates, and for analyzing samples where the number of fibers or fiber segments is important for calculation.

X-ray photoelectron spectroscopy (XPS, Physical Electronics Versaprobe II) was used to determine surface elemental composition of the fibers, and to further deduce the fiber structure as a result of processing based on elemental balances of all known components in the fiber. XPS spectra are obtained by irradiating a material with a beam of X-rays while simultaneously measuring the kinetic energy and number of electrons that escape from the surface of the material being analyzed. As such, XPS generally probes only the approximately top 10 nm of the surface of the samples, so it provides an accurate measure of the surface composition.

Differential scanning calorimetry (DSC, TA Instruments DSC Q1000) was used to characterize the heat capacity of the fiber samples, and to detect the presence or absence of fiber components based on their signature phase transition or glass transition temperatures.

Polarized Fourier-transformed infrared spectroscopy (polarized-FTIR, Thermo Fisher FTIR6700) was used to measure the molecular orientation of the polymer molecules within the electrospun fibers. Bundles of aligned fibers were used for this measurement. The dichroic ratio $D = A_{\parallel} / A_{\perp}$ where A_{\parallel} and A_{\perp} are the absorbance related to a signature infrared-absorption

active molecular mode measured with the incident beam polarized parallel and perpendicular to the fiber bundle axis, respectively. The overall molecular orientation, f , and the angle between the molecular axis and the fiber bundle axis, Ω , can be calculated from Eq. 1,²⁹

$$f = \frac{3\langle \cos^2 \Omega \rangle - 1}{2} = \frac{(D-1)(2 \cot^2 \alpha + 2)}{(D+2)(2 \cot^2 \alpha - 1)}, \quad (1)$$

where α is the angle between the molecular axis and direction of the bond being measured. Here, $f = 1$ represents perfect alignment of molecules along the fiber axis, $f = 0$ represents random orientation, and $f = -1/2$ represents molecular alignment perpendicular to the fiber axis.

The porosity of the electrospun fiber mats, ϕ , was estimated using Eq. 2. The mass of the mat (m_m) was weighed by a digital balance (Caley & Whitmore CP4202S). Fiber density values were obtained from literature.³⁰ w is the width of the sample, and t is the thickness of the mat measured by a digital micrometer (Mitutoyo CLM1) with a fixed force of 0.5 N.

$$\phi = 1 - \frac{m_m}{\rho_f \delta w t} \quad (2)$$

2.2 Electrical Conductivity Characterization

The research relied very heavily on being able to find a reliable and sensitive characterization method for the range of electrical conductivities applicable. To that end, careful consideration has been given to how to measure both the fiber electrical conductivity and mat electrical conductivity reliably, with contact-resistance and fiber alignment factors all considered. Because of its widespread use in the relevant literature, the four-point probe method was first evaluated, but was ultimately deemed inaccurate. A systematic method of depositing electrospun fibers onto interdigitated electrodes were instead used to measure fiber electrical conductivities.

2.2.1 Four-point Probe

Four-point probe is a very common method measuring the resistivity of semiconducting material. It consists of four equally-spaced metal tips (as shown in Figure 5). A high impedance current source is used to supply current through the outer two probes; a voltmeter measures the voltage across the inner two probes to determine the sample resistivity. The model used was Signatone S-302-4 with Keithley SCS-4200 current source. Its tips are made of tungsten carbide, and the spacing is 1 mm between adjacent tips.

For a thin sheet of material measured by four-point probe, Equation 3 can be used to calculate its electrical resistivity, ρ , with V and I being the measured voltage and imposed current, respectively.

$$\rho = \frac{\pi}{\ln 2} \left(\frac{V}{I} \right) \quad (3)$$

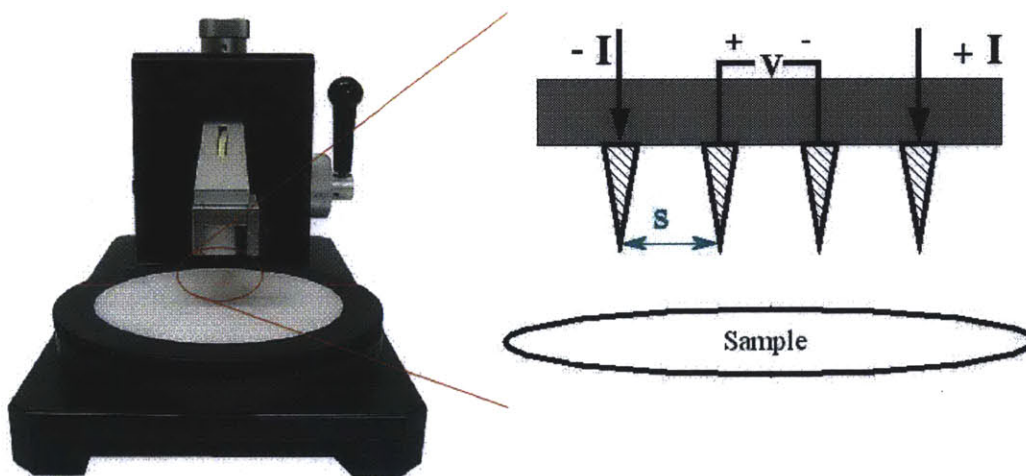


Figure 5 Four-point Probe Setup

The main difficulty when using four-point probe to measure electrical conductivities of electrospun fiber mat is that the four-point probe calculation assumes a thin film rather than a highly porous fiber network. The actual conducting paths can be much more tortuous and longer in the case of the latter, so the reported conductivity values could be much lower than the actual value for bulk films. In addition, the porosity and compressibility of the fiber mats make the

contact between the metal tips and fibers questionable and inconsistent from sample to sample and from one measurement to the next. There also seem to be a large uncertainty involved with the penetration depth (height) of the pins into the fiber mats. As a result, the experimental measurements presented huge error bars and inconsistencies from different repeats of the same material, some even giving negative resistivity values. This characterization method was thus not chosen, for its lack of accuracy and repeatability.

2.2.2 Interdigitated Electrodes

Instead of using four-point probe or simply a multimeter to measure the electrical conductivity of the electrospun fibers, a more systematic way of depositing fibers onto interdigitated electrodes was used for electrical conductivity characterization.

To determine the electrical conductivity of single electrospun fibers, aligned fibers were electrospun in between two parallel electrodes and then deposited onto interdigitated platinum electrodes (IDE, ABTech).^{31 32} The IDEs have 50 sets of interdigitated fingers, and finger width and spacing ranging from 5 to 20 μ m, as shown in Figure 6. After deposition, the fiber/IDE sample was hot-pressed at 200°C and 1 metric ton load for 10 seconds to ensure good electrical contact. A Solartron 1260/1287A high-impedance analyzer was used to measure the resistance between the two electrodes on the IDE. A typical Nyquist plot from the impedance analyzer is shown in Figure 7, where a semicircular trace in the plot shows both resistive and capacitive

behavior. The resistance value was read from the Nyquist plot as the extrapolated real-axis (horizontal) intercept at the lowest frequency.

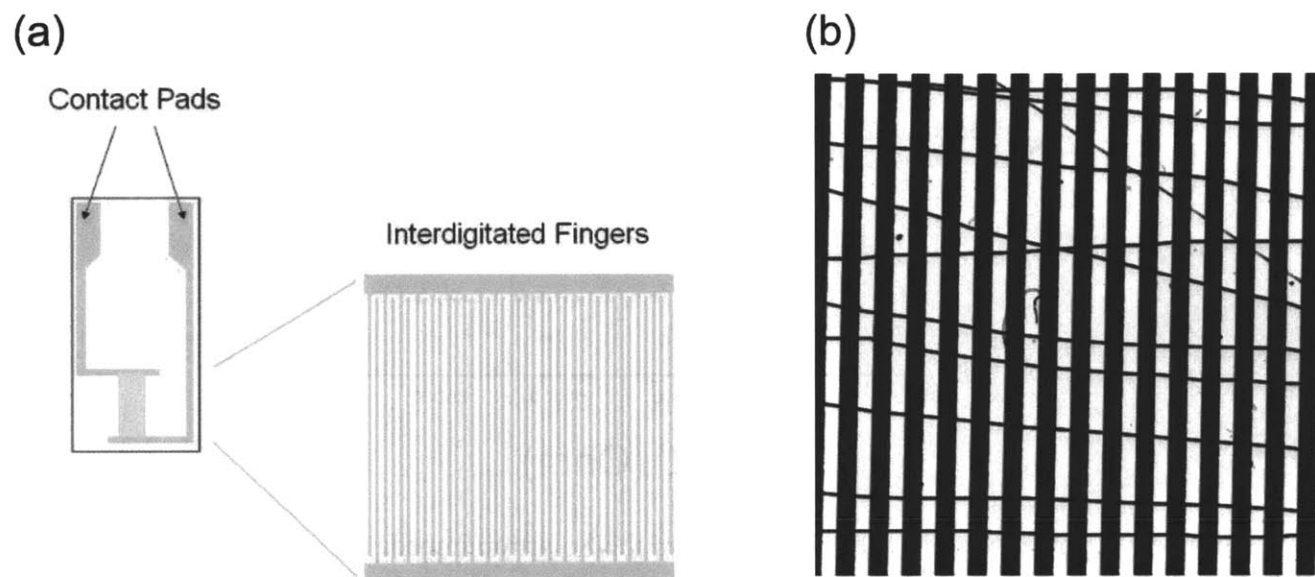


Figure 6 (a) Illustration of the interdigitated electrodes (IDE) and a magnified view of the fingers; (b) optical microscope image of electrospun PANi-PEO blend fibers deposited on IDE and hot-pressed

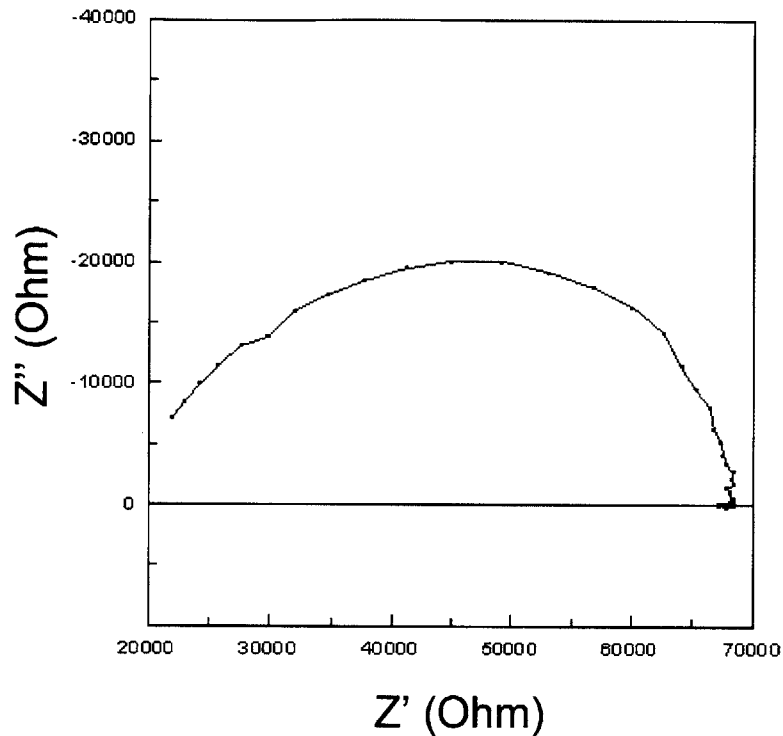


Figure 7 Typical Nyquist plot obtained from the Solartron impedance analyzer (for an aligned fiber sample of PANi-PMMA blend fibers with 7.7 wt% of PANi)

The average electrical conductivity (σ), which is the inverse of the electrical resistivity, can be calculated using Eq. 4, where R is the resistance measured on the IDE, N is the number of parallel pathways formed by fibers on the IDE bridging over the interdigitated fingers (which varies from sample to sample), estimated by optical microscopy, d is the average fiber diameter obtained by SEM on the as-spun fibers, and δ is the finger spacing (inter-electrode distance) of the IDE:

$$\sigma = \frac{4\delta}{\pi d^2 RN}. \quad (4)$$

2.2.3 Contact Resistance Correction

Assuming that the fiber segments act as resistances in parallel, the single-fiber resistance is $R_f = (RN)$. The correction for contact resistance between the fiber and electrode was obtained by measuring the resistance R for N fiber segments deposited under the same processing conditions on IDEs with different finger spacings (5, 10, 15, and 20 μm). Plotting the single-fiber resistance R_f versus the finger spacing and extrapolating the best linear fit (as determined by least squared residuals) to zero finger spacing δ , one obtains the contact resistance, R_{f0} . The uncertainty in R_{f0} was typically less than 20%, suggesting that the extrapolation method is reliable. When averaged to a single fiber segment, one eliminates the contribution caused by the different number of fibers (N) deposited on different electrodes. Figure 8 shows a typical plot used to extrapolate the contact resistance contributions.

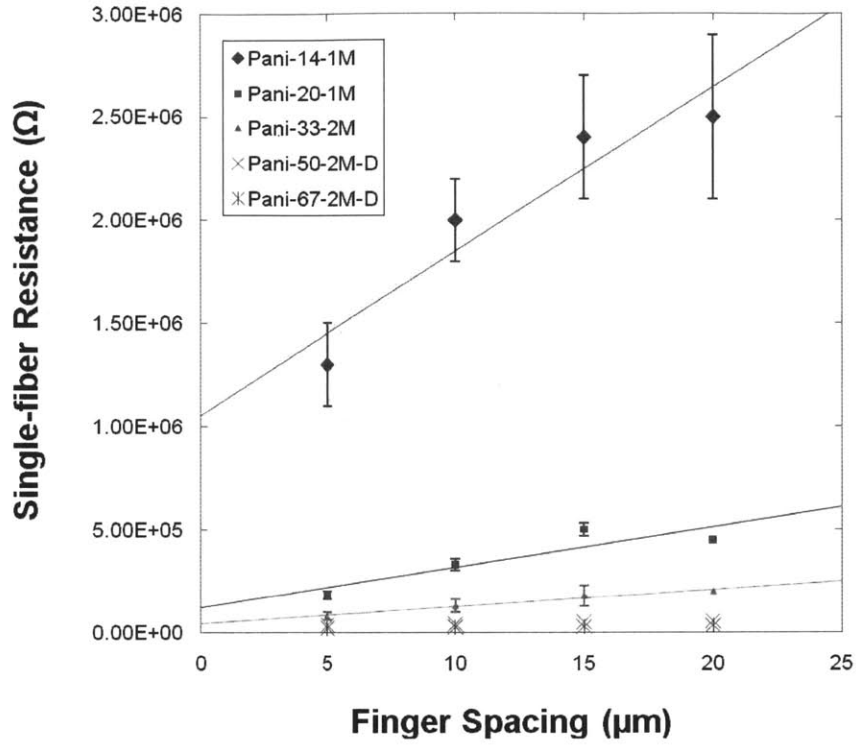


Figure 8 Sample Plot to Extrapolate the Contact Resistances from Measurements on Interdigitated Electrodes of Different Finger Spacings

This contact resistance was then subtracted from the total resistance to determine the fiber electrical conductivity, according to Eq. 5.

$$\sigma_f = \frac{4\delta}{\pi d^2 (R_f - R_{f0})} \quad (5)$$

2.2.4 Mat Electrical Conductivity Measurement

Electrical measurements were also performed on both randomly-oriented and aligned electrospun fiber mats. Electrospun fiber mats were cut into rectangular samples that were 2.0 cm in one dimension and various lengths (1.0, 1.5 or 2.0 cm) in the other dimension. The complex resistance between two strips of copper foil placed on the opposing 2.0 cm edges of the mat was measured by the impedance analyzer, so that the spacing between the two copper foils, δ , varied from 1.0 to 1.5 to 2.0 cm. The mat conductivity was calculated based on the geometry of the sample using Eq. 6, where σ_m is the mat conductivity, R is the measured resistance, w is the width of the sample (fixed at 2.0 cm in this study), and t is the thickness of the mat measured by a digital micrometer (Mitutoyo CLM1) with a fixed force of 0.5 N. The contact-resistance was again determined by plotting the measured resistance R versus the electrode spacing, extrapolating the best linear fit (as determined by least squared residuals) to zero electrode spacing, and reading off the contact resistance, R_0 .

$$\sigma_m = \frac{\delta}{(R - R_0)wt} \quad (6)$$

Chapter 3

Production of Electrospun Fibers

In general, as shown in the processing flowchart in Figure 9, fluid properties and processing conditions affect one another in a network of different ways in electrospinning. All are factors that affect the resultant fiber structures. For example, the current carried by the jet is determined by the electric field imposed, the type of polymer and solvent and additives, as well as the rate of drying of the jet, which itself is affected by the type of polymer and solvent used. These two factors, the current on jet and the rate of drying, along with several other factors, ultimately determine the fiber radius we get through electrospinning.

Generally, the observations are that the radius of fibers increases with increasing concentration, increasing surface tension, increasing extensional viscosity, and decreases with increasing charge density. However, one cannot simply change one of them without affecting some other factors as well, because of the interdependence.

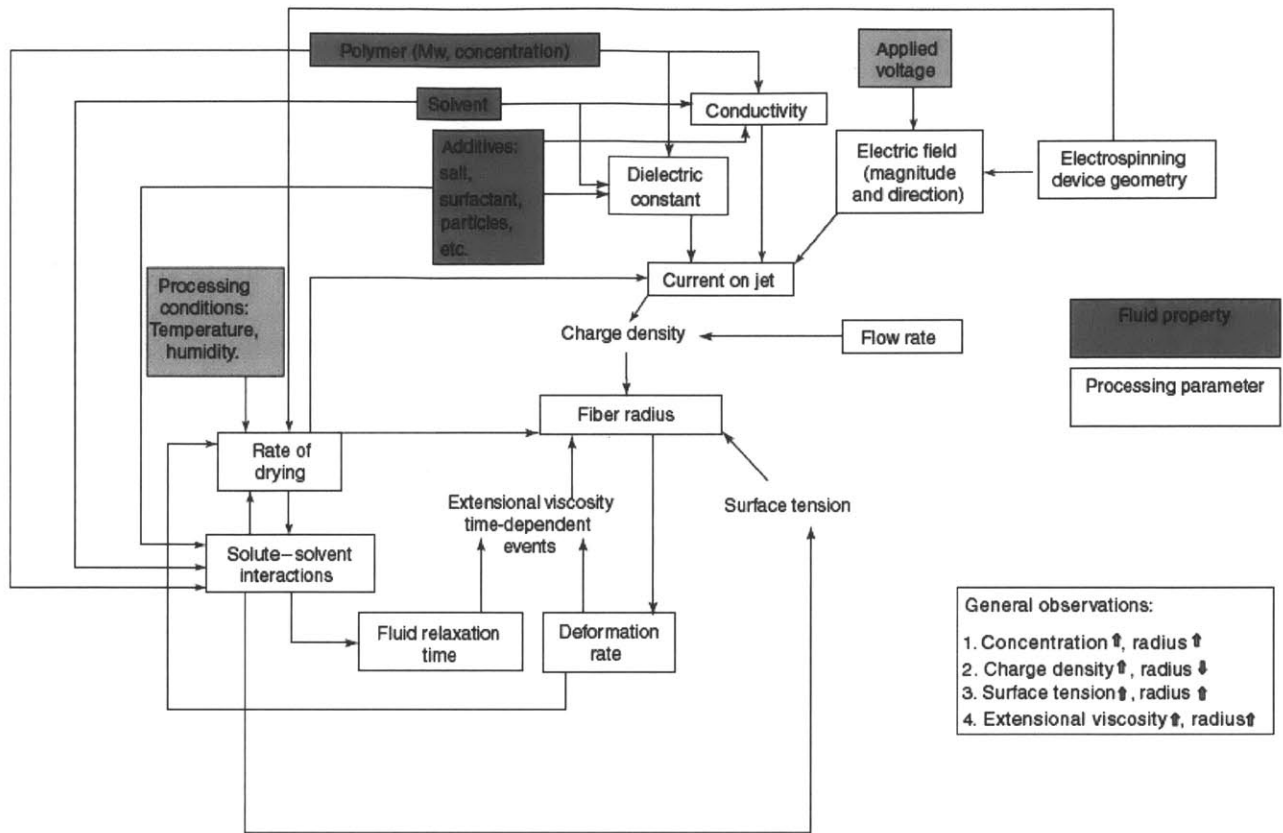


Figure 9 Flow chart illustrating how material properties, processing parameters, and processing conditions affect the resultant fibers ³³

3.1 Fibers from Polymer Blends

Polyaniline (PAni) is one of the most studied electrically conductive polymers, so it was chosen as the model system to study for electrospinning of conductive polymers. As is common among intrinsically conductive polymers, it has a fairly rigid backbone due to the high aromaticity, and is available only in relatively low molecular weight forms, so that the elasticity of its solutions is generally insufficient for it to be electrospun directly into fibers. To circumvent this problem, several different approaches have been reported. Strategies include electrospinning from solutions in concentrated sulfuric acid, a corrosive solvent,³⁴ coating polyaniline onto a non-conducting substrate,³⁵ and blending with more flexible, high molecular weight polymers that serve as processing aids.^{36 37} However, most of these reports demonstrate only the formation of nanofibers, but do not report their electrical properties. The highest conductivity reported for an electrospun PAni blend fiber is about more than two orders of magnitude lower than those reported for pure polyaniline films and fibers with diameters on the order of hundreds of micrometers.^{38 39} The difference is attributed in part to the necessity of blending of PAni with non-conducting polymers in order to form submicron diameter fibers, but also to the possible structural and molecular alignment differences in the fibers.

In our study of electrospinning fibers from polymer blends, PAni (emeraldine base, $M_w = 65,000$, Sigma-Aldrich, Inc.) was dissolved with an equimolar amount of dopant (+)-camphor-10-sulfonic acid (HCSA, Fluka Analytical Chemicals) in chloroform or in a mixture of chloroform and DMF with the weight ratio 5:1 to form solutions with concentrations ranging

from 0.5 to 2.0 wt% of doped PANi. The processing aid polymers, poly(ethylene oxide) (PEO, $M_w = 1,000,000$ and $2,000,000$ g/mol, Sigma-Aldrich, Inc.) or poly(methyl methacrylate) (PMMA, $M_w = 540,000$ and $960,000$ g/mol, Scientific Polymer Products Inc.), was then dissolved in these solutions in concentrations ranging from 2.0 to 4.0 wt% to form blended solutions for electrospinning. The parallel-plate electrospinning setup described by Shin et al.⁴⁰ was used to collect randomly-oriented fiber samples. The plate-to-plate distance was 30 cm.⁴¹ Aligned fiber samples were collected by replacing the lower collection plate with two parallel electrodes to orient the fibers across the gap, as described originally by Li et al.,⁴² with the electrodes 4.0 cm apart. The flow rate of the solutions was controlled by a syringe pump (Harvard Apparatus), and varied from 0.015 to 0.05 mL/min. The applied voltage across the plates was varied from 25 to 40 kV. The weight percentage of PANi in the resultant blended fibers ranged from 11% to 67% for the PANi-PEO blend system and 3.8% to 25% for the PANi-PMMA blend system, based on mass balance of the relative amounts of polymers dissolved in the solutions.

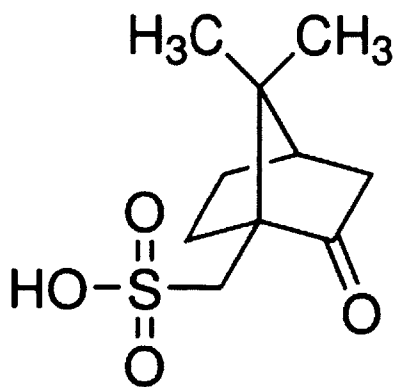


Figure 10 Molecular structure of HCSA, one of the most efficient dopants for PANi⁴³

PAni blended with PEO was readily electrospun into fibers from a mixed 5:1 chloroform/DMF solution, with compositions in the range of 11 to 67 wt% PAni in the final fibers. PAni blended with PMMA was electrospun from its chloroform solution to form fibers with 3.8 to 25 wt% PAni in the fibers. Attempts to electrospin blend solutions resulting in higher weight percentage of PAni in the fibers failed to produce continuous fibers, due to insufficient elasticity of the solutions. Detailed processing conditions and resulting fiber diameters are listed in Table 3. Some typical SEM images of the blended PAni-PEO fibers are shown in Figure 11.

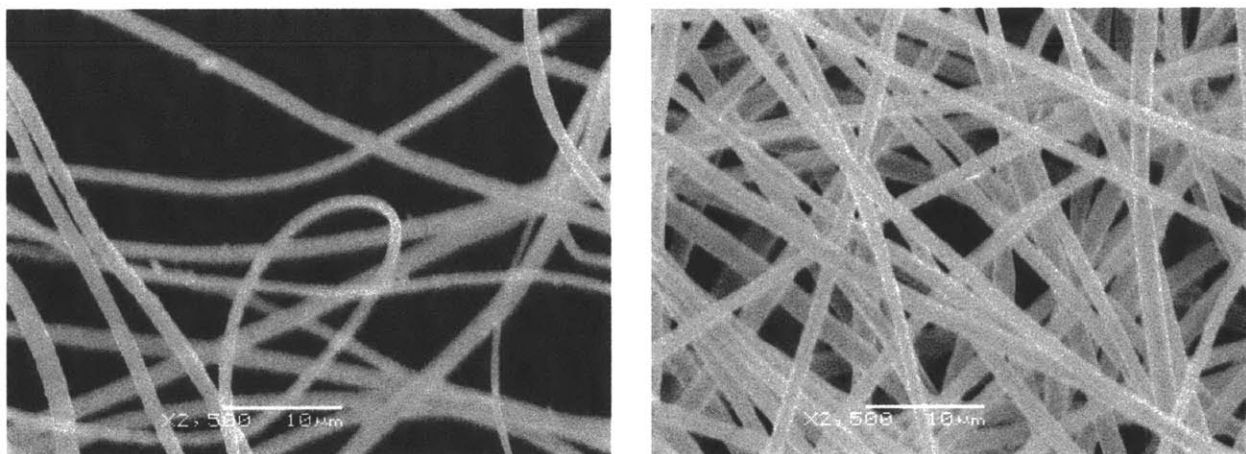


Figure 11 SEM images of PAni-PEO blend electrospun fibers with 11 wt% PAni in blend (left) and 20 wt% PAni in blend (right), PEO $M_w = 1,000,000$; taken under $2,500\times$ magnification (scale bar = $10\ \mu\text{m}$)

Table 3 Processing conditions and fiber diameters of PANi-blend fibers

Solvent (D: DMF; C: Chloroform)	Blended Polymer & MW	PAni wt% in solution	PAni wt% in resultant fiber	Flowrate (mL/min)	Applied Voltage (kV)	Fiber Diameter (μm)
C	PEO, 1M	0.5	11	0.015	35	1.2 ± 0.3
C	PEO, 1M	0.5	14	0.015	32	1.6 ± 0.4
5:1 C:D	PEO, 1M	1.0	20	0.02	40	1.5 ± 0.3
5:1 C:D	PEO, 2M	0.5	33	0.05	35	2.6 ± 0.8
5:1 C:D	PEO, 2M	1.0	50	0.05	40	2.7 ± 0.9
5:1 C:D	PEO, 2M	2.0	67	0.05	40	2.3 ± 0.7
C	PMMA, 0.54M	0.5	3.8	0.05	25	1.6 ± 0.3
C	PMMA, 0.54M	1.0	7.7	0.05	29	1.8 ± 0.3
C	PMMA, 0.54M	1.5	12	0.05	33	1.9 ± 0.4
C	PMMA, 0.96M	1.0	17	0.04	28	1.5 ± 0.2
C	PMMA, 0.96M	1.5	25	0.04	31	1.6 ± 0.3

Poly(3,4-ethylenedioxythiophene) (PEDOT) and poly(styrenesulfonate) (PSS), a different system of conducting polymers, was also blend with PEO with molecular weight of 1M in its water solution and electrospun into fibers. The molecular structure of the PEDOT-PSS forming

macromolecular salt is shown in Figure 12. The purchased water dispersion (Aldrich) has 1.3 to 2.6 wt% PEDOT:PSS in water. PEO was subsequently added to the water dispersion to achieve various concentrations in water solution. In some cases the solution was diluted by adding more water to lower the weight percent of PEO so as not to have a solution of too high viscosity. By mass balance, the highest amount of PEDOT:PSS achievable in the resulting solid electrospun fiber is 30 wt%. Table 4 lists the detailed processing conditions for this system of polymer blends.

Table 4 Processing conditions and fiber diameters of PEDOT-blend fibers

PEDOT:PSS wt% in solution	PEO wt% in solution	PEDOT: PSS wt% in fiber	Flowrate (mL/min)	Applied Voltage (kV)	Fiber Diameter (nm)
0	6.0	0	0.05	15	320 ± 80
0.7	5.9	10	0.05	15	300 ± 40
1.3	7.8	14	0.05	22	390 ± 60
1.3	6.0	18	0.05	14	240 ± 50
1.3	5.2	20	0.05	14	280 ± 50
2.6	7.0	27	0.05	17	480 ± 90
2.6	6.0	30	0.05	15	490 ± 50

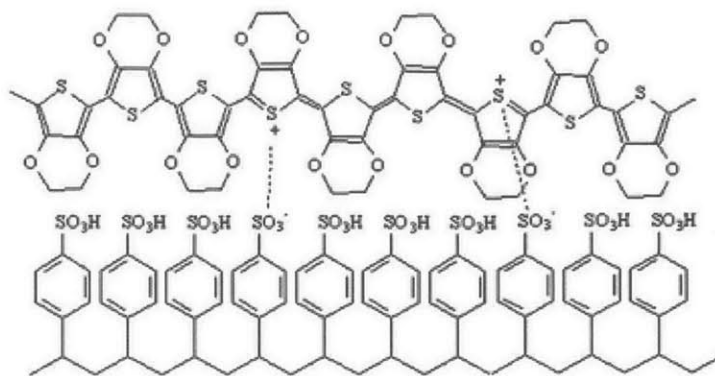


Figure 12 Structure of PEDOT-PSS Macromolecular Salt ⁴⁴

3.2 Fibers by Coaxial Electrospinning

While blending high molecular weight non-conducting polymers with the conductive polymers to make the solution electrospinnable remains one of the effective ways to solve the problem of low solution elasticity for conductive polymer solutions, the resulting fibers have much lower conductivity due to dilution of the conducting component. The co-axial (also known as “two-fluid”) electrospinning technique uses two spinnerets that are arranged concentrically so that a low-elasticity fluid introduced to the core of the jet can be elongated along with an electrospinnable fluid introduced to the shell of the jet. The result is a continuous filament with core-shell morphology.^{45 46} With the selective removal of the shell component of the resulting fibers, pure component electrospun fibers can be formed from fluids like the pure PANi solutions that are otherwise non-electrospinnable. Figure 13 shows the schematic of having two separate solutions controlled by different pumps forming coaxial jets during electrospinning.

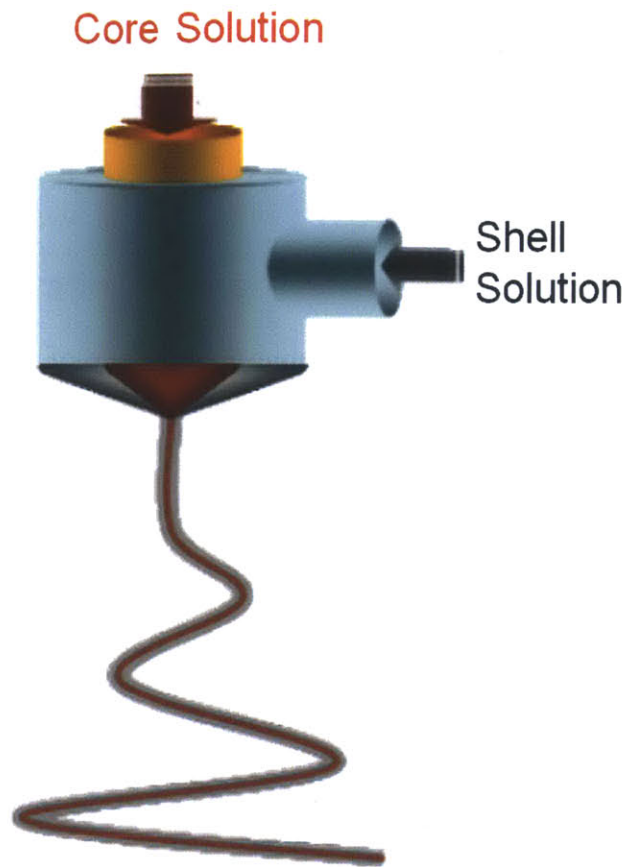


Figure 13 Schematic of coaxial electrospinning and resultant core-shell jets

For our co-axial electrospinning study, the electrospinnable conditions are such that the core fluid was 2 wt% PANi with an equimolar amount of HCSA in a 5:1 weight ratio of mixed chloroform and DMF; the shell fluid was 15 wt% PMMA in DMF. The co-axial spinneret had an inner spinneret diameter of 0.46 mm and outer spinneret diameter of 2.03 mm, both of which were charged to the same electrical potential. The core and shell fluid flow rates were 0.01 mL/min and 0.05 mL/min, controlled independently by two syringe pumps. The applied voltage was 34 kV and the distance between the spinneret and collection plate was 30 cm. After the

fibers were formed, the resultant fibers and mats were then immersed in isopropyl alcohol for one hour with gentle stirring, so that the PMMA shell component was removed, leaving intact the doped PANi fiber cores.

The core-shell PANi-PMMA fibers were fabricated by co-axial electrospinning to achieve smooth and continuous fibers. After removal of the PMMA shell component by isopropyl alcohol, the fiber diameters decreased from 1440 ± 200 to 620 ± 160 nm, but the fiber surfaces were still mostly smooth, as shown by representative SEM images in Figure 14.

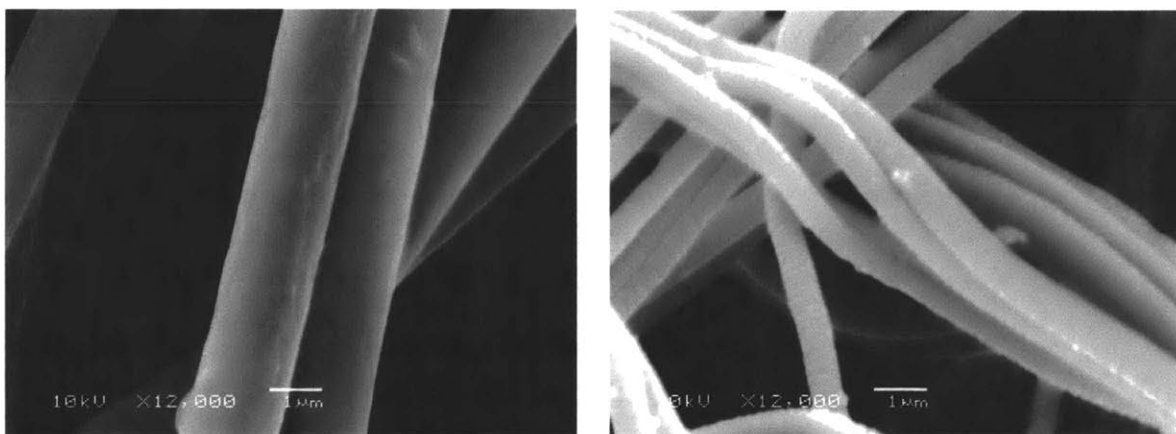


Figure 14 SEM images of electrospun PANi-PMMA core-shell fibers before (left) and after (right) dissolution of PMMA by isopropyl alcohol; taken under 12,000× magnification (scale bar = 1 μm)

X-ray photoelectron spectroscopy (XPS) was used to determine the extent to which the shell component was removed by dissolution in isopropyl alcohol. XPS generally probes only

the first (approximately) 10 nm of the surface of the samples, so it provides an accurate measure of the surface composition. The elemental compositions obtained from XPS results were then converted into percentages of the possible fiber components (PAni, HCSA, PMMA) using the best fit to a system of equations from elemental balances of each element present (C, O, N, S).

As shown in Table 5, the results suggest that before dissolution the surface of the fibers is almost entirely PMMA, while after dissolution most of the PMMA is gone, leaving behind PAni and the dopant HCSA. As the ratio of PAni to HCSA should ideally be 1 to 1 in the fibers, the XPS results suggest that some of the dopant is lost during the dissolution process, and possibly in the electrospinning process itself, too. This contributes negatively to the conductivities measured, as fibers with compositions less than the equimolar amount of dopant to PAni are known to exhibit lower electrical conductivities than those with equimolar amounts of dopant.⁴⁷

Table 5 XPS Results showing Surface Compositions of Core-Shell Electrospun Fibers before and after Dissolution of Shell

	Before Dissolving Shell	After Dissolving Shell
C atomic %	73 ± 2	81 ± 3
O atomic %	26 ± 2	8.7 ± 2.0
N atomic %	0.87 ± 0.10	8.2 ± 0.5
S atomic %	0.03 ± 0.005	2.0 ± 0.2
PAni %	6.5 ± 0.6	67 ± 4
HCSA %	0.6 ± 0.4	30 ± 4
PMMA %	93 ± 3	4.5 ± 2.0

Differential scanning calorimetry (DSC) was also used to characterize the composition of the core-shell fibers measured between -40 and 160 °C. The results show no discernable PMMA glass transition signals ($T_g = 124^\circ\text{C}$) in the core-shell PANi fibers after removal of the shell, further supporting the claim that almost all of the PMMA in the shell has been removed. Both PANi and HCSA signals are observed in the fibers separately, suggesting that there is some phase separation between PANi and the dopant HCSA. This also affects the measured conductivities negatively, as phase separation of the two components decreases the electrical conductivity of the system.⁴⁸ Also, PANi in this form shows no crystallinity transition between -40 and 160 °C.

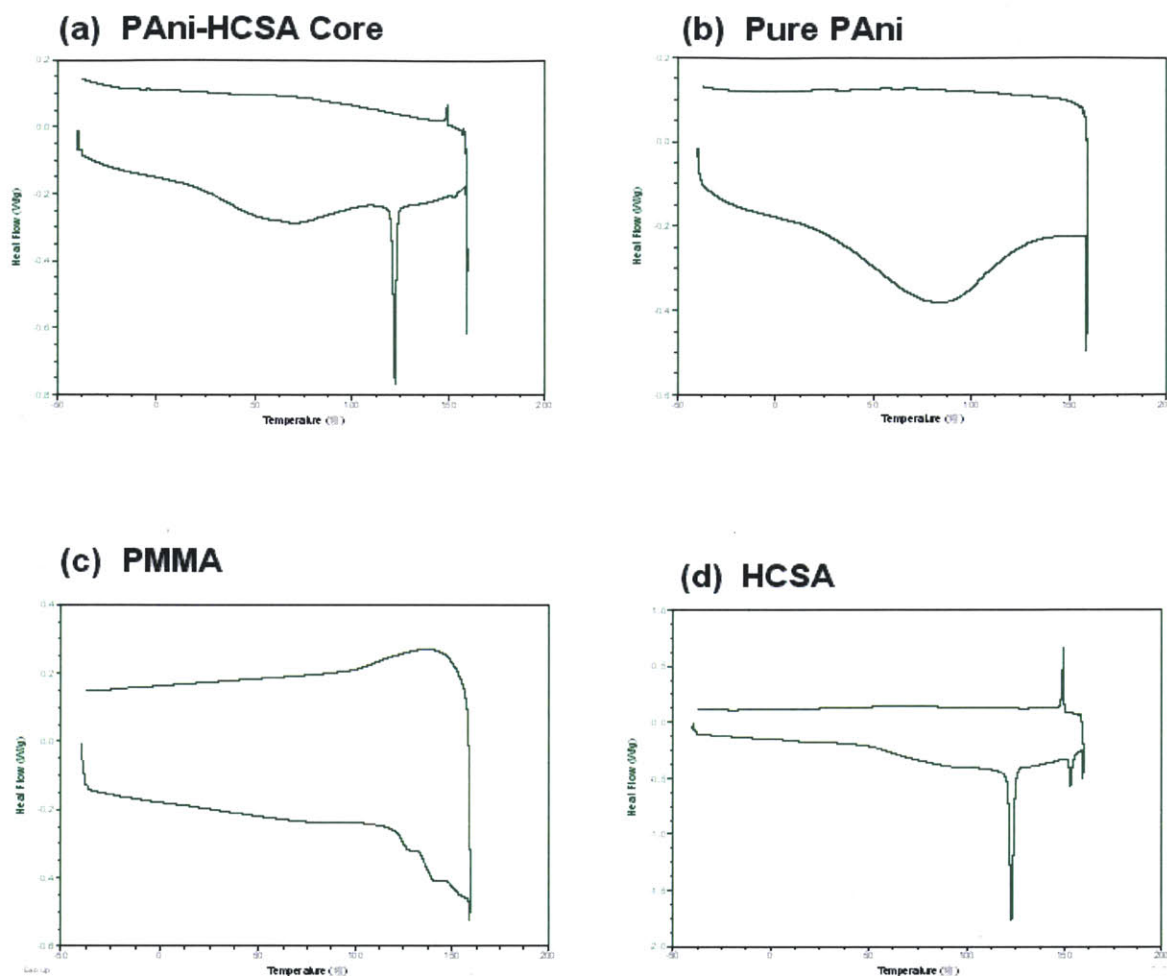


Figure 15 DSC Results of (a) core-shell PANi fibers after removing shell; (b) pure PANi; (c) pure PMMA; (d) pure dopant HCSA; all measured between -40 and 160 °C and the horizontal axes are all from -50 and 200 °C

In addition, the amount of HCSA dopant was varied in coaxial electrospinning with molar ratios of HCSA to PANi of 0, 0.25, 0.50, 0.75 or 1, to yield fibers with the whole range of electrical conductivities. Figure 16 shows representative images of the PANi/HCSA fibers after coaxial electrospinning and removal of the PMMA shell component by dissolution in IPA. The

fibers are confirmed to be smooth, relatively uniform in diameter and continuous. No significant difference in fiber diameters is observed for fibers prepared with molar ratios of HCSA to PANi of 0, 0.25, 0.50, 0.75 or 1.

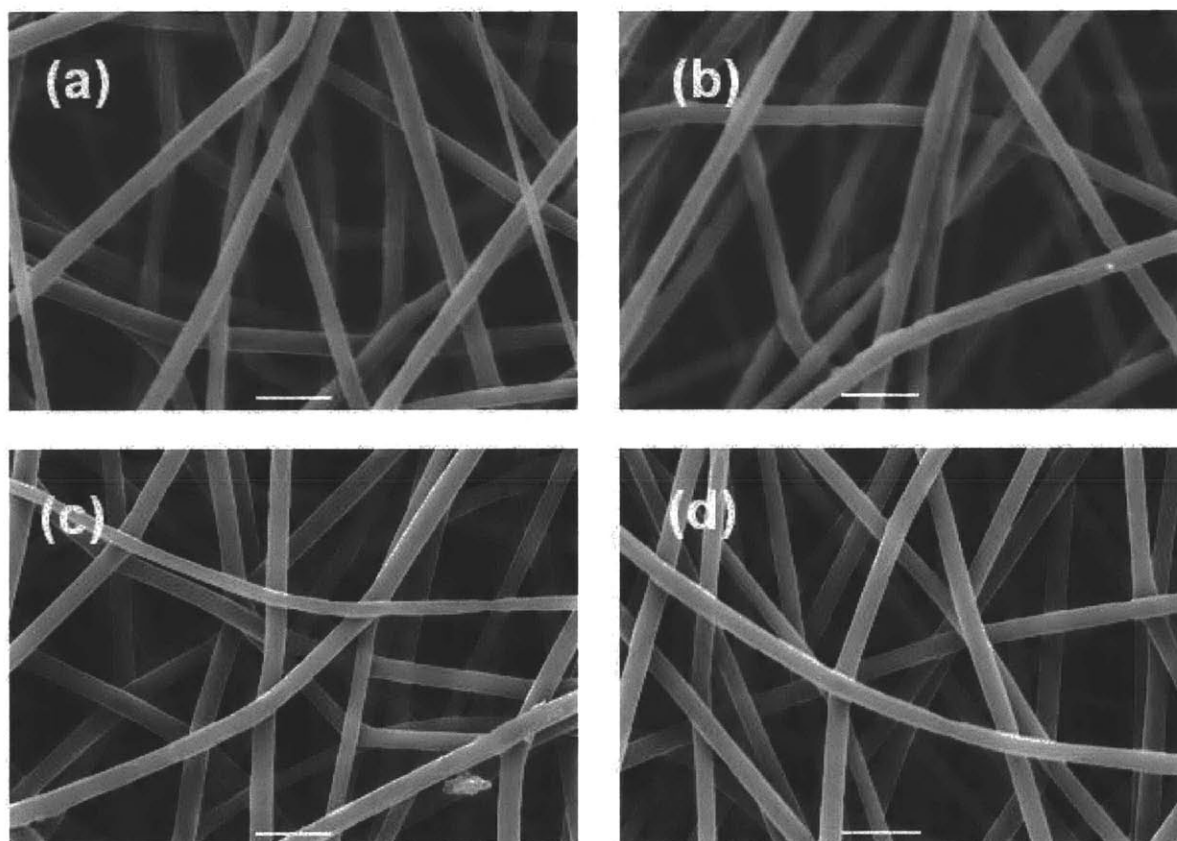


Figure 16 SEM images of electrospun PANi/HCSA fibers with different molar ratios of HCSA to PANi: [HCSA]/[PANi] = 0 (a); 0.5 (b); 0.75 (c); and 1.0 (d). All images taken after dissolution of PMMA shell and using 7,500 \times magnification (scale bar = 2 μ m)

3.3 Fibers with Surface Coating

Various surface treatment methods, such as in-situ polymerization, chemical vapor deposition, and layer-by-layer deposition, can be used to have conductive coatings on non-conductive polymeric fiber substrate. With careful control of the experimental conditions, surface layers can be coated and then tested for electrical performances and compared to fibers that were directly electrospun. In these cases, the chemical nature of the non-conducting substrate may not be important, so the major variables are the thickness of the coating layer and the diameter of the electrospun fiber (or the ratio of the two). The overall porosity of the electrospun fiber mat may also affect the morphology and thus electrical conductivity.

One of the simplest ways to surface-coat an electrospun fiber mat is to immerse it in a solution of monomers and perform in-situ polymerization to have the conductive polymer forming on the fiber surfaces. For example, an electrospun polycaprolactone (PCL) mat was immersed in pyrrole solutions up to 0.10M in concentration, and 0.10M of iron(III) chloride as catalyst to polymerize at room temperature, with constant stirring for 3 hours, and the coating results are shown in Figure 17. The problem with this approach is that the coating is very non-uniform, as can be seen for the polypyrrole coating onPCL.

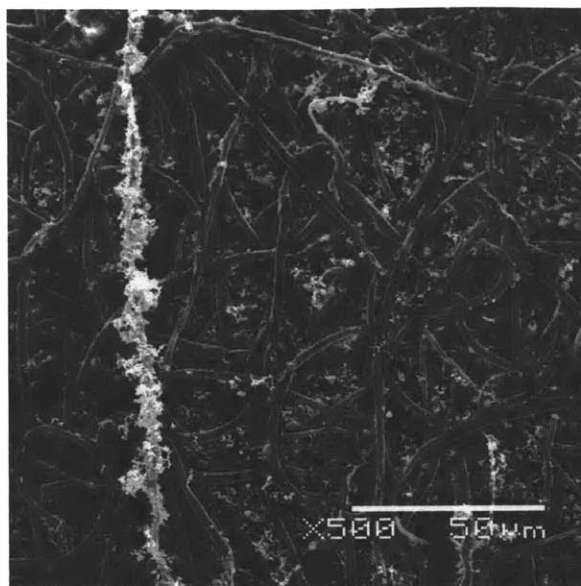


Figure 17 SEM image of electrospun polycaprolactone (PCL) fibers after in-situ solution polymerization with pyrrole and iron(III) chloride to form polypyrrole coatings

In principle, effective coating must be uniform and conformal, in order to utilize the large specific surface area of the substrate and allow for continuous pathways for electrons to conduct through the samples. Conformality is also important so that the electrospun fibers with these coatings can be reproducible and compared across different samples as well as different processing methods.

Oxidative chemical vapor deposition (oCVD) can be used to coat electrospun nanofibers with conductive polymers.^{49 50} PEDOT, one of the most widely used conductive polymer, has been deposited on both PA 6(3)T and PEO fibers using oCVD, with iron(III) chloride as oxidant and at an operating temperature of 80°C. Figure 18 shows the microscopic images of the fibers

before and after coating. It is apparent that the coatings are not uniformly thick on the fibers, though they do seem to cover all the fibers and most of the fiber surface areas.

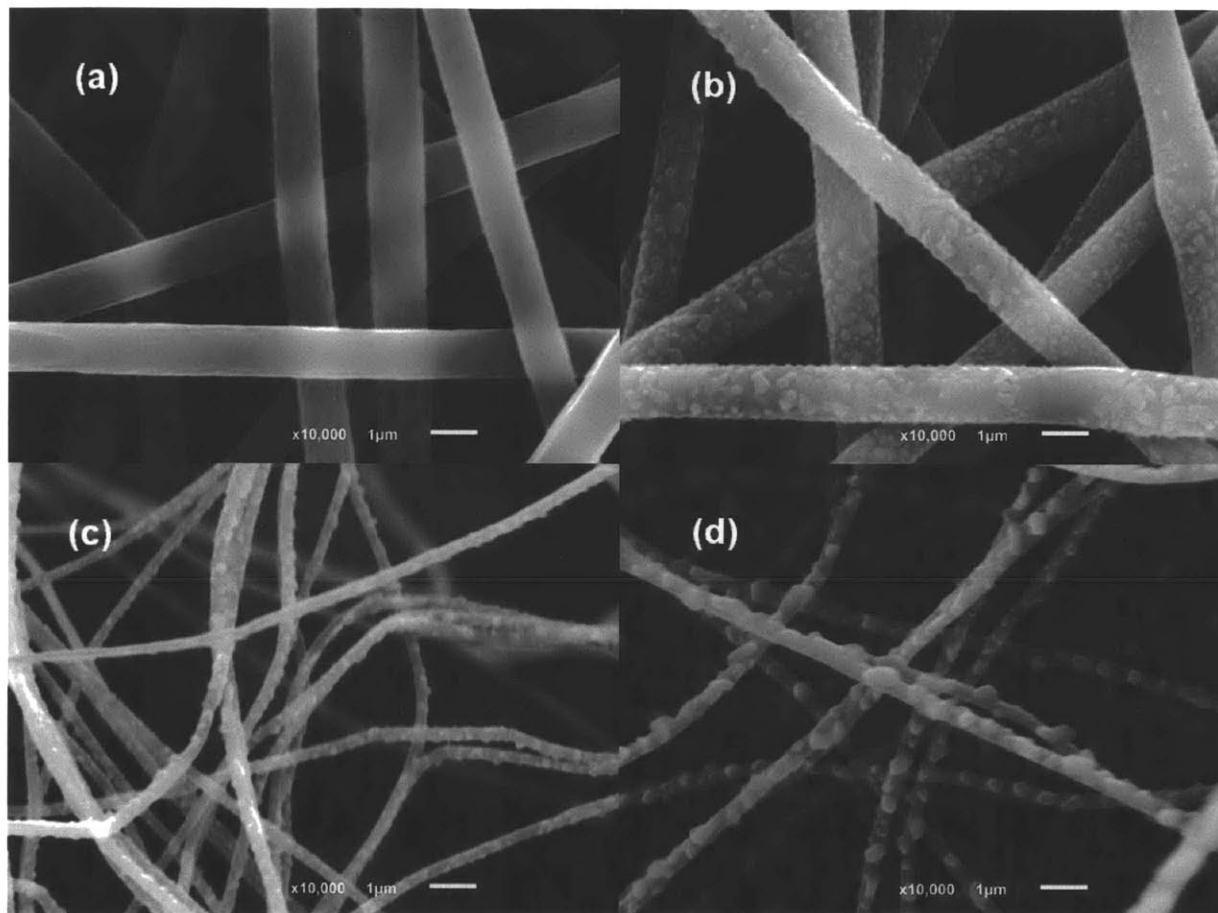


Figure 18 SEM images (scale bar 1 μm , 10,000 \times magnification) of (a) as-electrospun PA 6(3)T fibers; (b) PA 6(3)T fibers CVD coated for 10min; (c) PEO fibers CVD coated for 5min; (d) PEO fibers CVD coated for 10min; all coatings were done at 80 $^{\circ}\text{C}$ with PEDOT

Layer-by-layer deposition is another way to coat electrospun fibers. Coating can be achieved by dipping the fiber mat in oppositely charged solutions in sequence. The challenge

with this approach is also with the issue of conformality. There is the possibility of the coating layer bridging between fibers and covering up the pores in the fiber mat, as shown in Figure 19.

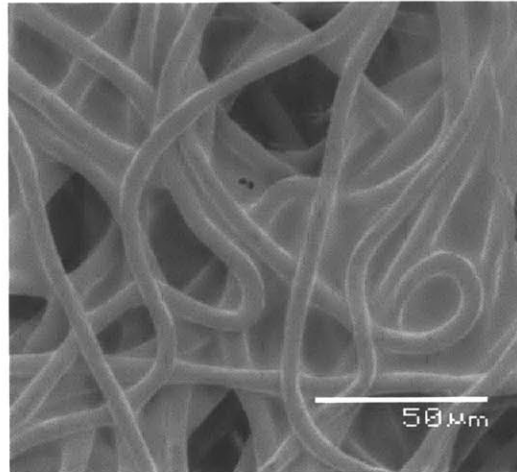


Figure 19 SEM Image of Electrospun Polycaprolactone Fibers after Coating by Layer-by-layer Deposition

Overall, there are many challenges for obtaining uniformly and conformally coated electrospun fibers. Electrospinning with the coaxial electrospinning technique and from blended solutions, by comparison, have more control over the fiber morphologies.

Chapter 4 Mats

Electrical Conductivities of Fibers and

4.1 Conduction in Conductive Polymer Fibers

In general, the conductivity of any material is given by

$$\sigma = ne\mu \quad (7)$$

where n is the number of charge carriers, e is the charge on the charge carriers, and μ is the charge carrier mobility.

It is established that for most of the intrinsically conductive polymers, their conduction bands are partially filled because of the conjugated π orbitals, and have a width of about an order of magnitude larger than kT .⁵¹ These bands are one dimensional as they are restricted to the backbone of the long-chain polymers. Thermally activated hopping of electrons, however, occurs in both intra-molecular and inter-molecular fashion. There is evidence that when disorder on the molecular level, such as random chain conformations and chemical defects, is prevalent, the conductivities are much lower.⁵² This suggests that intra-molecular electron transport is important and can be enhanced greatly with chain alignment and the removal of defects. Inter-molecular charge transport, on the other hand, is believed to be the reason of these doped conductive polymers still having electrical conductivities several orders of magnitude short of metallic.⁵³

In a mixture of conductive and non-conductive components, such as those obtained from a blended polymers solution of conductive and non-conductive processing aid polymers, it is expected that the electrical conductivity of the whole mixture shows a percolation behavior, such as shown in an illustration in Figure 20.⁵⁴ That means when the non-conductive polymer having a conductivity σ_p is dispersed with a conductive polymer and when the fraction φ reaches a critical value φ_c , called the percolation threshold, an infinite conductive cluster is formed and, consequently, the composite becomes much more conductive. As the filler concentration increases from φ_c , the value of σ increases rapidly over several orders of magnitude, from the value σ_c at the percolation threshold to the maximal value σ_m , and according to the percolation theory, is expected to follow a relationship such that

$$\sigma \sim (\varphi - \varphi_c)^t \quad (8)$$

where the exponent t is usually between 1.5 and 2. Below the percolation threshold, the conductivity change is expected to be negligible and the conductivity of the composite is equal to the non-conductive polymer conductivity σ_p or slightly higher.

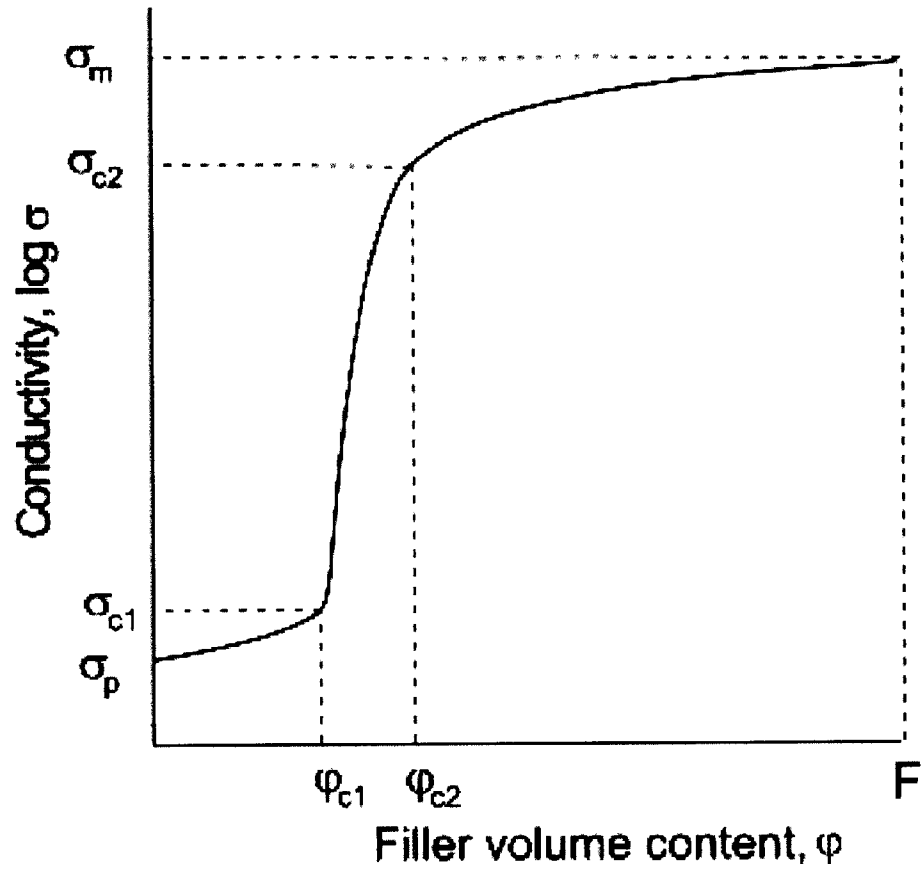


Figure 20 Typical dependence of electrical conductivity (logarithm) on conductive filler volume content ⁵⁴

4.2 Experimental Fiber Electrical Conductivities

The fiber electrical conductivities of the as-electrospun polyaniline and polyaniline-blend fibers with equimolar of HCSA doping are summarized in Figure 21. These are the results of electrical conductivities measured by IDE across the whole range of polyaniline compositions in the electrospun fibers, up to 100% for the fibers formed by co-axial electrospinning and subsequent dissolution of the shell.

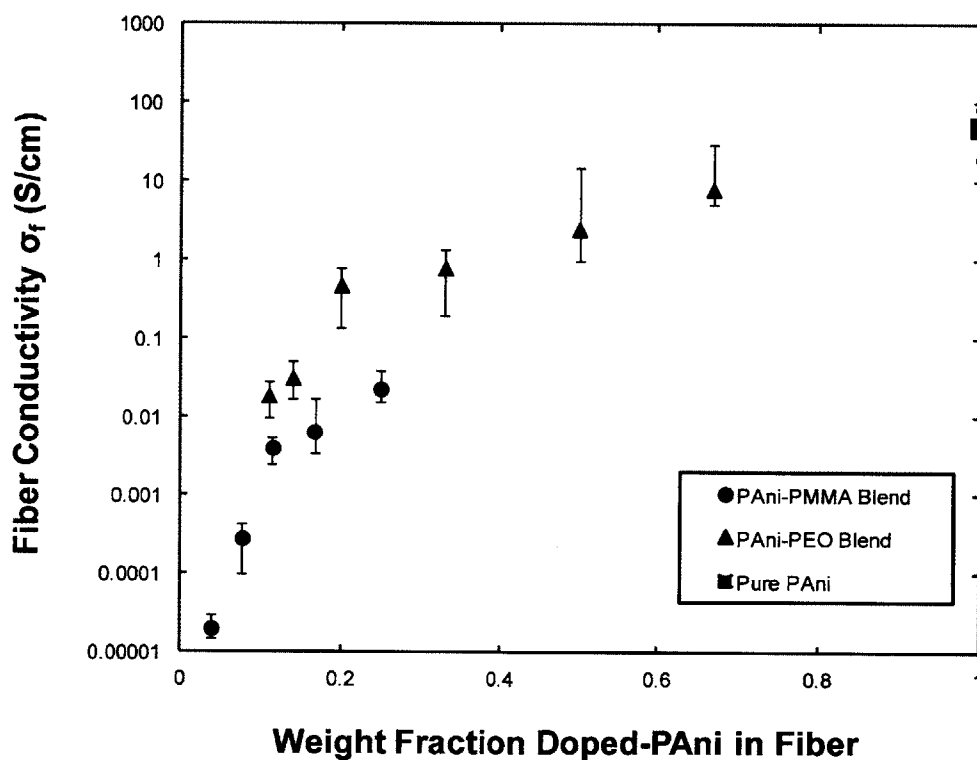


Figure 21 Electrical conductivity of as-electrospun polyaniline fibers (nominally doped with an equimolar amount of HCSA) as a function of the weight fraction of PAni in the blended fibers; the pure PAni fiber was obtained after dissolving the shell component (PMMA) of the core-shell fibers

The electrical conductivity of electrospun polyaniline-blend fibers increases exponentially with the weight percent of doped polyaniline in the fibers. The electrical conductivities of the PANi-PEO blend fibers are an order of magnitude higher than those of the PANi-PMMA blend fibers for the same weight percent of PANi, indicating that the blend polymers are not simply acting as non-conducting fillers in the fibers. The difference in conductivities of the PEO and PMMA blends is attributed to the different intrinsic conductivities of PEO ($\sim 10^{-6}$ S/cm) and PMMA ($\sim 10^{-10}$ S/cm) and the difference in their degree of compatibility with PANi.¹²

The highest electrical conductivity achieved is for the 100% PANi fibers after the shell PMMA component was removed; the calculated fiber conductivity is found to be 50 ± 30 S/cm. To the best of our knowledge, this value is the highest electrical conductivities measured for electrospun polyaniline nanofibers, comparable to that reported by Yu et al.⁵⁵ for electrospun fiber bundles.

For fibers with the amount of HCSA dopant varied with molar ratios of HCSA to PANi of 0, 0.25, 0.50, 0.75 or 1, the electrical conductivities of the fibers increase exponentially with increasing molar ratio of HCSA to PANi, as shown in Table 6. This trend is consistent with the observations of Trchova et al for PANi fibers with different doping levels.⁵⁶

Table 6 Diameter and Conductivity of As-spun PAni/HCSA Fibers after Removing Shell

[HCSA]/[PAni] Mole Ratio	Diameter, d (nm)	Electrical Conductivity, σ_f (S/cm)
0	650 ± 110	$(2.0 \pm 0.6) \times 10^{-6}$
0.25	670 ± 120	0.0022 ± 0.0008
0.50	600 ± 90	0.18 ± 0.05
0.75	650 ± 110	2.3 ± 0.9
1.0	620 ± 160	50 ± 30

To increase the molecular orientation within the fibers, the core-shell fibers were post-processed by stretching along the fiber axes. This was achieved by first electrospinning fibers in an oriented fashion between two parallel electrodes connected by an element under compression so that the gap was 1.0 cm, and then partially releasing the compression to realize strains of 0.3 to 1.0. There was no apparent separation of core and shell layers due to the deformation. The shell component of the stretched fibers was then dissolved by isopropyl alcohol, similar to the as-electrospun fibers, and the fiber conductivities measured. The results are shown in Table 7.

Table 7 Electrical Conductivities of PANi Fibers after Stretching

Strain	Fiber Diameter (nm) after removing shell	Electrical Conductivity (S/cm) after removing shell
0	620 ± 160	50 ± 30
0.30	570 ± 200	54 ± 15
0.50	500 ± 150	70 ± 50
0.72	450 ± 70	105 ± 40
1.0	420 ± 130	130 ± 40

As expected, the fiber diameters decrease with increasing strain. The electrical conductivities, on the other hand, increase noticeably with increasing strain. The highest electrical conductivity achieved this way was 130 ± 40 S/cm, a three-fold improvement over the as-spun fiber conductivity. Note that all fiber conductivities reported here have been corrected for contact resistance.

4.3 Electrical Conductivity and Molecular Orientation within Fibers

Polarized Fourier-transformed infrared spectroscopy was used to measure the molecular orientation of the polyaniline molecules within the electrospun fibers. Bundles of aligned fibers, on the order of 20 to 50 fibers for each sample, were required for this measurement. The dichroic ratio $D = A_{\parallel} / A_{\perp}$ where A_{\parallel} and A_{\perp} are the absorbance related to the C-N stretching mode (1490 cm^{-1} and 1510 cm^{-1}) measured with the incident beam polarized parallel and perpendicular to the fiber bundle axis, respectively. The overall molecular orientation, f , and the angle between the molecular axis and the fiber bundle axis, Ω , as shown in Figure 22(a), can be calculated from Eq. 5,⁵⁷

$$f = \frac{3\langle \cos^2 \Omega \rangle - 1}{2} = \frac{(D-1)(2 \cot^2 \alpha + 2)}{(D+2)(2 \cot^2 \alpha - 1)}, \quad (9)$$

where α is the angle between the molecular axis and the C-N bonds (shown in Figure 22(a)). α is between 30° and 39° in polyaniline. Here, $f = 1$ represents perfect alignment of molecules along the fiber axis, $f = 0$ represents random orientation, and $f = -1/2$ represents molecular alignment perpendicular to the fiber axis.

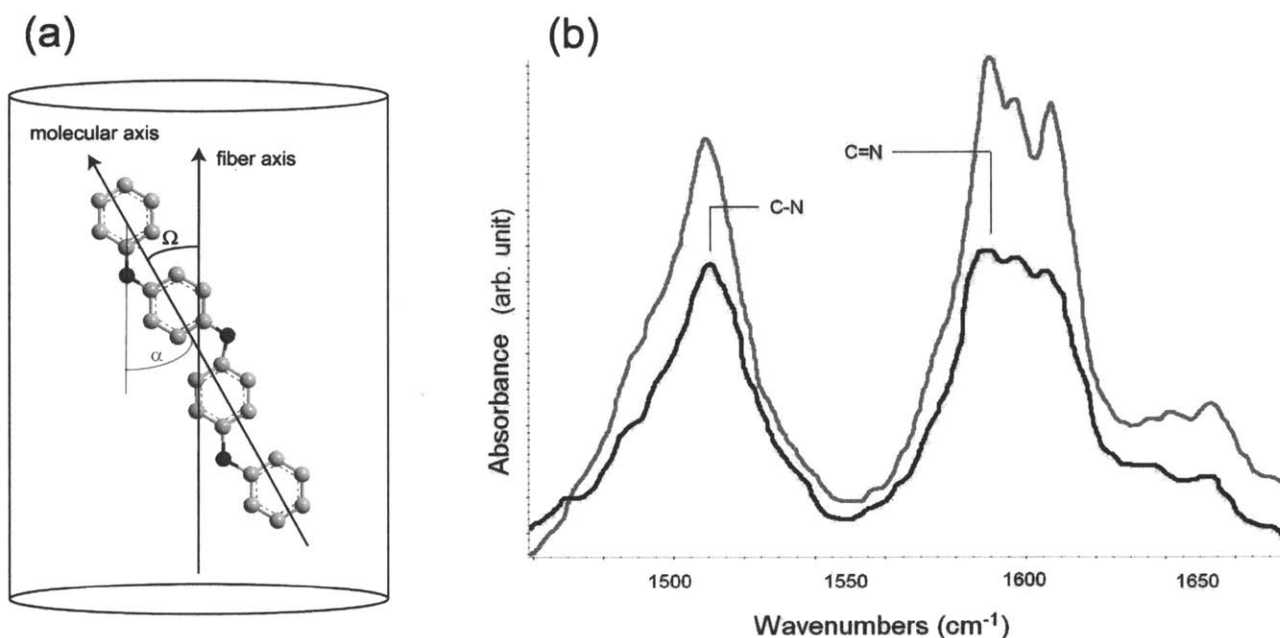


Figure 22 (a) Illustration of molecular orientation of polyaniline in fibers; (b) polarized-FTIR result for PANi fibers stretched to a strain of 0.72, with parallel spectrum in grey and perpendicular spectrum in black

To explain the improvement of conductivity with deformation, the results of the polarized FTIR measurements on the stretched fibers are shown in Figure 23. It shows a clear positive correlation between the electrical conductivities and the molecular alignment within the fibers. The as-spun fibers exhibit a modest level of molecular orientation ($f = 0.1 - 0.15$ for $d = 620$ nm). This is comparable to the orientation observed by Pai et al in as-electrospun fibers of PA 6(3)T (poly(trimethyl hexamethylene terephthalamide)) of comparable diameter,⁵⁸ and can be attributed to the elongational nature of the fiber forming process. Subsequent solid-state drawing increases the molecular orientation to levels ($f = 0.35 - 0.4$) previously observed only for as-

electrospun PA 6(3)T fibers with diameters on the order of 100 nm. It can thus be concluded that post-spin solid state drawing is more efficient than elongational flows during fiber formation to increase molecular orientation, and that the enhanced molecular orientation is the origin of the higher conductivities observed.

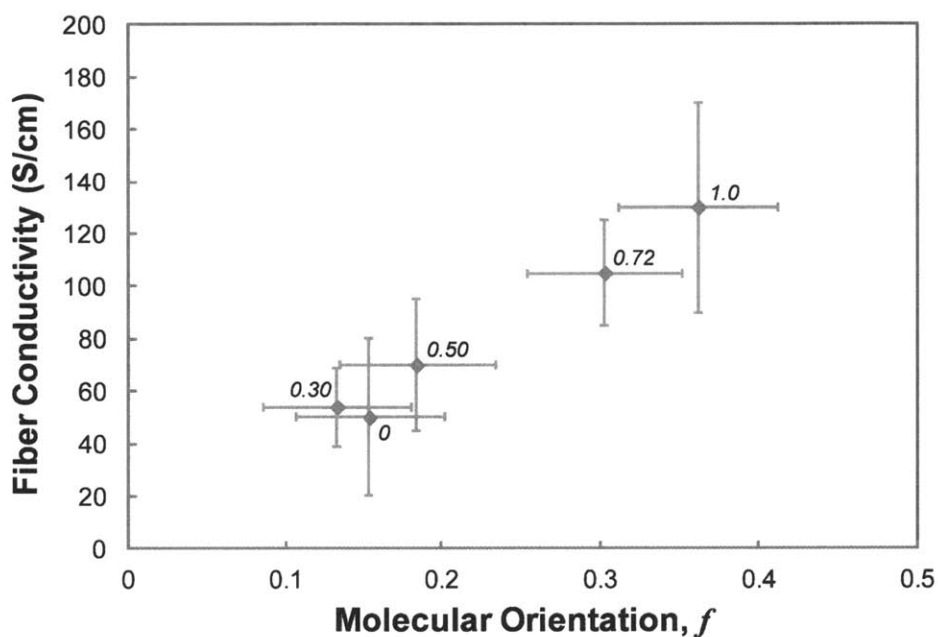


Figure 23 Electrical conductivity of the pure polyaniline fiber, as-spun and after solid-state drawing, as a function of molecular orientation within the fibers, as measured by polarized FTIR from aligned fiber bundles; the label next to each data point shows the corresponding nominal strain.

4.4 Mat Conductivity – Fiber Conductivity Correlations

4.4.1 Experimental Mat Electrical Conductivity

The measured mat conductivities, defined by Eq. 3, are shown in Figure 24. The trend in conductivity of the mats with composition is very similar to that observed for the fibers themselves, shown in Figure 21, but the values are lower by an order of magnitude or more. This difference between the fiber conductivities and mat conductivities can be caused by several factors. These may include differences in fiber composition, fiber microstructure, fiber curl, mat porosity, fiber orientation distribution within mats, fiber-fiber contacts in mats, etc. In order to reconcile these differences, we consider the effect of several of these factors in turn.

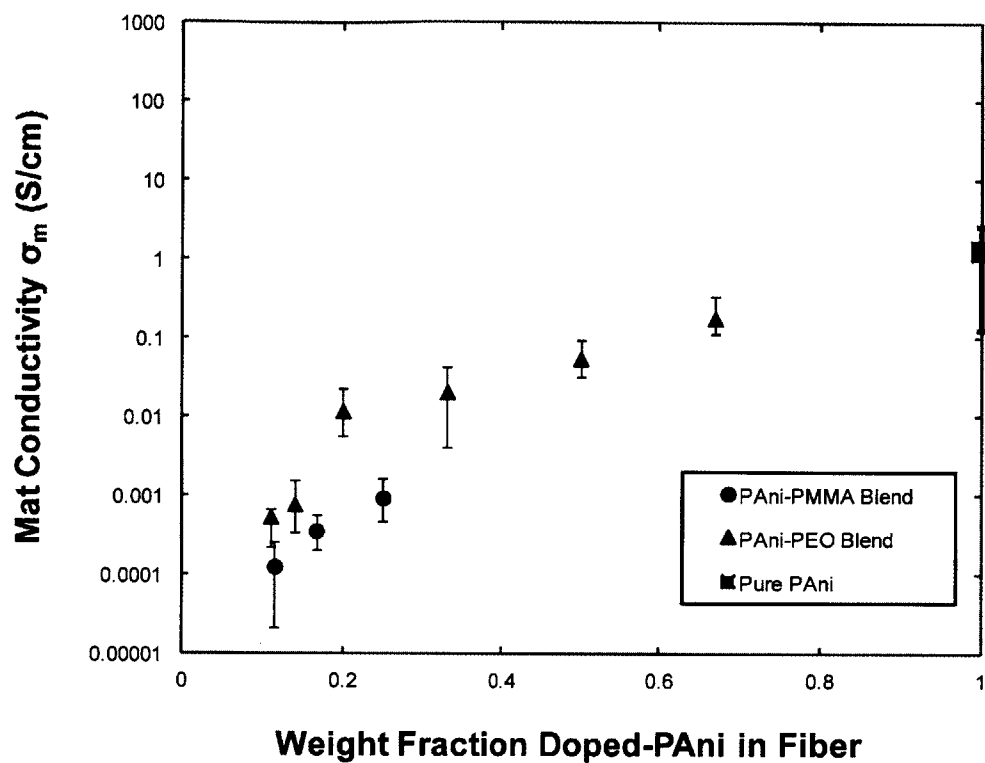


Figure 24 Mat electrical conductivity of polyaniline fiber mats (as-electrospun, nominally doped with an equimolar amount of HCSA) as a function of the PAni weight fraction in the blended fibers; the pure PAni fiber mat was obtained after dissolving the shell component (PMMA) of the core-shell fibers

4.4.2 Mat Porosity

To account for mat porosity, we adopt a simple, volume-averaged model for mat conductivity based on the rule of mixtures, expressed by Eq. 10, where σ_m^{calc} is the calculated mat conductivity, σ_f is the measured fiber conductivity, and ϕ is the measured mat porosity. The matrix (void) component has effectively zero conductivity, $\sigma_{void}=0$. Variations in composition are taken in to account through the use of the measured fiber conductivity of the same composition; molecular orientation within the fibers is assumed to be comparable for both aligned fibers on IDE's and randomly orientated mats.

$$\sigma_m^{calc} = (1 - \phi)\sigma_f + \phi\sigma_{void} = (1 - \phi)\sigma_f \quad (10)$$

4.4.3 Fiber Orientation in Fiber Mats

We account for the effect of fiber orientation on the measured resistances of the mats next. Unlike the measurement of fiber conductivity on the IDEs, where the fibers were collected in an aligned fashion and Eq. 2 can be applied, the measured mat conductivity depends on both the length of the copper foil electrodes and the distance of separation between them. Since

nonwoven fiber mats generally do not have a unidirectional aligned fiber orientation distribution, some fraction of the fibers does not provide a conducting path from one electrode to the other; furthermore, those that do provide a conducting path are generally inclined at some angle to the normal direction between electrodes, and so experience a longer path length. To account for this, we assume that all of the fibers act as resistors in parallel. Let the length of individual fiber that connects both electrodes be l . The resistance to electrical current from one electrode to the other via this fiber is expressed by Eq. 11,

$$R_f = \frac{4l}{\pi d^2 \sigma_f} \quad . \quad (11)$$

The inverse of total resistance is obtained as the sum of the inverse resistances of all fibers that provide a conducting path from one electrode to the other:

$$\frac{1}{R} = \sum_{i=1}^N \frac{1}{R_{f,i}} = \left[\frac{\pi}{4} \sum_{i=1}^N \frac{d_i^2 \sigma_{f,i}}{l_i} \right] \quad . \quad (12)$$

Plugging Eq. 12 into Eq. 4, we obtain:

$$\sigma_f^{odf} = \delta \langle \sigma_f / l \rangle, \quad (13)$$

where the superscript ‘odf’ has been introduced to clarify that the effective fiber conductivity in the two-electrode experiment depends on the orientation distribution function (odf) of the fibers within the mat.

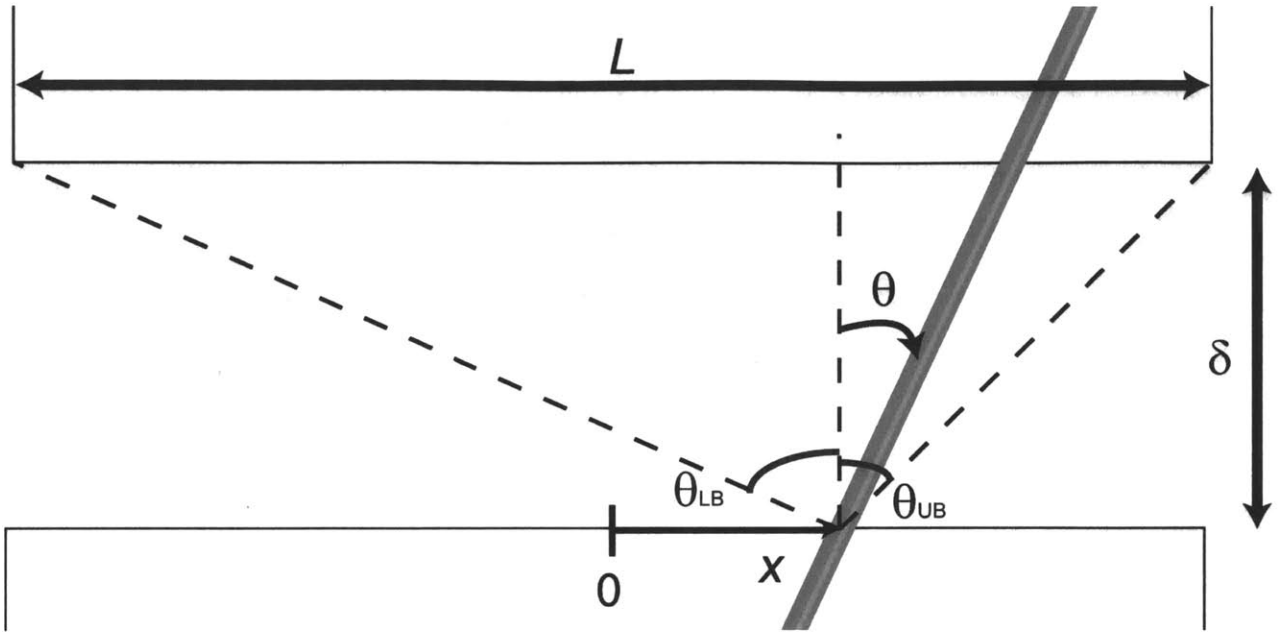


Figure 25 Definition of fiber orientation angle θ between across two electrodes with width L , separated by a gap δ . X denotes the position where the fiber makes contact with one of the electrodes. $\theta_{LB}(x)$ and $\theta_{UB}(x)$ denote the upper and lower bounds in orientation angle, beyond which a fiber located at position x does not make contact with the second electrode

To evaluate the fiber ensemble average $\langle \sigma_f/l \rangle$, we sum over all the fibers that contact the first electrode at a point x with an orientation angle θ , as illustrated in Figure 25. The corresponding orientation distribution function is $p(x, \theta)$. We assume that the fiber orientation distribution is uniform throughout the mat and independent of the position x , i.e. $p(x, \theta) =$

$(1/L)p(\theta)$, where L is the length of the copper foil electrodes, and that the fibers are straight, with length $l = \delta/\cos\theta$. The range of orientation angle within which a fiber leaving the first electrode makes contact with the second electrode is a function of position, x . The upper and lower bounds of the range are $\theta_{UB}(x) = \arctan\left(\frac{L-2x}{2\delta}\right)$ and $\theta_{LB}(x) = \arctan\left(\frac{-L-2x}{2\delta}\right)$, respectively.

We assume that these fibers all have the same fiber conductivity, as measured by the IDE experiments. Fibers that fall outside of these bounds do not make contact with the second electrode and have effectively infinite resistance ($\sigma_{f,i} = 0$) for purposes of the mat measurement. This leads to the following expression:

$$\begin{aligned}\sigma_f^{odf} &= \delta \int_{-L/2}^{L/2} dx \int_{-\pi/2}^{\pi/2} \frac{\sigma_f(x, \theta)}{l(x, \theta)} p(x, \theta) d\theta \\ &= \frac{\sigma_f}{L} \int_{-L/2}^{L/2} dx \int_{\theta_{LB}(x)}^{\theta_{UB}(x)} p(\theta) \cos\theta d\theta\end{aligned}\tag{14}$$

Replacing the fiber conductivity with its odf-corrected value in Eq. 10, we obtain the following relation, which accounts for composition, porosity and fiber orientation distribution within the mat:

$$\sigma_m^{calc} = (1-\phi)\sigma_f^{odf} = (1-\phi)\sigma_f\left(\delta\langle 1/l \rangle\right).\tag{15}$$

4.4.4 Fiber Orientation Distribution Calculation

To determine the mat conductivity calculated according to this model, we first measured the orientation distribution of fibers in the mats, $p(\theta)$, by SEM image analysis.⁵⁹ We then evaluated the double integral of Eq. 14 numerically using the `quad2d` function in MATLAB to obtain the value of the orientation correction factor, $(\delta\langle 1/l \rangle)$. Figure 26 shows the variation of the orientation correction factor as a function of the ratio of the electrode length to separation, L/δ , for the special case of a random in-plane fiber orientation distribution function, $p(\theta)=1/\pi$.

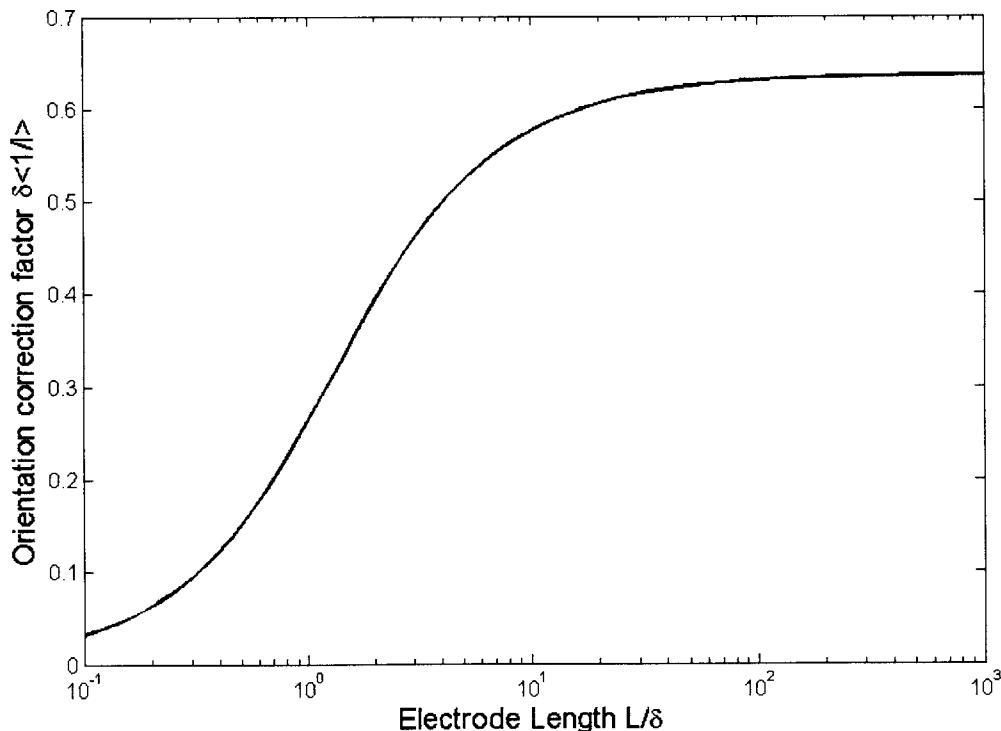


Figure 26 Orientation correction factor for mat conductivity as a function of the measurement geometry (ratio of electrode length to electrode separation), assuming a uniform angular distribution of fibers in the plane of the mat

To check the validity of this orientation correction factor, we fabricated mats with different fiber orientation distributions for each of three different fiber compositions, 20% PAni-PEO, 67% PAni-PEO, and 16% PAni-PMMA. The results for the mats of 20 wt% PAni blended with PEO are shown in Figure 27. The ratio σ_m/σ_f scales almost linearly with the orientation factor. The results for 67% PAni-PEO, and 16% PAni-PMMA showed similar trends. The linearity of this relationship confirms the accuracy of the orientation correction factor expressed by Eq. 14.

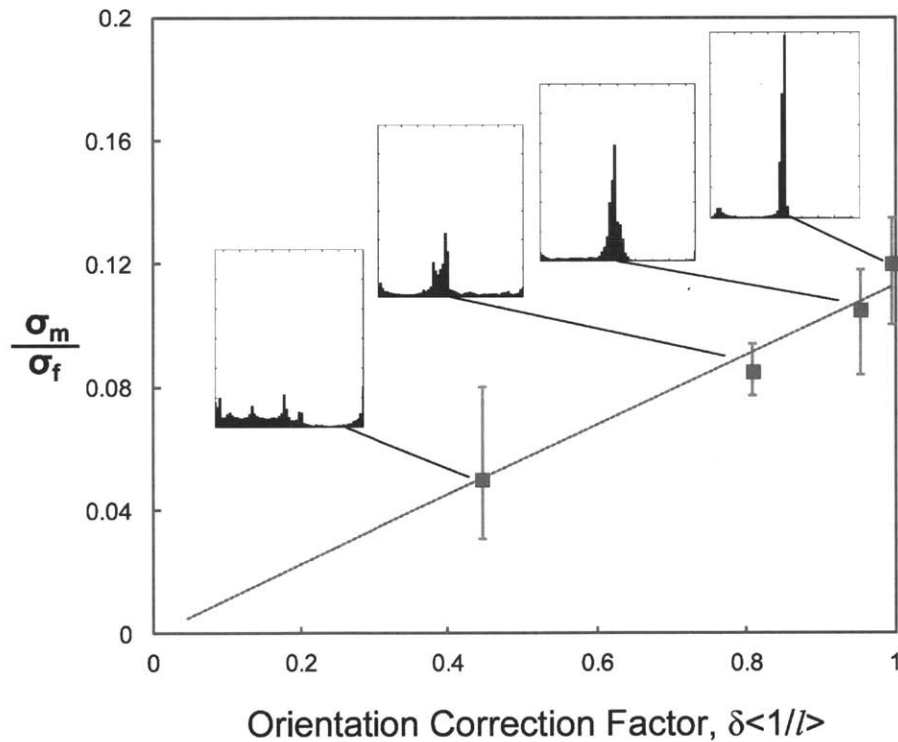


Figure 27 Correlation between dimensionless conductivity ratio (mat to fiber) and orientation distribution of fibers in the mat for samples with 20 wt% PAni blended with PEO. The insets show histograms of the angular orientation distribution for each sample from SEM image analysis. For each inset, the abscissa ranges from -90° to 90° , while the ordinate goes from 0 to 12000 counts

4.4.5 Mat-Fiber Conductivity Parity Plot & Discrepancies

Finally, Figure 28 shows a parity plot of the experimentally-measured mat conductivity versus the mat conductivity predicted by the model for different fiber mat compositions, based on the experimentally-observed fiber conductivity, porosity and fiber orientation distribution according to Eq. 15,. The results show that the model predicts the mat conductivity quite well, although for most samples the predicted value is slightly higher than the experimentally-measured mat conductivity.

The most likely source of the discrepancy between the measured and calculated mat conductivities is the curvature of the fibers in the mat. As observed previously by Pai et al.,⁶⁰ the curvature (or “curl”) of electrospun fibers in fiber mats tends to be more important for fibers of smaller diameter. In fiber mats where the diameters of individual fibers are around several hundred nanometers, the average radius of curvature was found to be on the order of 10 to 100 μm , which is much smaller than the dimensions of the mat samples measured in this study. The net effect of fiber curvature is a longer conduction path from one electrode to the other, so the model based on straight fibers overestimates the mat conductivity slightly.

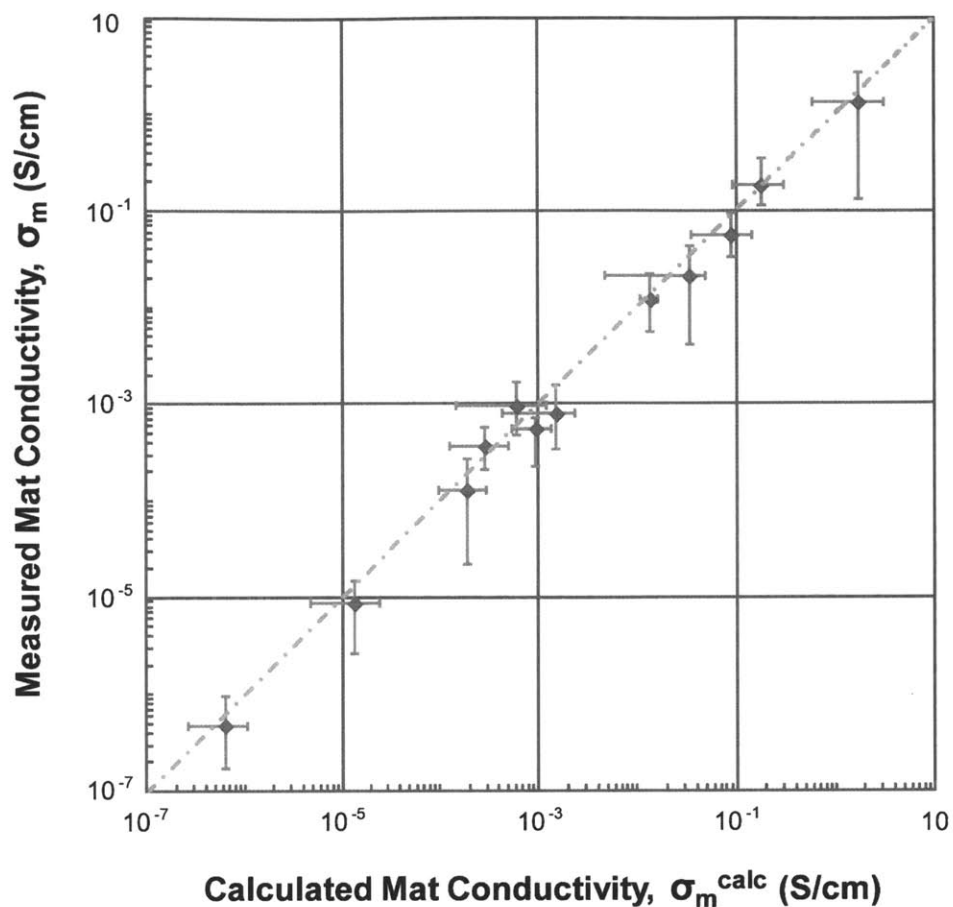


Figure 28 Parity plot of the experimentally-observed mat conductivity versus that calculated by the model for PANi-blend and PANi fibers

Another possible source of discrepancy is the neglect of conductive contacts between fibers. Fibers that do not provide a conductive path from one electrode to the other may nevertheless contribute to the mat conductivity measurement if they make conductive contact with another fiber that touches the other electrode. However, this effect would lead to the systematic underprediction of mat conductivity, which is not observed.

5.1 Gas Sensing Tests

Several recent studies have reported the development of different types of gas sensors in which nanofibers or nanowires are used to detect trace amounts of harmful gases effectively and rapidly.^{61 62 63 64} For this purpose, electrically conductive polymer nanofibers have been suggested as promising candidates for sensing materials.⁶⁵ Their unique combination of high specific surface area, mechanical flexibility, room-temperature operation, low cost of fabrication, and large range of conductivity makes these materials particularly attractive as nanoscale resistance-based sensors.^{66 67}

PAni doped with HCSA produced from coaxial electrospinning is particularly suited to the application of gas sensing because of the ease with which its conductivity is modified. The activity of the dopant can be switched reversibly between oxidation and reduction states simply by exposure to acidic and basic gases, respectively.^{68 69} These fibers were also shown to exhibit high electrical conductivities when fully doped, and thus present a broader range of tunable conductivity to work with during gas sensing than most of the similar systems thus reported.⁷⁰

Gas sensing tests were conducted in a quartz tube placed inside a Lindberg Blue TF 55035A furnace,⁷¹ where exposure of the samples to different concentration of gases was achieved using mass flow controllers (MFC) on separate streams of test gases and inert background gas. The temperature of the tube furnace was left at room temperature (20°C) and

not adjusted. The experiments were conducted inside the furnace in order to avoid any additional effects from external illumination. The setup is shown in the illustration in Figure 29.

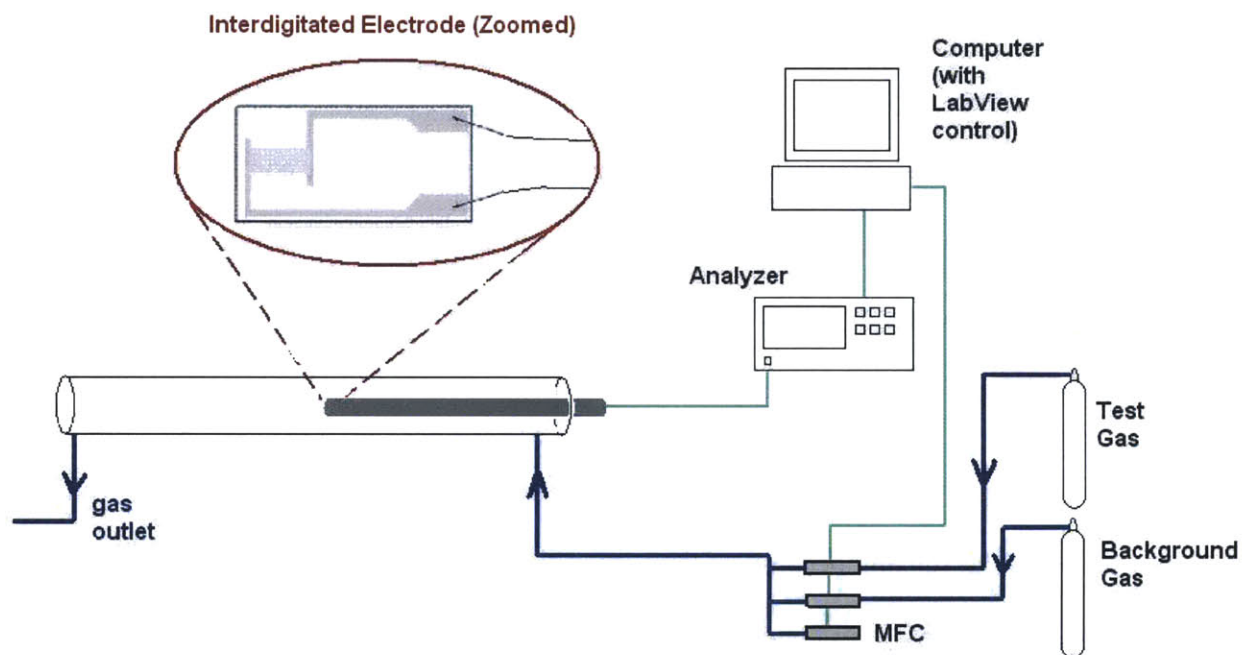


Figure 29 Illustration of gas sensing apparatus, including the tube furnace, the location of the interdigitated electrodes (IDE) (zoomed in), the mass flow controllers (MFC), the computer for LabView control and data collection and analyzer interface

Both ammonia (NH_3) and nitrogen dioxide (NO_2) gases were identified as candidates for sensing with the PANi fibers. All experiments were conducted with a constant total gas flow rate of 200 sccm. For NH_3 sensing, a certified premixed gas containing 1000 ppm of NH_3 in dry nitrogen was diluted with additional dry nitrogen gas by MFC's to a concentration in the range of

10 to 700 ppm of NH₃; for NO₂ sensing, a certified premixed gas containing 100 ppm of NO₂ in dry air was diluted with additional dry air to a concentration in the range of 1 to 50 ppm of NO₂. For each sample, about 10 aligned electrospun fibers were deposited on an IDE with 10µm finger spacings. The contacts from the interdigitated electrodes to the testing set-up were made by platinum wires. The DC resistances between the measurement portals in the quartz tube were measured by an Agilent HP34970A data acquisition system controlled by a LabView program and interface. For NH₃ sensing, the reported $\Delta R/R_0$ values are the ratios of the change in resistance over the original measured resistance (R_0), so that

$$\frac{\Delta R}{R_0} = \frac{R_{ex} - R_0}{R_0} \quad (16)$$

where R_{ex} is the final measured resistance after exposure. For NO₂ sensing, the reported $\Delta R/R_{ex}$ values are the ratios of the change in resistance over the final resistance, as shown in Eq. 17

$$\frac{\Delta R}{R_{ex}} = \frac{R_0 - R_{ex}}{R_{ex}} \quad (17)$$

The reported resistance values are averaged over at least three repeats. The sensitivity of the materials to gas sensing is defined as the ratio between $\Delta R/R$ and the concentration of the test gas, in units of ppm⁻¹, usually taken at low concentrations of gases where there is a linear relation between these two quantities.

5.2 Sensitivities and Response Times

5.2.1 Ammonia Sensing

The PANi fibers with HCSA: PANi mole ratio of 1, both as-electrospun (620nm in diameter) and after solid-state drawing (450nm in diameter), were used for sensing experiments with NH_3 for concentrations from 10 to 700ppm. PANi doped with HCSA exhibits *p*-type semiconductor characteristics, so exposure to electron-donating species such as NH_3 gives rise to a decrease in the charge-carrier concentrations and thus a decrease in the conductivity.

The gas sensing responses are fast, as demonstrated by a representative plot shown of $\Delta R/R_0$ for drawn PANi fiber with diameter of 450nm in Figure 30. PANi fibers of 450nm were exposed to repeated cycles of 5 min exposure to a gas stream of 500ppm of ammonia (balance nitrogen) followed by 5 min of nitrogen purging. The response time is defined as the time required for the signal to reach $1/e$ of its steady state value. For the case shown in Figure 30, the average response times are about 45 seconds upon exposure, and about 63 seconds for purging.

The results also show that the measurement was reasonably reversible; the maximum $\Delta R/R_0$ value did not vary much over multiple cycles of exposure to the same concentration of gases, so that the fibers can be used multiple times for sensing. However, there was an increase of baseline resistance after the first cycle in some cases, as seen in the case shown in Figure 30, indicating that nitrogen purging is not enough to return the fibers to the original state, i.e., some ammonia molecules have irreversibly reacted with or bound to the fibers. The baseline does not

increase after subsequent cycles, so that the sensing measurements are reversible after the first cycle of exposure in all cases.

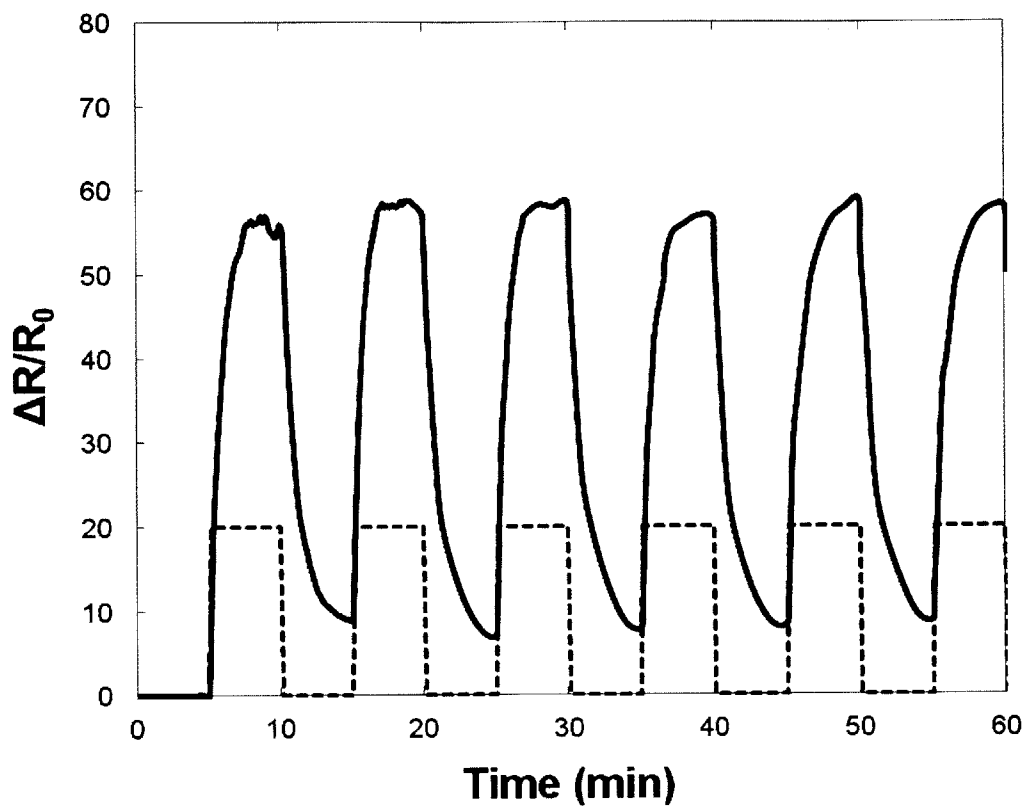


Figure 30 Time response of drawn PANi fiber (450nm in diameter) under cyclic exposure of 500ppm of ammonia; superimposed line indicates the change in ammonia concentration from 0 to 500ppm

Table 8 Characteristic Response Times of As-Spun and Solid-State-Drawn PANi/HCSA Fibers during Ammonia Exposure and Nitrogen Purge

NH ₃ Concentration (ppm)	Response time (s) for as-spun PANi fiber		Response time (s) for solid-state drawn PANi fiber	
	Exposure	Purging	Exposure	Purging
20	84 ± 6	133 ± 8	82 ± 3	109 ± 9
50	82 ± 4	92 ± 4	67 ± 5	84 ± 4
100	66 ± 6	75 ± 2	59 ± 8	83 ± 5
500	43 ± 3	61 ± 8	45 ± 3	63 ± 9
700	31 ± 4	53 ± 6	28 ± 5	47 ± 7

PAni fibers were then subjected to longer exposures of ammonia for concentrations ranging from 10 to 700ppm. Table 8 lists the characteristic response times (averaged over at least three cycles) of the as-spun and solid-state drawn PANi fibers under different levels of ammonia exposure. Response times decrease monotonically with increasing ammonia concentration. The response times under nitrogen purging are significantly longer than the exposure responses times. When comparing the as-spun and solid-state drawn PANi fibers, the drawn fiber tend to have slightly faster response times, but the difference is not significant. The difference could be due to both the smaller fiber diameter and the high level of molecular orientation that comes with solid state drawing. In general, 10 minutes is sufficient for the signals to reach steady state during both exposure and purging, as shown in the time response of fibers to exposure of different concentration of ammonia in Figure 31.

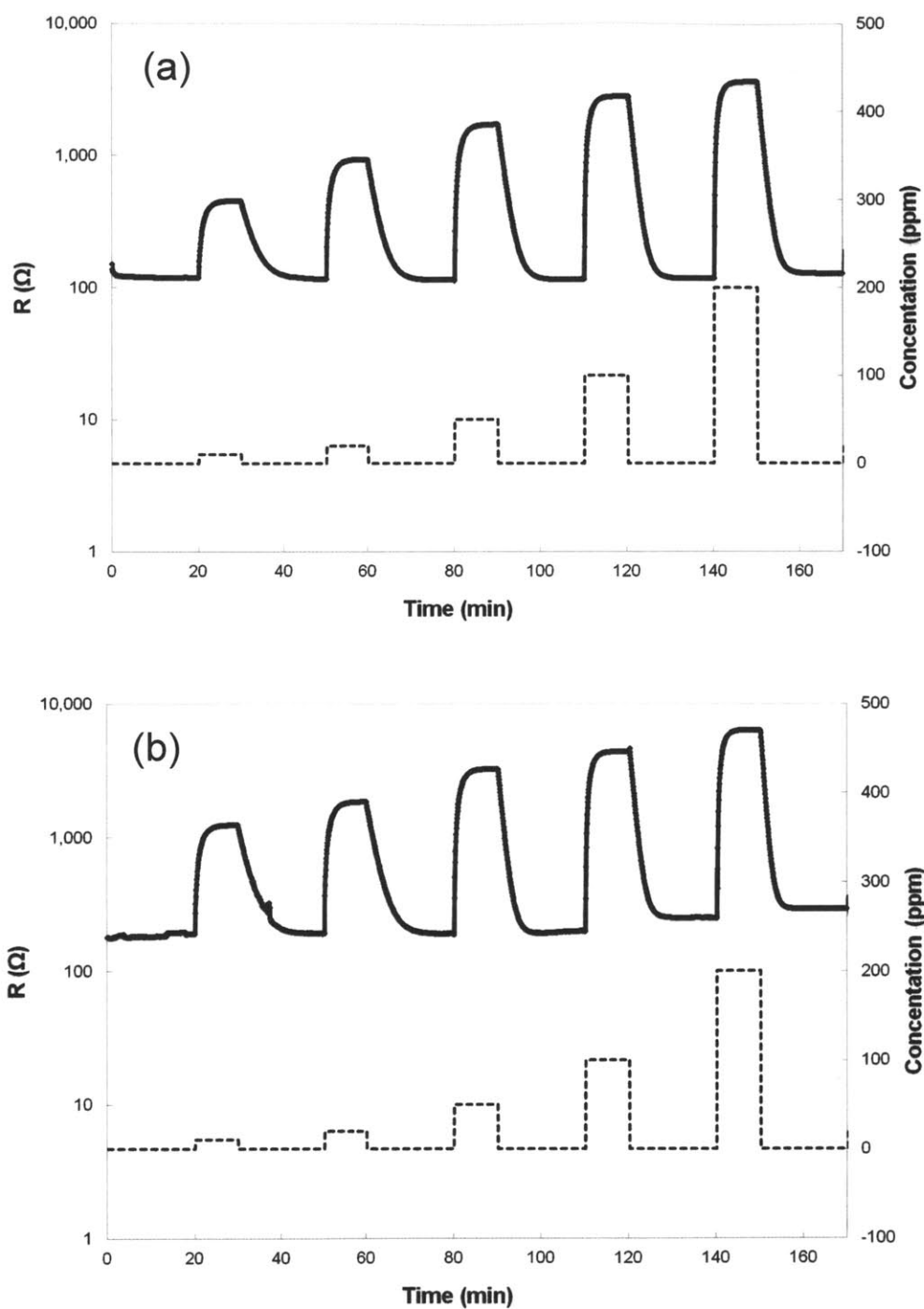


Figure 31 Time response of (a) as-spun doped PANi fibers and (b) solid-state drawn doped PANi fibers, to different concentrations of NH₃; dotted lines show the change in NH₃ concentrations

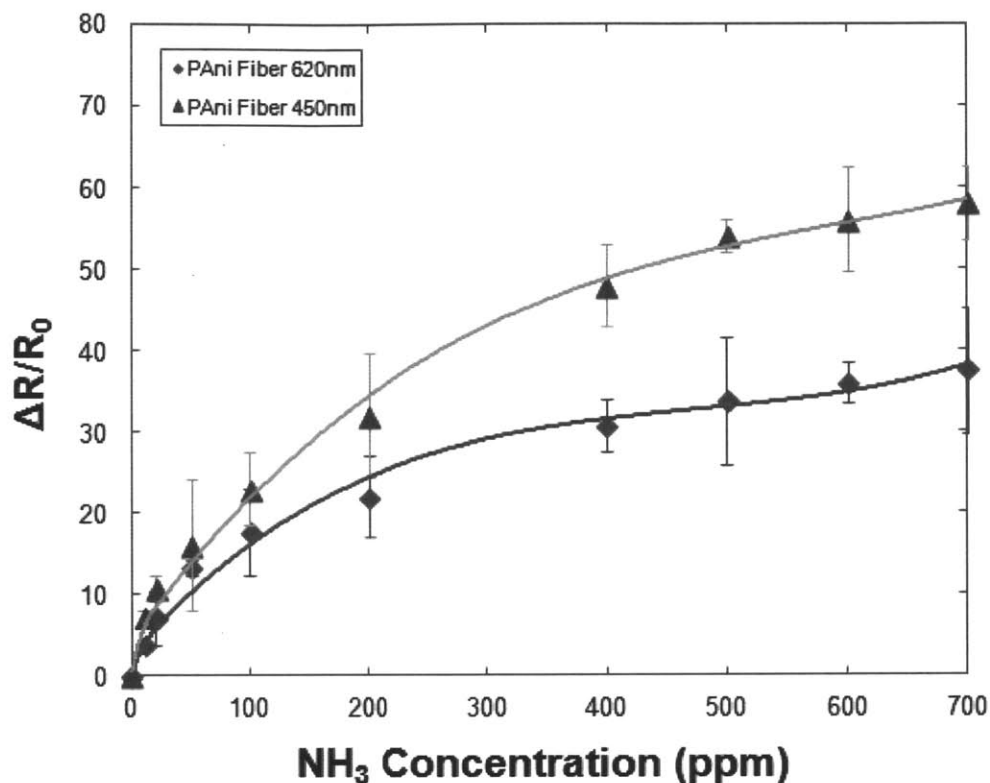


Figure 32 Resistance modulation upon exposure of doped electrospun PANi fibers to different concentrations of ammonia gas

The steady-state responses read after 10 min exposures of ammonia are shown in Figure 32 as a function of increasing ammonia concentration from 10 to 700ppm. The measured resistances of the HCSA-doped PANi fibers increase dramatically upon exposure to NH₃. Responses as large as $\Delta R/R_0 = 38$ for as-spun PANi fiber with diameter of 620nm, and $\Delta R/R_0 = 58$ for drawn PANi fiber with diameter of 450nm. Such large ranges of modulation are among the highest thus far reported for PANi and PANi-composite fibers, and are advantageous for gas sensing where signal-to-noise ratios can be an issue.⁷² In the linear region of exposure to

concentrations below 20ppm of ammonia, the sensitivity of the 620nm fiber is 3.5 ppm^{-1} , and the sensitivity of the 450nm fiber is 5.5 ppm^{-1} , both of which are much higher than the sensitivity of a cast film of the same material with $10\mu\text{m}$ thickness, measured at 0.02 ppm^{-1} . The ammonia exposure limit in the US is 25ppm over an eight-hour period and 35ppm over a short-term exposure.⁷³ The level of sensitivity exhibited by these fibers is sufficient for rigorous environmental monitoring under these conditions.

5.2.2 Nitrogen Dioxide Sensing

Next, the undoped PANi fibers (i.e., HCSA: PANi ratio of 0) were used for NO_2 gas sensing. In contrast to NH_3 , which is electron-donating, NO_2 is electron-withdrawing and thus acts as dopant in lieu of HCSA to increase the charge carrier concentration of *p*-type PANi. Consequently, upon exposure to NO_2 the electrical conductivities increase and measured resistances decrease.

The representative time response shown in Figure 33 was for the exposure of undoped pure PANi electrospun fibers to different concentrations of NO_2 . Similar to the NH_3 sensing system, it also shows quick response times and good recovery. Table 9 lists the characteristic response times of the undoped PANi fibers to NO_2 exposure. The response times are on the order of 50 s for exposure and 70 s for purging, and do not vary much within the range of concentrations from 1 to 50ppm.

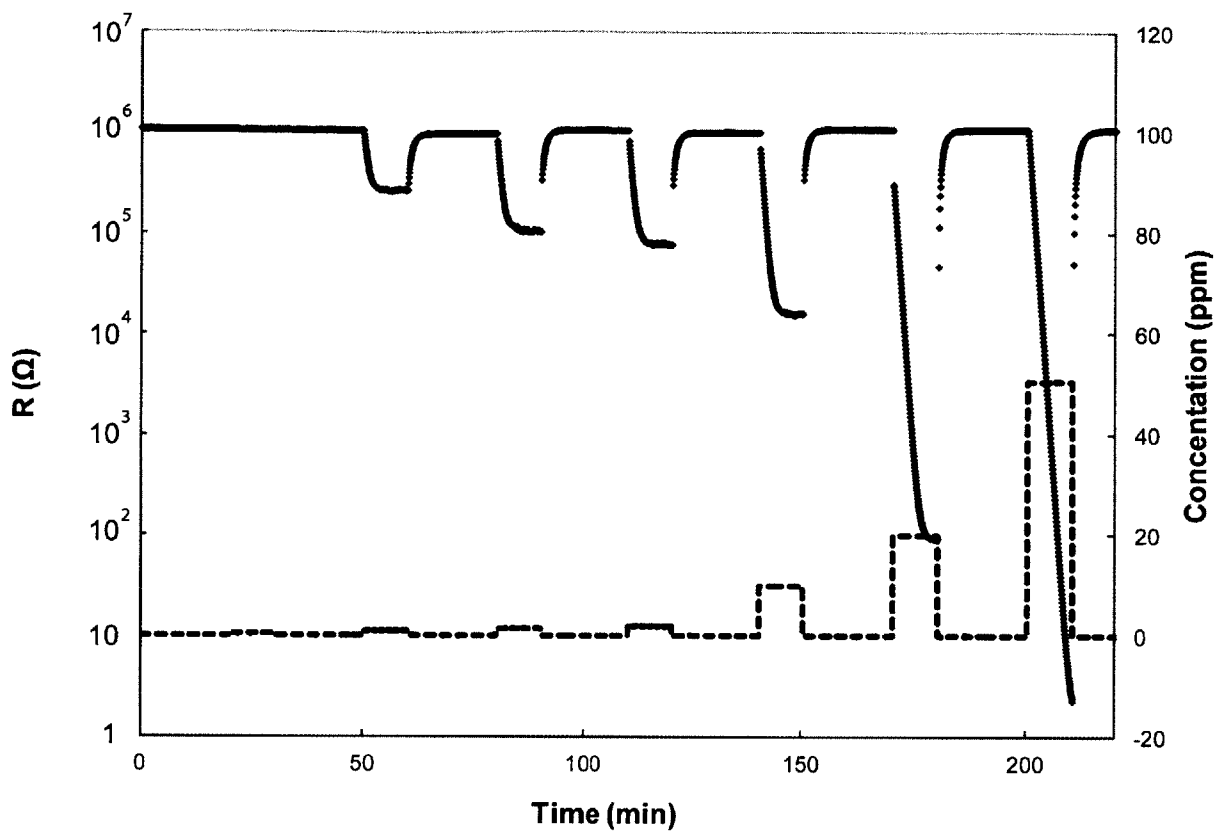


Figure 33 Time response of undoped PANi fiber to different concentrations of NO₂; dotted line shows the change in NO₂ concentrations

Table 9 Characteristic Response Times of Undoped PANi Fibers during NO₂ Exposure and Purge

NO ₂ Concentration (ppm)	Response Time (s)	
	Exposure	Purging
1	55 ± 5	68 ± 8
2	50 ± 9	71 ± 6
5	48 ± 3	62 ± 5
10	45 ± 3	61 ± 8
20	43 ± 3	67 ± 8
50	46 ± 5	82 ± 9

Figure 34 shows the response of the undoped PANi fibers to NO₂ exposure with concentrations in the range between 1 and 50ppm. The reported $\Delta R/R_f$ values are taken after 10 minutes of sustained exposure. It shows remarkable resistance decrease (conductivity increase) at low NO₂ concentrations between 1 and 50ppm. The huge range of modulation, up to almost 6 orders of magnitude, indicates that the pure PANi fibers used are very effective NO₂ sensors, changing PANi from its undoped, insulating state to the almost fully doped high-conductivity state. The modulation at 1ppm is a more than 5-fold resistance decrease, indicating very good sensitivity at even very low concentrations of NO₂ exposure. The exposure limit set by the environmental agencies in the US for NO₂ is 50ppb,⁷⁴ which is a concentration too low to be tested directly with the gas composition and flow controllers available. However, based on

extrapolation it is reasonable to expect more than 15% resistance change from the PANi fibers, which should be easily detectable. With its large modulation range and quick responses, this PANi fiber can serve as a very effective nanoscale sensor for NO₂.

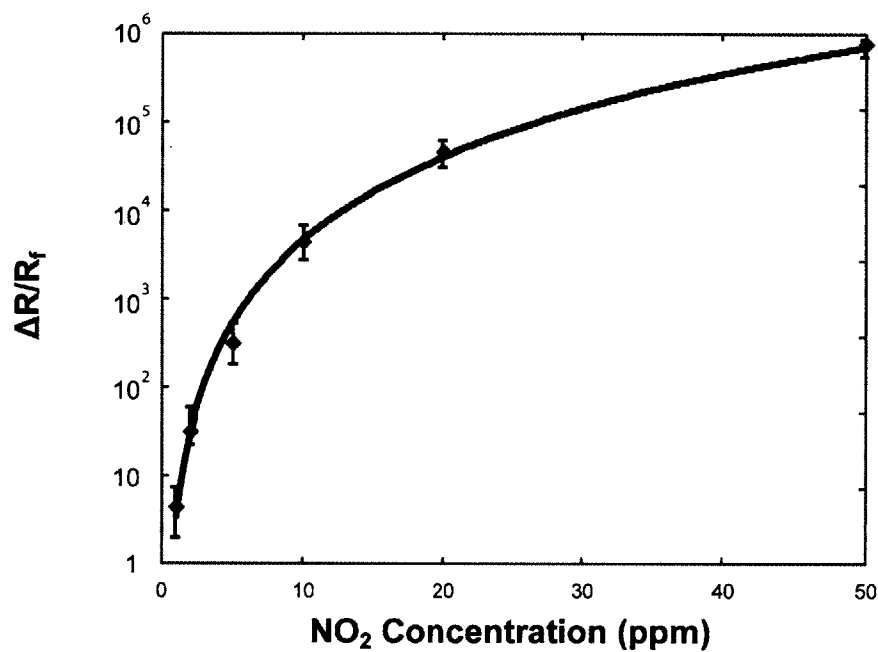
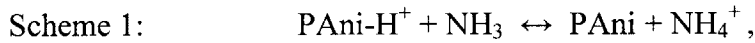


Figure 34 Resistance modulation upon exposure of undoped electrospun PANi fiber to different concentrations of NO₂ gas

5.3 Reaction-Diffusion Model for Gas Sensing by Fibers

5.3.1 Reaction Equilibrium

A major difference between the experimental results for NH₃ and NO₂ sensing is that the $\Delta R/R_{ex}$ for NO₂ undergoes changes in resistance up to 6 orders of magnitude, while the $\Delta R/R_0$ for NH₃ exhibits less than two orders of magnitude of modulation. It is clear from the value for conductivity in Table 6 that the whole range of doping levels is not being explored in the NH₃ case. The most likely explanation is that ammonia, being a relatively weak base, does not fully deprotonate the doped PANi in the presence of the acidic HCSA, even at concentrations as high as 700 ppm. This can be explained by a reaction equilibrium between the doped PANi and NH₃:



and the equilibrium lies somewhere in the middle rather than to either extreme, i.e.,

$$\frac{[PANi]}{[PANi-H^+]} = \frac{K[NH_3]}{[NH_4^+]} \sim 1. \quad (18)$$

On the other hand, because the PANi fibers used for nitrogen dioxide sensing were undoped, the incoming NO₂ serves as the only available acidic dopant for PANi; there is no competing strong acid/base in the system. The huge change of conductivity suggests that the reaction is mostly irreversible or the equilibrium lies very much to the right (K approaches ∞).

5.3.2 Response as a Function of Radial Electrical Conductivities

To characterize the changes in resistance observed in this work, we model the fibers as simple cylindrical elements in which gases diffuse radially into the fiber upon exposure. The model is simplified by assuming that the chemical composition (and thus conductivity) of the fibers varies only with radial position, so that the overall observed change in resistance can be expressed as

$$\frac{R_{ex}}{R_0} = \frac{\sigma_0 L^2}{2 \int_0^L \sigma(\Phi(r)) r dr} \quad (19)$$

where r is the radial position in the fiber, L is the characteristic length, which is the fiber radius in this case, σ_0 is the fiber conductivity prior to exposure, and $\sigma(\Phi(r))$ is the radially varying conductivity as a function of concentration of the reactive component in the fiber ($\Phi(r)$) and thus a function of r . This model can be thought of as concentric rings in the fiber forming parallel conducting pathways throughout the length of the fiber, with the inverse of total resistance for the fiber being the sum of the inverse resistances (conductivities) for each concentric ring weighted by its respective cross-sectional area.

5.3.3 Time-Dependent Reaction-Diffusion Model

A reaction-diffusion model can be used to model both the spatial and temporal changes in the electrospun fibers upon gas exposure. With the assumption that the reaction is reversible and first order with respect to each of its reactants and products, the concentration changes can be described generically by the following system of partial differential equations:

$$\frac{\partial \Theta}{\partial \tau} = \frac{1}{r} \frac{\partial}{\partial r} \left(r \frac{\partial \Theta}{\partial r} \right) + \alpha \left[-\text{Da} \Theta \Phi + \frac{\text{Da}}{K} \Omega \Psi \right] \quad (20)$$

$$\frac{\partial \Phi}{\partial \tau} = -\text{Da} \Theta \Phi + \frac{\text{Da}}{K} \Omega \Psi \quad (21)$$

$$\frac{\partial \Omega}{\partial \tau} = \alpha \left[\text{Da} \Theta \Phi - \frac{\text{Da}}{K} \Omega \Psi \right] \quad (22)$$

$$\frac{\partial \Psi}{\partial \tau} = \text{Da} \Theta \Phi - \frac{\text{Da}}{K} \Omega \Psi \quad (23)$$

Here, Θ is the normalized concentration of the diffusing gaseous reactant (e.g. NH_3 or NO_2), Φ is the normalized concentration of the non-diffusing reactant (e.g. PAni or PAni-H^+), Ψ is the normalized concentration of the polymeric product of reaction (e.g. PAni-H^+ or PAni), Ω is the normalized concentration of the other product of reaction (e.g. NH_4^+ or NO_2^-). r is the normalized radius r/L . τ is the dimensionless time $\tau = \frac{t}{t_D} = \frac{tD}{L^2}$ with D being the diffusivity of the diffusing gaseous reactant in the fiber. Da is the Damköhler number, defined with respect to the

forward reaction and reference concentration of Θ , so that $Da = \frac{k_f C_{o,\Theta} L^2}{D}$. K is the equilibrium

constant of the reaction, also the ratio of the forward to reverse reaction rate constants $K = \frac{k_f}{k_r}$.

α is the dimensionless ratio of the reference concentrations for the non-diffusing and diffusing

reactant: $\alpha = \frac{C_{o,\Phi}}{C_{o,\Theta}}$. Because of their corresponding stoichiometric ratios, the reference

concentration of Ψ , $C_{o,\Psi}$, is set to be equal to the reference concentration of Φ , and the reference

concentration of Ω , $C_{o,\Omega}$, is set to be equal to the reference concentration of Θ . Eq. 20 expresses

the dynamics for the concentration of the gaseous reactant, which includes diffusion down a

concentration gradient, consumption by the forward reaction and production by the reverse

reaction. Eq. 22 expresses the dynamics for the concentration of the product formed from the

gaseous reactant; as the product is generally ionic and believed to bind closely with the

oppositely charged ions on the polymeric substrate, the dynamics do not include diffusion

(assumed to be negligible), but includes only production by the forward reaction and production

by the reverse reaction. Eq. 21 (or 23) expresses the dynamics for the concentration of the

polymeric reactant (product), which includes only consumption (production) by the forward

reaction and production (consumption) by the reverse reaction.

With the specification of appropriate boundary and initial conditions, this system can be solved numerically by MATLAB for specified values of the parameters. If one assumes that only the non-diffusing polymeric reactant is present in the system initially, and the initial

concentrations of solute species (both reactant and product) are zero, the boundary and initial conditions for the cylindrical system can be described as follows:

$$\Theta(1, \tau) = 1, \quad \frac{\partial \Theta}{\partial r}(0, \tau) = 0, \quad \Theta(r, 0) = 0$$

$$\Phi(r, 0) = 1$$

$$\Omega(r, 0) = 0$$

$$\Psi(r, 0) = 0$$

Figure 35 shows the results of this reaction-diffusion model, where the ratio of initial to final resistances is plotted as a function of Da and τ at selected values of $K = \infty, 100, 1,$ and 0.1 . For these calculations, we assume that the initial concentrations of small molecular solute species are zero, and that the conductivity of a section of the fiber decreases linearly with the concentration of the reactant Φ .

One can see that the resistance increases (R_0/R_f decreases) monotonically with τ for all values of Da and K. If Da is very large, the reaction is much faster than the diffusion; the diffusion front is very sharp but penetrates slowly into the fibers. If Da is very small, diffusion is much faster than reaction, so that the concentration profile is almost flat within the fiber; the gas rapidly penetrates the entire fiber. However, it may still take a long time (on the dimensionless scale) for the diffused gas to react and cause the necessary change in conductivity, as shown in radial concentration profiles in Figure 36. Significantly, there exists a minimum in R_0/R_f with respect to Da at any given τ , except for the case of $K = \infty$ where the forward reaction is irreversible. Therefore, there exists an optimal Da value for the overall resistance of the fiber to change at the fastest rate. This suggests that systems can be optimized with respect to Da for all

such reversible reactions. Recalling that $Da = \frac{k_f C_{o,\theta} R^2}{D}$, such optimization can be performed for a specific application by designing the fiber diameter for the target exposure concentration. Indirectly, Da can also be altered by changing the fiber material, gas species, or temperature, factors that all affect the reaction rate constant and diffusivity.

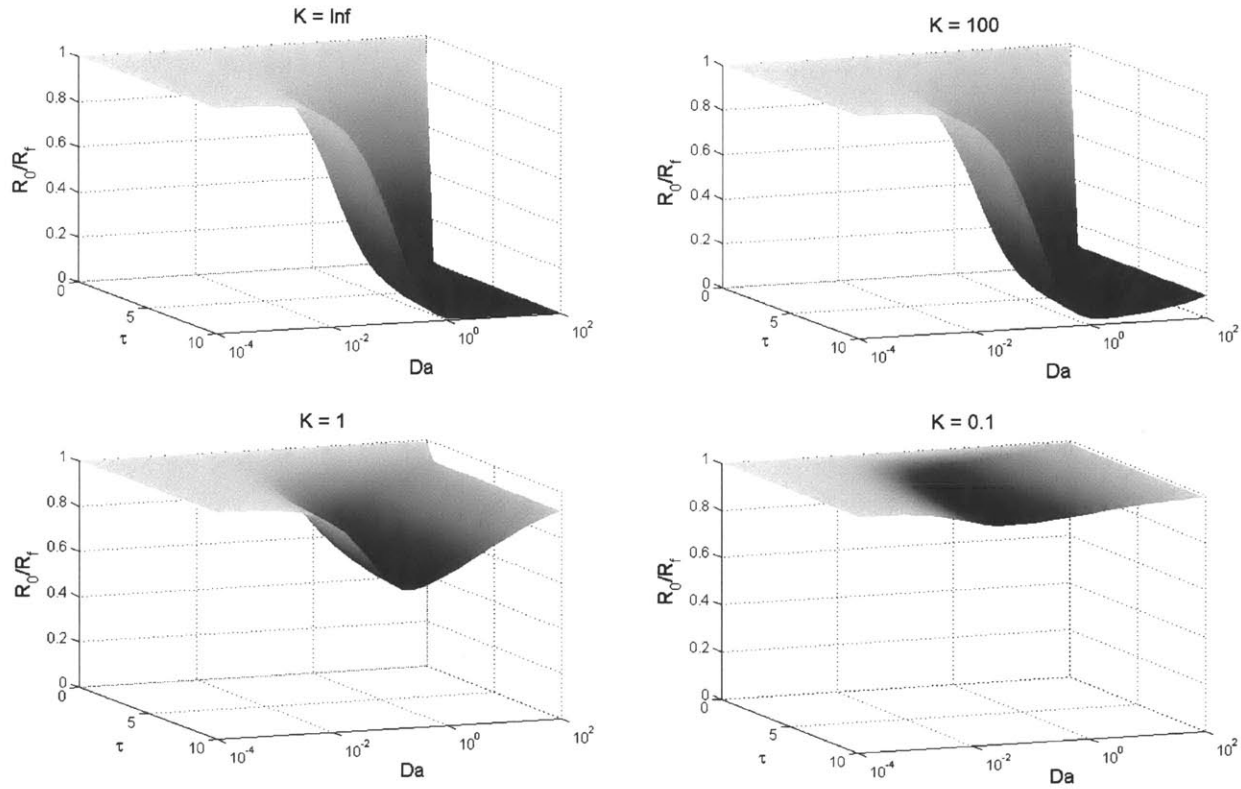


Figure 35 Results of reaction-diffusion model showing the ratio of initial resistance to final resistance as a function of Damköhler number (Da) and dimensionless time (τ) for selected values of equilibrium constant (K). Calculations assume that no gaseous reactant or products are present in the fibers as the initial condition, and the conductivity of the fiber decreases linearly with the concentration of the reactant Φ

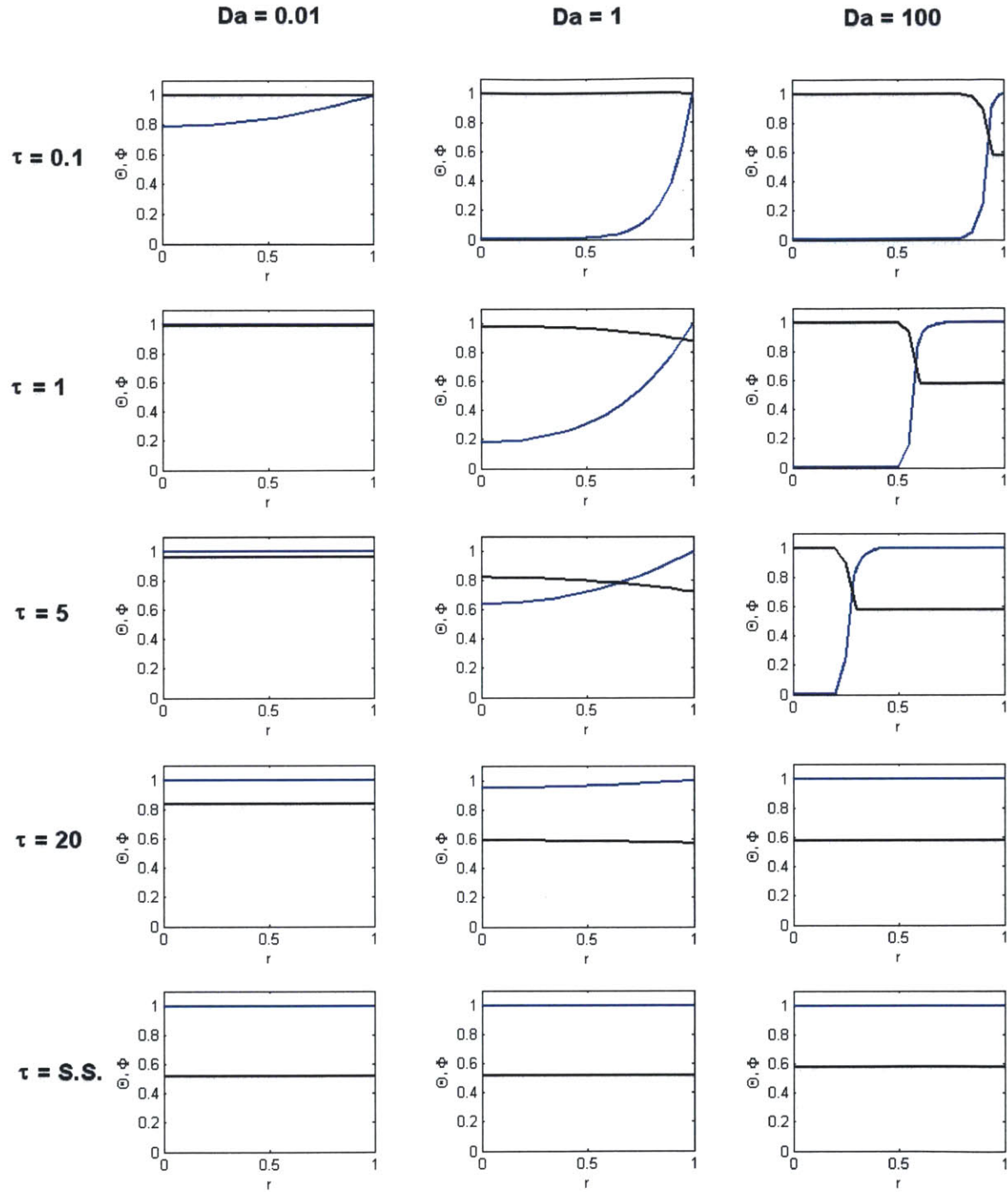


Figure 36 Results of radial concentration profiles of Θ (blue lines) and Φ (black lines) for combinations of Da and τ at $K = 1$; in the last row, S.S. refers to steady state which is reached at large τ values

5.3.4 Equilibrium Determination from Steady-State Data

The three variables in the modeled system are Da , K , and τ . The determination of the value of K can be achieved from fitting the steady-state data.

At steady state, where there is no longer dependence on time, the system of equations simplifies to:

$$\frac{\partial \Theta}{\partial \tau} = \frac{1}{r} \frac{\partial}{\partial r} \left(r \frac{\partial \Theta}{\partial r} \right) = 0 \quad (20')$$

$$\frac{\partial \Phi}{\partial \tau} = -Da \Theta \Phi + \frac{Da}{K} \Omega \Psi = 0 \quad (21')$$

$$\frac{\partial \Omega}{\partial \tau} = \alpha \left[Da \Theta \Phi - \frac{Da}{K} \Omega \Psi \right] = 0 \quad (22')$$

$$\frac{\partial \Psi}{\partial \tau} = Da \Theta \Phi - \frac{Da}{K} \Omega \Psi = 0 \quad (23')$$

where equations (21'), (22') and (23') all reduce to the definition of the equilibrium constant being the ratio of the four concentrations at equilibrium, and equation (20') gives that the concentrations have no more radial dependence, either, at steady state. As the concentrations, and thus the fiber electrical conductivity, is no longer dependent on radial position in the fiber, this leads to the simplification in equation 19 that

$$\frac{R_{ex}}{R_0} = \frac{\sigma_0}{\sigma_{ex}} \quad (19')$$

Equation (19') can be used to replot the results for $\Delta R/R$ vs. gas phase concentration experimental data (at steady state) as a relationship between dedoped conductivity σ_{ex} and gas phase concentration.

Take the system of ammonia sensing, for example, once the experimental steady state data have been converted to a plot of σ_{ex} vs. gas phase ammonia concentration, it can be converted further to a plot such as Figure 37 using calibration curve based on results for conductivity vs $[HCSA]/[PAni]$, to show the relationship between fraction of PAni doped versus the external ammonia concentration.

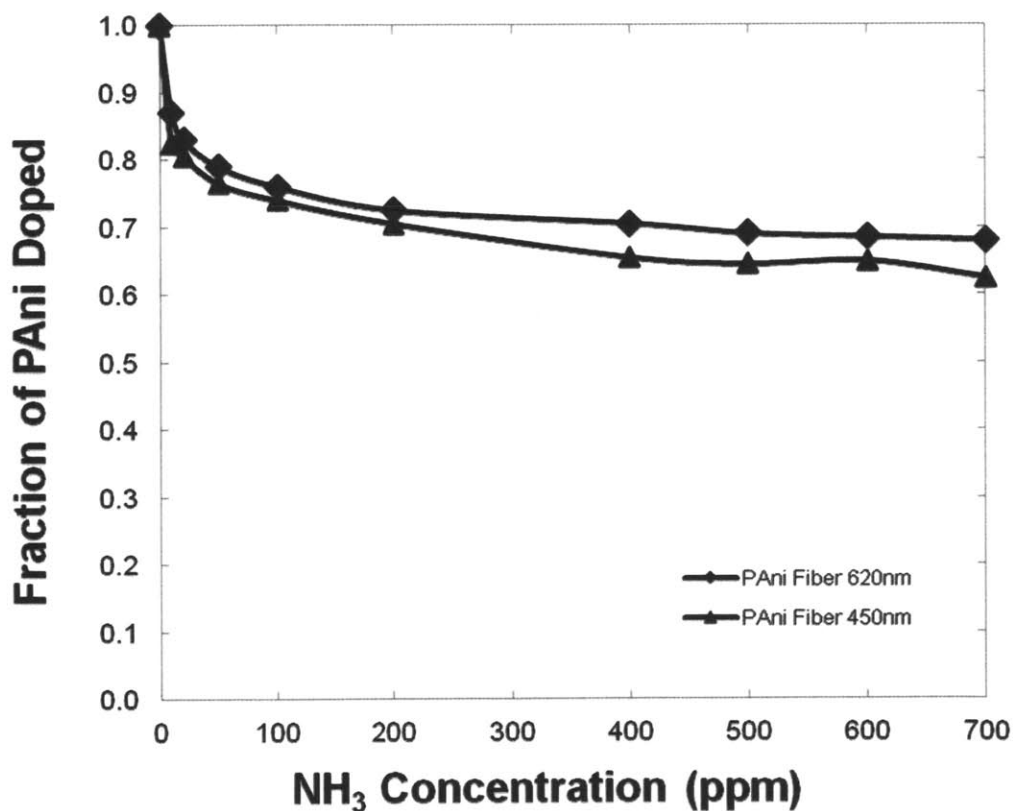


Figure 37 Equilibrium fraction of PAni doped (after partial dedoping by the gas) in the fibers derived from sensing responses at different ammonia concentrations

Since by mass balance $[PAni - H^+] + [PAni] = [PAni]_0$, where the last concentration is the original concentration of PAni present in the fibers, regardless of doping levels, the fraction of doped PAni can be derived from the equilibrium constant definition and represented as

$$\frac{[PAni - H^+]}{[PAni]_0} = \left(\frac{K[NH_3]_s}{[NH_4^+]_s} + 1 \right)^{-1} = 1 - \frac{K[NH_3]_s}{K[NH_3]_s + [NH_4^+]_s} \quad (24)$$

where all concentrations of ammonia and ammonium ion are those in the fiber.

For all data points in Figure 37, each fraction of PAni doped can then lead to a value of $\frac{K[NH_3]_s}{[NH_4^+]_s}$ according to equation 24. The steady-state concentration of ammonia in the fiber is set by the exposed gas phase concentration of ammonia by a partition coefficient, S , $[NH_3]_s = S[NH_3]_g$ according to Henry's Law. The concentration of dedoped PAni and ammonium ion will be equal to the extent of reaction, ξ , as neither was present in the fiber initially and neither species diffuses in the fiber. This leads to the expression of K to be expressed by the extent of reaction as follows

$$K = \frac{[NH_4^+]_s [PAni]}{[NH_3]_s [PAni - H^+]} = \frac{\xi^2}{S[NH_3]_g ([PAni]_0 - \xi)} \quad (25)$$

which becomes a quadratic equation in ξ

$$\xi^2 + SK[NH_3]_g \xi - SK[NH_3]_g [PAni]_0 = 0 \quad (26)$$

The non-negative root of the equation is thus

$$\xi = \frac{\sqrt{(SK)^2[\text{NH}_3]_g^2 + 4SK[\text{NH}_3]_g[\text{PAni}]_0 - SK[\text{NH}_3]_g}}{2} \quad (27)$$

The values of external ammonia concentrations are known, and for as-spun PAni fibers, $[\text{PAni}]_0 = 5.0 \times 10^3 \text{ mol/m}^3$, according to the known density and molecular weight. Assuming a set of values of SK , we can then solve for the extent of reaction corresponding to each

experimental data point, and obtain theoretical values for $\frac{K[\text{NH}_3]_s}{[\text{NH}_4^+]_s} = \frac{\xi}{[\text{PAni}]_0 - \xi}$ at each of the conditions. A least-squared residue analysis is then performed on the difference between experimental and theoretical values, and used to find the best fit for values of SK .

From the experimental steady-state data for the ammonia sensing by as-spun fibers (620nm in diameter), the value of the equilibrium constant SK is thus determined to be 1.5 ± 0.1 . The best-fit theoretical values are shown in Figure 38 as the solid line fitting the as-spun fiber data.

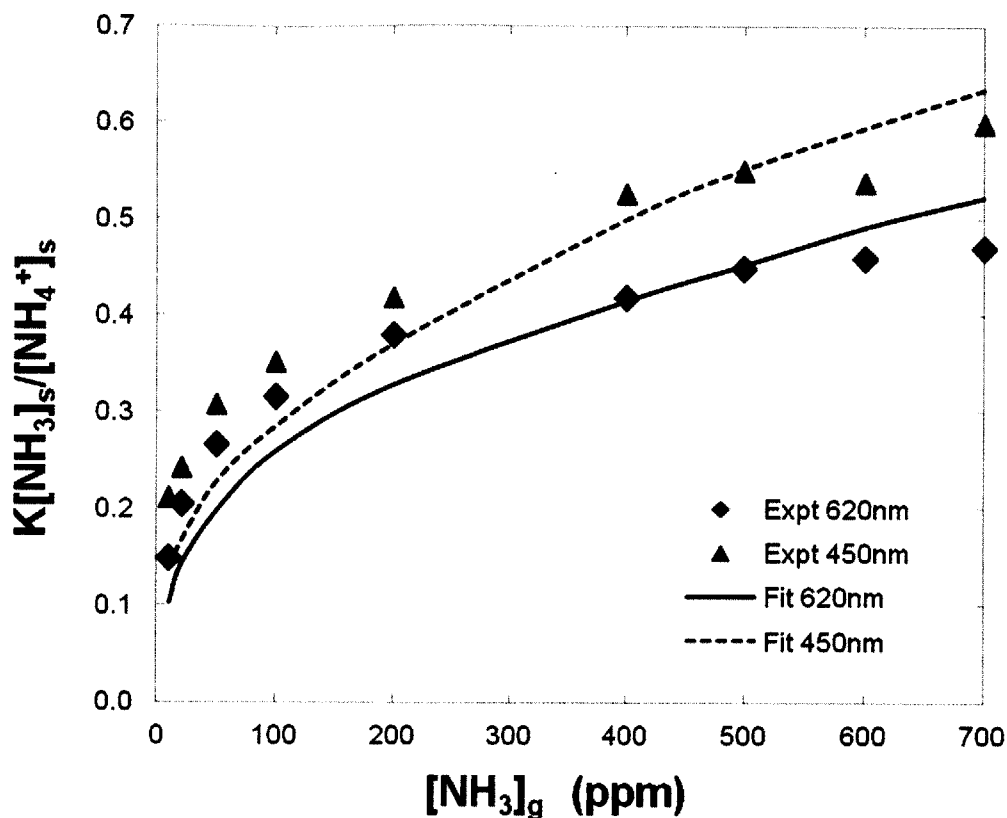


Figure 38 Comparison of experimental and fitted data for both as-spun and solid-drawn doped PANi fibers upon ammonia exposure with concentrations ranging from 10 to 700ppm

As can be seen from Figure 38, the two sets of experimental data from fibers of two different diameters are different at the same external gas concentrations. In the expression in Equation 27, S and K should both be independent of fiber diameter, so the most probable difference is the difference in the original PANi concentrations present in the fibers. Because the fibers with 450nm diameters have been solid-state drawn prior to performing sensing tests, their densities may have changed, resulting in a total PANi concentration lower than the 5.0×10^3 mol/m³ value assumed for as-spun fibers.

Keeping the fitted value of $SK = 1.5$, we have allowed $[\text{PAni}]_0$ to vary for the data from solid-state drawn fibers (450 nm diameter), and the least squared fit results in a value of $[\text{PAni}]_0 = 3.8 \times 10^3 \text{ mol/m}^3$. The best-fit is also shown in Figure 38 as the dotted line fitting data from the solid-state drawn fibers.

5.3.5 Fitting Parameters from Time-dependent Data

For ammonia sensing, in the Damköhler number $\text{Da} = \frac{k_f C_{o,\Theta} L^2}{D}$, the reference concentration of Θ is the concentration of ammonia at the most exterior of the fiber ($r = 1$), which is related to the exposed gas phase concentration of ammonia by a partition coefficient, S , $C_{o,\Theta} = [\text{NH}_3]_{s,r=1} = S[\text{NH}_3]_g$ according to Henry's Law. Under the assumptions that the reaction rate constant, diffusivity, and partition coefficients are not functions of gas concentration or fiber diameter, and the gas phase is well mixed, their ratio, $\frac{k_f S}{D} = \frac{\text{Da}}{[\text{NH}_3]_g L^2}$, is a constant parameter that can be fitted.

Assuming that $S = 1$, the value of K can then be determined from the steady-state data as $K = 1.5$, and the fitting parameter from Da can be reduced to $\frac{k_f}{D}$. The other unknown variable in the model is τ . As $\tau = \frac{tD}{L^2}$, and with known real time and fiber diameter, the fitting parameter from this dimension corresponds to the diffusivity, D . We can then fit the time-dependent sensing data with the modeled values to fit value for k_f and D , and perform optimization of the

sensing system. Figure 40 shows the reaction-diffusion model results for $K = 1.5$. A least-squares residue fitting using all time-dependent data for as-spun fibers (620nm diameter) measured with gaseous ammonia concentrations from 10ppm to 500ppm gives the value of D as $(1.3 \pm 0.2) \times 10^{-10} \text{ cm}^2/\text{s}$, and the value of k_f as $0.5 \pm 0.3 \text{ cm}^3/(\text{mol s})$. The comparison between experimental data and fitted values is shown in Figure 39.

These fitted values agree with the reported literature values where diffusion coefficient of ammonia in polymer on the order of 10^{-11} to $10^{-9} \text{ cm}^2/\text{s}$,⁷⁵ and k_f is on the order of 0.001 to 0.1 $\text{cm}^3/\text{mol/s}$.^{76 77}

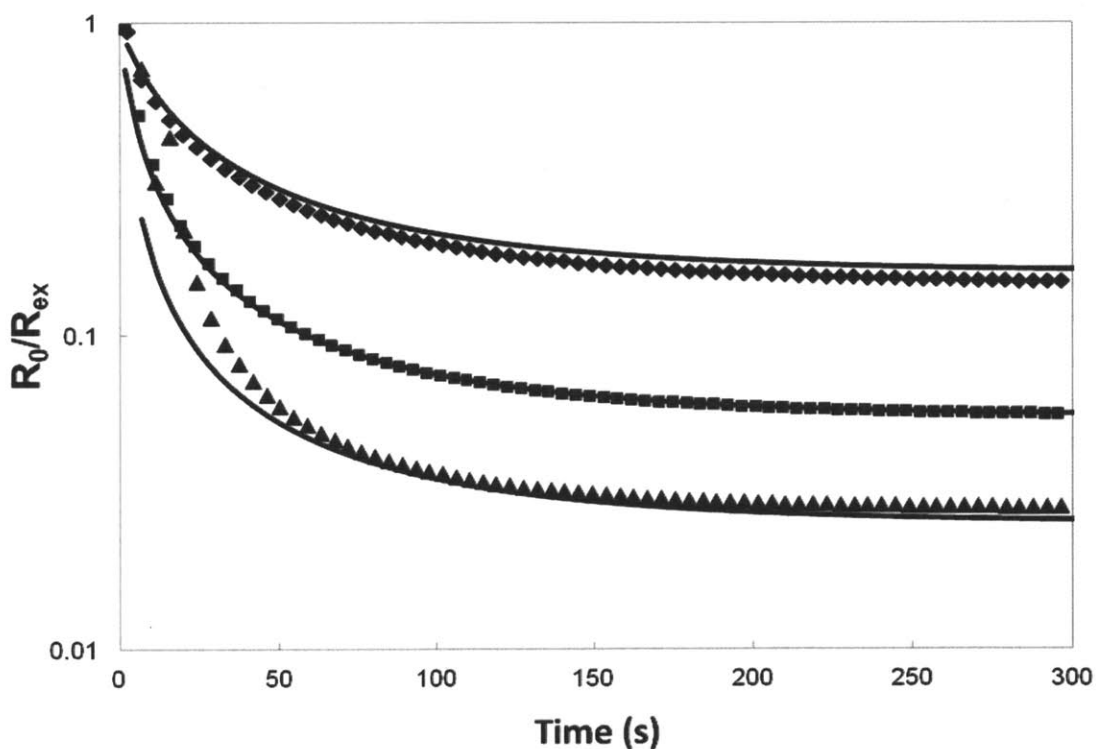


Figure 39 Comparison of experimental data (markers) and fitted values (solid lines) for three sensing response time series

5.3.6 Application of the Model for Design Optimization

For a predetermined time of detection, e.g., $t = 60$ s, if we take 450 nm PAni fibers at 500ppm of ammonia exposure as a starting point for optimization, with the fitted parameters we know that

$$\tau = \frac{tD}{L^2} = \frac{(60s)(1.3 \times 10^{-10} \text{ cm}^2 / s)}{(225 \times 10^{-7} \text{ cm})^2} = 15,$$

$$Da = \frac{k_f S}{D} [\text{NH}_3]_g L^2 = (4.0 \times 10^{13} \text{ m} / \text{mol}) \left(\frac{500}{10^6} \times \frac{1 \times 10^3 \text{ g} / \text{m}^3}{28 \text{ g} / \text{mol}} \right) (225 \times 10^{-9} \text{ m})^2 = 0.036.$$

The optimum condition for this value of τ , is found from the model plots to be at $Da = 0.18$ and $R_0/R_{ex} = 0.011$. Since τ is not varied, the fiber diameter L stays that same, and the change in Da corresponds to a change in the gas concentration. This means that the highest $\Delta R/R_0$ for PAni of this fiber diameter should be 88 and occur at 2500ppm of NH_3 exposure.

$$\left(\frac{\Delta R}{R_0} \right)_{opt, \tau=15} = \left[\left(\frac{R_0}{R_{ex}} \right)_{opt} \right]^{-1} - 1 = 88$$

$$\frac{Da_{opt}}{Da_{ref}} = \frac{([\text{NH}_3]_g)_{opt}}{([\text{NH}_3]_g)_{ref}} \Rightarrow ([\text{NH}_3]_g)_{opt} = \frac{0.18}{0.036} \times 500 \text{ ppm} = 2500 \text{ ppm}$$

For the same prescribed time of $t = 60$ s, $\tau = 8.1$ and $Da = 0.069$ for 620nm PAni fibers, based on the fitted parameters.

$$\tau = \frac{tD}{L^2} = \frac{(60s)(1.3 \times 10^{-10} \text{ cm}^2 / s)}{(310 \times 10^{-7} \text{ cm})^2} = 8.1,$$

$$Da = \frac{k_f S}{D} [\text{NH}_3]_g L^2 = (4.0 \times 10^{13} \text{ m} / \text{mol}) \left(\frac{500}{10^6} \times \frac{1 \times 10^3 \text{ g} / \text{m}^3}{28 \text{ g} / \text{mol}} \right) (310 \times 10^{-9} \text{ m})^2 = 0.069 .$$

The optimum at this τ is read from the modeling results to be at $Da = 0.50$ and $R_0/R_{ex} = 0.018$. This means that the highest $\Delta R/R_0$ ratio for PANi of this fiber diameter (620nm) should be 55 at 3600ppm of NH_3 exposure.

$$\left(\frac{\Delta R}{R_0} \right)_{opt, \tau=8} = \left[\left(\frac{R_0}{R_{ex}} \right)_{opt} \right]^{-1} - 1 = (0.018)^{-1} - 1 = 55$$

$$\frac{Da_{opt}}{Da_{ref}} = \frac{([\text{NH}_3]_g)_{opt}}{([\text{NH}_3]_g)_{ref}} \Rightarrow ([\text{NH}_3]_g)_{opt} = \frac{0.50}{0.069} \times 500 \text{ ppm} = 3600 \text{ ppm}$$

If one wants to optimize the fiber diameter only, by keeping both gas concentration and time constant, both τ and Da vary so the trajectory does not stay on a single contour line shown in Figure 40. Instead, the product, τDa , stays constant. In this case, reading parameter values from the modeling results show that within an allowed time frame of 60 s, the best sensing results would be obtained at $Da = 0.032$ and $\tau = 37$, where R_0/R_{ex} is read from the plot to be 0.007. This condition correlates to a fiber diameter of 150 nm, and expected to show a ratio of resistance change of $\Delta R/R_0 = 140$.

$$L_{opt} = \sqrt{\frac{Dt}{\tau}} = \sqrt{\frac{(1.3 \times 10^{-10} \text{ cm}^2 / \text{s})(60 \text{ s})}{37}} = 150 \text{ nm}$$

$$\left(\frac{\Delta R}{R_0}\right)_{opt} = \left[\left(\frac{R_0}{R_{ex}}\right)_{opt}\right]^{-1} - 1 = 140$$

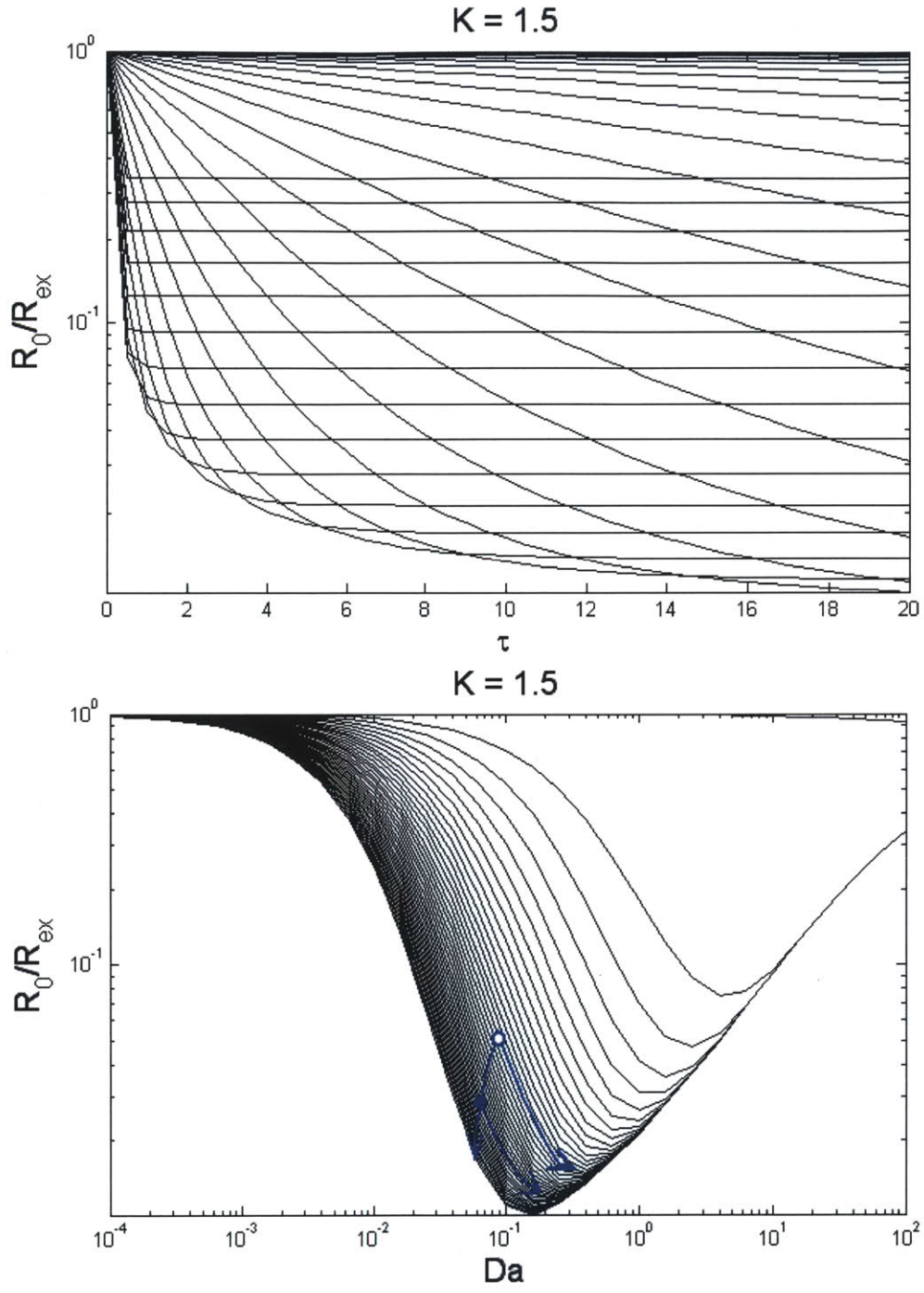


Figure 40 Reaction-diffusion model results at $K = 1.5$ using the experimental NH_3 sensing parameters; (a) a plot of resistance ratios as a function of τ for Da ranging from 10^{-4} to 10^2 ; (b) a plot of resistance ratios as a function of Da for τ ranging from 0 to 20 (increment of 0.5), the open and closed dots indicates the locations of the 620nm fiber and 450 nm fiber at $t = 60s$ respectively, and the arrows indicate the optimization directions.

6.1 Conclusions

The fiber-forming technique of electrospinning and the unique electrical characteristics of conductive polymers present a synergy where the electrospinning of conductive polymers is not only a technological challenge but also a doorway to produce potentially better materials for a variety of applications such as chemiresistive gas sensing.

To test the processing-structure-property relationship of electrospun conductive polymer fibers, we have first developed a reliable method to characterize fiber conductivity using IDE with contact-resistance corrections, and applied to electrospun conductive polymer nanofibers. This method was shown to be reliable and sensitive, as opposed to some of the other methods that have been reported in literature.

Facing with the challenge of overcoming the relatively low elasticity of the conductive polymer solutions to achieve electrospinnability, we have fabricated electrospun fibers of PANi and PEDOT, blended with PEO or PMMA over a range of compositions. One of the major contributions of this work was the successful fabrication of pure PANi/HCSA fibers by co-axial electrospinning and subsequent removal of the PMMA shell by dissolution. This allowed for the pure electrospun PANi fibers to be tested for electrical performances and its enhancement as well as gas sensing application.

The conductivities of the PANi-blend fibers are found to increase exponentially with the weight percent of doped PANi in the fibers, to as high as 50 ± 30 S/cm for as-electrospun fibers of 100% PANi/HCSA. This fiber conductivity of the pure doped PANi fibers was found to increase to 130 ± 40 S/cm with increasing molecular orientation, achieved through solid state drawing. The experimental results thus support the idea that enhanced molecular alignment within electrospun fibers, both during the electrospinning process and subsequent post-treatment, contributes positively to increasing electrical conductivity of conductive polymers. Using a model that accounts for the effects of intrinsic fiber conductivity (including both composition and molecular orientation), mat porosity, and the fiber orientation distribution within the mat, calculated mat conductivities are obtained in quantitative agreement with the mat conductivities measured experimentally. This correlation, along with the reliable method of fiber conductivity measurement by IDE, presents a way to resolve some of the inconsistencies in the literature about reporting electrical conductivity values of electrospun fibers and fiber mats.

Pure PANi fibers with different levels of doping were also fabricated by co-axial electrospinning and subsequent removal of the shell by dissolution, and shown to exhibit a large range of fiber electrical conductivities ranging from $(2.0 \pm 0.6) \times 10^{-6}$ to 50 ± 30 S/cm, increasing exponentially with increasing ratio of dopant to PANi. These fibers are found to be very effective nanoscale sensors for both ammonia and nitrogen dioxide gases, thanks to this large range of available electrical conductivities. Both sensitivity and response times are shown to be excellent, with response ratios up to 58 for doped PANi sensing of NH_3 and up to more than 10^5 for NO_2 sensing by undoped PANi fibers. The characteristic times for the gas sensing are shown to be on the order of 1 to 2 minutes. We have also developed a generic time-dependent reaction-diffusion model that accounts for reaction kinetics, reaction equilibrium, and diffusivity

parameters, and show that the model can be used to extract parameters from experimental results and used to predict and optimize the gas sensing of fibers under different constraints without the need to repeat experiments under different fiber and gas conditions.

6.2 Recommendations

Based on the experience gained working with electrospinning of conductive polymers and their composites, the following recommendations for future work in this area are proposed:

1. Other than the model system of PANi and PEDOT that are explored extensively in this work, there are a whole range of other intrinsically conductive polymers that can be tested for conditions of electrospinnability; although the author expects the trends in both processing parameters and electrical performance will be similar to the model systems tested, some of them may present unique challenges in terms of both processing and electrical measurement ranges, e.g. poly(3-hexylthiophene-2,5-diyl) (P3HT); alternatively, some conductive polymers may experience crystallinity transition more readily than PANi (which showed no signs of crystallinity transition based on DSC results), and present new challenges to its processing and study of properties that way;
2. The effect of changing dopant species to the conductive polymer fibers was not explicitly tested in this work, and may be interesting to study; there are some literature reviews of the effect of dopant to common conductive polymers such as PANi, but none was tested with regards to whether the change of dopant species might affect processing conditions in electrospinning;
3. More extensive studies should be done to achieve uniform and conform conductive surface coatings on electrospun polymer fibers by various processing methods; the author

believes that this is attainable through careful control over both the materials used and the processing parameters, but it will likely be a non-trivial and challenging study to enable the processing principles to be applied universally to all systems;

4. Incorporation of nanoparticles into electrospun fibers, both as a conductive component and otherwise, have always been a challenge, due to their limited ability to be dissolved or dispersed (agglomeration) in most of the polymer solutions; if conductive or semiconducting nanoparticles can be dispersed evenly or with greater control over locations in the small electrospun fibers, it will present lots of new opportunities to study effects like percolation and clustering, and its effects on electrical, mechanical, optical and other properties of the fibers;
5. Other applications of electrospun conductive polymers, such as applications towards solar cells, batteries, supercapacitors, and other sensor types (optical, strain, etc.), can be explored with the existing conductive polymer systems, other conductive polymers or composites, and those with further functionalization.

Bibliography

- ¹ Fridrikh, S.V., J.H. Yu, M.P. Brenner, G.C. Rutledge, *Phys. Rev. Lett.* **2003**, *90*, 144502
- ² Shin, Y.M., M.M. Hohman, M.P. Brenner, G.C. Rutledge, *Appl. Phys. Lett.* **78** (2001), 1149-1151
- ³ Yu, J.H., S.V. Fridrikh, G.C. Rutledge, *Polymer* **2006**, *47*, 4789-4797
- ⁴ Theron, S.A., E. Zussman, A.L. Yarin, *Polymer* **45** (2004), 2017-2030
- ⁵ Rutledge, G.C., S.V. Fridrikh, *Adv. Drug Deliv. Reviews* **2007**, *5*, 1384-1391
- ⁶ Rutledge, G.C., S.V. Fridrikh, *Adv. Drug Deliv. Reviews* **2007**, *5*, 1384-1391
- ⁷ Wang, X.Y.; Drew, C.; Lee, S.H.; Senecal, K.J.; Kumar, J.; Sarnuelson, L.A. *Nano Lett.* **2002**, *2*, 1273-1275
- ⁸ Li D., Y. Xia, *Nano Lett.* **3** (2003), 555-560
- ⁹ Reneker, D.H., A.L. Yarin, E. Zussman, H. Xu, *Adv. Appl. Mechanics* **41** (2007), 43-195
- ¹⁰ Salgado, A.J., O.P. Coutinho, R.L.Reis, *Macromol. Biosci.* **4** (2004), 743-765
- ¹¹ Ma, M., M. Gupta, Z. Li, L. Zhai, K.K. Gleason, R.E. Cohen, M.F. Rubner, G.C. Rutledge, *Adv. Mater.* **19** (2007), 255-259
- ¹² Reneker, D.H.; Yarin, A.L.; Zussman, E.; Xu, H. *Adv. Appl. Mechanics* **2007**, *41*, 43-195
- ¹³ Krupenkin, T.N.; Taylor, J.A.; Wang, E.N.; Kolodner, P.; Hodes, M.; Salamon, T. *Langmuir* **2007**, *23*, 9128-9133
- ¹⁴ Hoth, C.N.; Choulis, S.A.; Schilinsky, P.; Brabec, C.J. *Adv. Mater.* **2007**, *19*, 3973-3978
- ¹⁵ Schreuder-Gibson, H.L., Q. Truong, J.E. Walker, J.R. Owens, J.D. Wander, W.E. Jones, *MRS Bull.* **28** (2003), 574-578
- ¹⁶ Pai, C.L.; Boyce, M.C., Rutledge, G.C. *Polymer* **2011**, *52*, 6126-6133
- ¹⁷ Chiang, C.K., C. R. Fincher, Y. W. Park, A. J. Heeger, H. Shirakawa, E. J. Louis, S. C. Gau, A. G. McDiarmid, *Phys. Rev. Lett.*, **1977**, *39*, 1098-1101
- ¹⁸ Heeger, A.J., *Curr. Appl. Phys.* **2001**, *1*, 247-267

-
- ¹⁹ Eftekhari, A., Ed., In *Nanostructured Conductive Polymers*, Wiley: Hoboken, New Jersey, 2010
- ²⁰ Malinauskas, A., *Polymer* **2001**, *42*, 3957-3972
- ²¹ Yamazoe, N., *Sens. Actuators B*, **108** (2005), 2-14
- ²² Mueller, M., M. Fabretto, D. Evans, P. Hojati, C. Gruber, P. Murphy, *Polymer* **2012**, *53*, 2146-2151
- ²³ Zhu, Y.; Zhang, J.; Zheng, Y.; Huang, Z.; Feng, L.; Jiang, L. *Adv. Funct. Mater.* **2006**, *16*, 568-574
- ²⁴ Reneker, D.H.; Chun, I. *Nanotechnology* **1996**, *7*, 216-223
- ²⁵ Dong, H.; Nyame, V.; MacDiarmid, A.G.; Jones, W.E. *J. Polym. Sci. B* **2004**, *42*, 3934-3942
- ²⁶ Wei, M.; Lee, J.; Kang, B.; Mead, J. *Macromol. Rapid Commun.* **2005**, *26*, 1127-1132
- ²⁷ Norris, I.D.; Shaker, M.M.; Ko, F.K.; MacDiarmid, A.G. *Synth. Metals* **2000**, *114*, 109-114
- ²⁸ Fryczkowski, R., Kowalczyk, T., *Synth. Metals* **2009**, *159*, 2266-2268
- ²⁹ Wang, M.; Yu, J.H.; Kaplan, D.L.; Rutledge, G.C. *Macromolecules* **2006**, *39*, 1102-1107
- ³⁰ Skotheim, T.A.; Elsenbaumer, R.L.; Reynolds, J.R., Eds., In *Handbook of Conducting Polymers*; Marcel Dekker: New York, 1998
- ³¹ Naoi, K., K. Ueyama, T. Osaka, *J. Electrochem. Soc.* **1990**, *137*, 494-499
- ³² Kowel, S.T., G.G. Zhou, M.P. Srinivasan, P. Stroeve, B.G. Higgins, *Thin Solid Films*, **1995**, *134*, 209-215
- ³³ Yu, J.H., G.C. Rutledge, "Electrospinning," in *Encyclopedia of Polymer Science and Technology*, John Wiley & Sons Inc., 2007
- ³⁴ Reneker, D.H.; Chun, I. *Nanotechnology* **1996**, *7*, 216-223
- ³⁵ Dong, H.; Nyame, V.; MacDiarmid, A.G.; Jones, W.E. *J. Polym. Sci. B* **2004**, *42*, 3934-3942
- ³⁶ Ko, F.F.; MacDiarmid, A.G.; Norris, I.D.; Shaker, M.; Lec, R.M.. US Patent 7,264,762, Sep. 4, 2007
- ³⁷ Wei, M.; Lee, J.; Kang, B.; Mead, J. *Macromol. Rapid Commun.* **2005**, *26*, 1127-1132
- ³⁸ Aussawasathien, D.; Dong, J.H.; Dai, L. *Synth. Metals* **2005**, *154*, 37-40

-
- ³⁹ Pomfret, S.J.; Adams, P.; Comfort, N.; Monkman, A.P. *Polymer* **2000**, *41*, 2265-2269
- ⁴⁰ Shin, Y.M.; Hohman, M.M.; Brenner, M.P.; Rutledge, G.C. *Polymer* **2001**, *42*, 9955-9967
- ⁴¹ Hohman, M.M.; Shin, Y.M.; Rutledge, G.C.; Brenner, M.P. *Phys. Fluids* **2001**, *13*, 2221-2236
- ⁴² Li, D.; Wang, Y.; Xia, Y. *Nano Lett.* **2003**, *3*, 1167-1171
- ⁴³ Li, M., Y. Guo, Y. Wei, A.G. MacDiarmid, P.I. Lelkes, *Biomaterials* **2006**, *27*, 2705-2715
- ⁴⁴ Ouyang J., Q. Xu, C.W. Chu, Y. Yang, G. Li, J. Shinar, *Polymer*, **2004**, *45*, 8443-8450
- ⁴⁵ Sun, Z.C.; Zussman, E.; Yarin, A.L.; Wendroff, J.H.; Greiner, A., *Adv. Mater.* **2003**, *15*, 1929-1932
- ⁴⁶ Yu, J.H.; Fridrikh, S.V.; Rutledge, G.C. *Adv. Mater.* **2004**, *16*, 1562-1566
- ⁴⁷ Trchova, M.; Zemek, J.; Stejskal, J. *Macromolecules* **1998**, *31*, 2218–2222
- ⁴⁸ Trchova, M.; Zemek, J.; Stejskal, J. *Macromolecules* **1998**, *31*, 2218–2222
- ⁴⁹ Ma, M., Y. Mao, M. Gupta, K.K. Gleason, G.C. Rutledge, *Macromolecules* **2005**, *38*, 9742-9748
- ⁵⁰ Vaddiraju, S., K. Senecal, K.K. Gleason, *Adv. Func. Mater.* **2008**, *18*, 1929-1938
- ⁵¹ Stafstrim, S., J.L. Bredas, A.J. Epstein, H.S. Woo, D.B. Tanner, W.S. Huang, A.G. MacDiarmid, *Phys. Rev. Lett.* **1984**, *59*, 1464
- ⁵² Focke, W.W, G.E. Wnek, *J. Electroanal. Chem.* **1988**, *256*, 343-352
- ⁵³ MacDiarmid, A.G., J.C. Chiang, A.F. Richter, A.J. Epstein, *Synth. Met.*, **1986**, *18*, 285
- ⁵⁴ Mamunya, Y.P., V.V. Davydenko, P. Pissis, E.V. Lebedev, *Euro. Polymer J.* **2002**, *38*, 1887-1897
- ⁵⁵ Yu, Q.; Shi, M.; Deng, M.; Wang, M.; Chen, H., *Mat. Sci. Eng. B* **2008**, *150*, 70-76
- ⁵⁶ Trchova, M., J. Zemek, J. Stejskal, *Macromolecules* **1998**, *31*, 2218–2222
- ⁵⁷ Wang, M.; Yu, J.H.; Kaplan, D.L.; Rutledge, G.C. *Macromolecules* **2006**, *39*, 1102-1107
- ⁵⁸ Pai, C.L.; Boyce, M.C.; Rutledge, G.C. *Polymer* **2011**, *52*, 2295-2301
- ⁵⁹ Jaehne B. In *Digital Image Processing*, 6th ed.; Springer: New York, 2005

-
- ⁶⁰ Pai, C.L.; Boyce, M.C., Rutledge, G.C. *Polymer* **2011**, *52*, 6126-6133
- ⁶¹ Wang, X.Y., C. Drew, S.H. Lee, K.J. Senecal, J. Kumar, L.A. Sarnuelson, *Nano Lett.* **2002**, *2*, 1273-1275
- ⁶² Kim, I., A. Rothschild, B.H. Lee, D.Y. Kim, S.M. Jo, H.L. Tuller, *Nano Lett.* **2006**, *6*, 2009-2013
- ⁶³ Hoth, C.N., S.A. Choulis, P. Schilinsky, C.J. Brabec, *Adv. Mater.* **2007**, *19*, 3973-3978
- ⁶⁴ Kolmakov, A., Y. Zhang, G. Cheng, M. Moskovits, *Adv. Mater.* **2003**, *15*, 997-1000
- ⁶⁵ Pinto, N.J., D. Rivera, A. Melendez, I. Ramos, J.H. Lim, A.T. Johnson, *Sensors & Actuators B* **2011**, *156*, 849-853
- ⁶⁶ Shin, Y.M., M.M. Hohman, M.P. Brenner, G.C. Rutledge, *Appl. Phys. Lett.* **2001**, *78*, 1149-1151
- ⁶⁷ Tran, H.D., D. Li, R.B. Kaner, *Adv. Mater.* **2009**, *21*, 1487-1499
- ⁶⁸ Yu, J.H., S.V. Fridrikh, G.C. Rutledge, *Polymer* **2006**, *47*, 4789-4797
- ⁶⁹ Zhang, Y., G.C. Rutledge, *Macromolecules* **2012**, *45*(10), 4238-4246
- ⁷⁰ Ding, B., M. Wang, J. Yu, G. Sun, *Sensors* **2009**, *9*, 1609-1624
- ⁷¹ Volanti, D.P., A.A. Felix, M.O. Orlandi, G. Whitfield, D.J. Yang, E. Longo, H.L. Tuller, J.A. Varela, *Adv. Funct. Mater.* **2013**, *23*, 1759-1766
- ⁷² Wu, Z., X. Chen, S. Zhu, Z. Zhou, Y. Yao, W. Quan, B. Liu, *Sensors & Actuators B* **2013**, *178*, 485-493
- ⁷³ Christie, S., E. Scorsone, K. Persaud, F. Kvasnik, *Sensors & Actuators B* **2002**, *90*, 163-169
- ⁷⁴ The U.S. Environmental Protection Agency: National Ambient Air Quality Standards (NAAQS), <http://www.epa.gov/air/criteria.html>
- ⁷⁵ Liu, H., J. Kameoka, D.A. Czaplewski, H.G. Craighead, *Nano Lett.* **2004**, *4*, 671-675
- ⁷⁶ Lin, Q., Y. Li, M. Yang, *Sensors & Actuators B* **2012**, *161*, 976-982
- ⁷⁷ Kuwabata, S., C.R. Martin, *J. Membr. Sci.* **1994**, *91*, 1-12

Appendix I Electrospinning for Poly(3-hexyl-thiophene-2,5-diyl) (P3HT)

Poly(3-hexyl-thiophene-2,5-diyl) (P3HT) is an intrinsically-conductive polymer that is widely used in the photovoltaics, in conjunction with [6,6]-Phenyl C61 butyric acid methyl ester (PCBM). It is similar to the polyaniline system that has been studied, and gives a useful application in organic photovoltaics.

Lab-grade P3HT and PCBM have been purchased from American Dye Sources Inc.. The results of solubility tests are shown in Table A1. Each test was done with a 5ml solvent, adding increments of 50mg of the solute to the solvent, stirring while heating to 50 to 70°C to dissolve. From these initial results, Chloroform/DMF mixture of 5:1 proportion seems to be a reasonable starting point, and electrospinning attempts were made using it as the solvent for P3HT.

Table A1 Solubility Test Results for P3HT and PCBM

(in mg/ml)	P3HT Solubility	PCBM Solubility
Chloroform	20 ± 2	80 ± 2
DMF	10 ± 2	50 ± 2
5:1 CHCl ₃ :DMF	10 ± 2	--
THF	10 ± 2	--
<i>o</i> -Dichlorobenzene	40 ± 2	80 ± 2

Figure A1 shows the solutions made with 5:1 Chloroform/DMF solvent system. From left to right are the solution with both P3HT (2wt%) and PEO (1MDa, 4wt%); the solution with P3HT only; and the solution with PEO only. The solutions are almost black, brownish, and colorless, respectively.

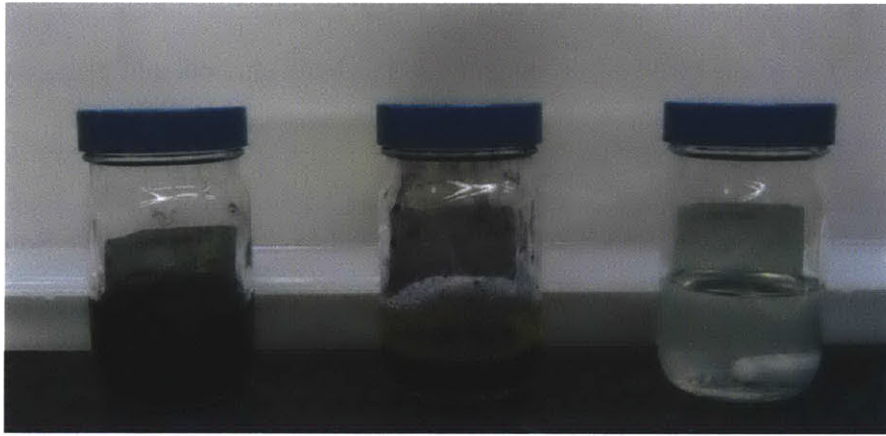


Figure A1 Solutions of P3HT and PEO in 5:1 Chloroform/DMF solvent system

When trying to electrospin the 2wt%P3HT/4wt%PEO solution, non-steady jetting was observed when the voltage was varied from 25 kV to 40kV under flow rate of 0.03 to 0.05 ml/min. The fiber collection was discontinuous and sporadic. The SEM pictures of the resulting fibers (Figure A2) show that there is a wide range of fiber diameters and the fiber diameters are relatively large (about 1 to 5 μm). The fiber surfaces are not mostly smooth, but do show small protrusions that look like particulates.

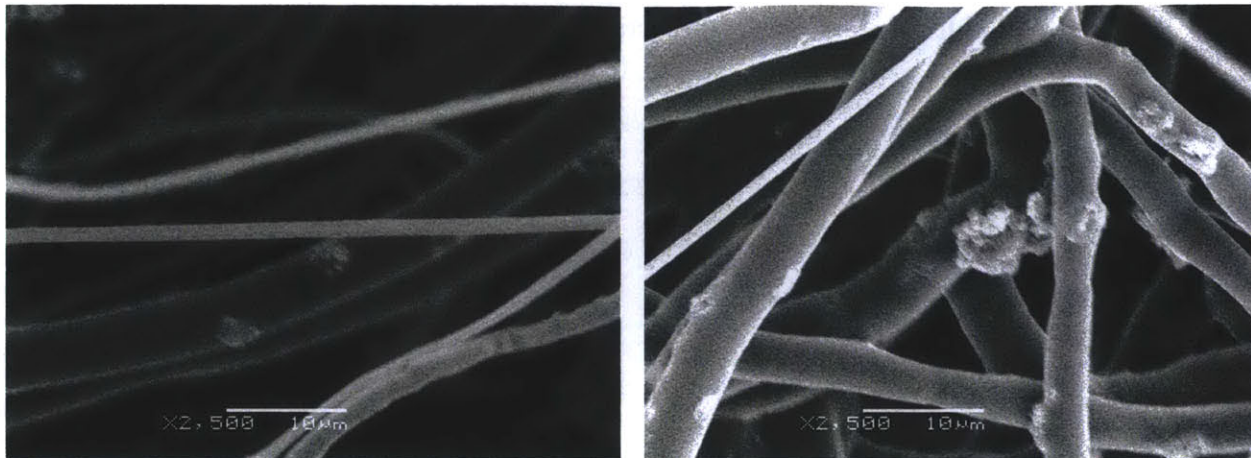


Figure A2 SEM Pictures of P3HT-PEO Blend Electrospun Fibers Made from 2wt%P3HT/4wt%PEO Solution

The conductivities of the P3HT-PEO blends have been calculated and shown in Table A2. The range of uncertainty is high in the calculated conductivities because of the wide range of fiber diameters present. Overall, the conductivity values seem quite low as compared to either the normal reported thin-film value of about 0.1 S/cm or the corresponding PANi-PEO values.

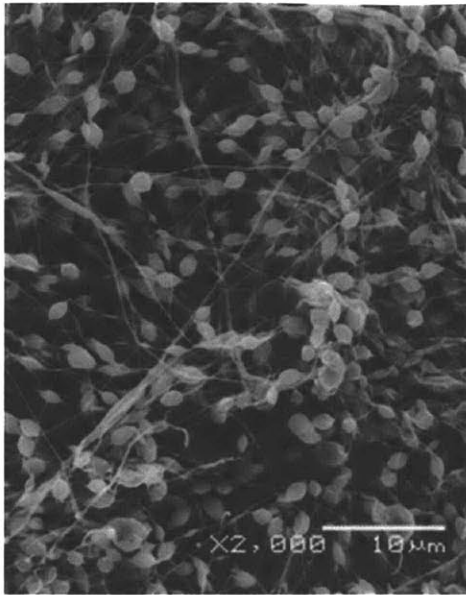
Table A2 Electrical Conductivities of P3HT-PEO Blends

Conditions	% P3HT in Solid Blend	Fiber Diameter (μm)	Electrical Conductivity (S/cm)
2 wt% P3HT, 4 wt% PEO in 5:1 C:D	33%	1.0 ~ 5.0	$4 \times 10^{-5} \sim 1 \times 10^{-3}$
1 wt% P3HT, 2 wt% PEO in 5:1 C:D	33%	1.5 ~ 5.0	$1 \times 10^{-5} \sim 1 \times 10^{-4}$
1 wt% P3HT, 4 wt% PEO in 5:1 C:D	20%	0.5 ~ 3.0	$1 \times 10^{-5} \sim 5 \times 10^{-4}$

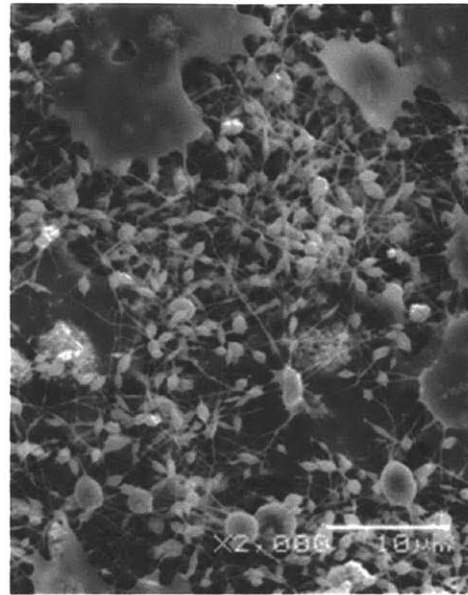
Appendix II Zinc oxide (ZnO) particle-filled Electrospun Fibers

Zinc oxide nanoparticles were purchased from NanoAmer Inc. in two batches with average diameters of 20nm and 90nm, respectively. They appeared to disperse much better in water than in DMF or chloroform, so they were blended into PEO in water solutions to be electrospun.

There was difficulty dispersing ZnO with more than 5.0% concentration in water (with constant stirring). Furthermore, even when it appeared to have dispersed in water, the resulting fiber mat showed chunks of coagulated solid under SEM (shown below) which are very likely the zinc oxide particles, as shown in Figure A3. At low ZnO loadings, though, there was no visible solid outside of the fibers in the fiber mat under SEM (e.g. the 0.5 wt% ZnO shown on the left), and the morphology looked very similar to the PEO fibers without ZnO (all beads-on-string morphology).



0.5 wt% ZnO
In 2wt% PEO in H₂O



5.0 wt% ZnO
In 2wt% PEO in H₂O

Figure A3 SEM images of electrospun PEO fibers with ZnO nanoparticles dispersed in solutions, at 0.5 wt% and 5.0 wt% respectively; scale bars = 10 μ m

Appendix III MATLAB Codes for Calculation of Orientation

Distribution and Correction Factors in Nonwoven Fiber Mats

```
function [ ] = Orientationfactor( )
% Orientationfactor: compute the average of inversed path length that
% intersect two lines.
% assumes two bars (electrodes) of length L a distance delta apart.
% path distribution function p(x, theta), x = position on first electrode
% and theta = direction of path to second electrode
%
% n = Int (from -L/2 to L/2) dx [ Int(from -pi to pi) dtheta
% (l(x,theta)*p(x,theta)) ]
% subject to constraint that
% -L/2/delta < tan(theta) + x/delta < L/2/delta

n = 50; % number of different L values
L = logspace(-1, 3, n); % length of electrodes
delta = 1; % distance between electrodes

BandNum = 61; % number of angular bands - can be varied
thetahist = orientation('c3.tiff', BandNum); % analyze image p(theta)

Q = zeros(size(L));
for k = 1 : n
    lambda = L(k)/2/delta;
    thetaLB = @(x) atan(-lambda-x/delta); % lower integration bound on theta
    thetaUB = @(x) atan(lambda-x/delta); % upper integration bound on theta
    distribFun = @(x,theta) 1./delta./L(k)./pi .* ones(size(x)) .*
thetahist(floor((theta/pi+0.5)*BandNum)) .* cos(theta);
    Q(k) = quad2d(distribFun, -lambda, lambda, thetaLB, thetaUB);
end

semilogx(L,Q,'b')
xlabel('Electrode Length L/\delta');
ylabel('Orientation correction factor \delta<1/l>');

end

function thetahistnorm = orientation(imagename, BandNum)

% orientation: Dimitrios Tzeranis, December 2007,
% curvature: J. van de Weijer, L.J. van Vliet, P.W. Verbeek, M. van Ginkel,
2001
% modified by Chia-Ling Pai, April 2011; further modified by Yuxi Zhang,
% Jan 2012
```

```

% Input image file name (string form) with the full path if not in current
folder

LPBlockSize = 11; sigma_g = 11; sigma_a = 35; pixsize=256;

% read image
RawFrame = imread(imagename);
RawFrame = rgb2gray(RawFrame);

RawFrame = imresize(RawFrame, [512,512]); RawFrame = RawFrame(:,:);
RawFrame = imresize(RawFrame, [pixsize,pixsize]);
RawFrame = imadjust(RawFrame); RawFrame = double(RawFrame);

PhotonC = double(RawFrame)/double(max(max(RawFrame)));
PhotonC2 = reshape(PhotonC,1,pixsize^2);

% % % ==> local orientation analysis
Hx = [3,0,-3;10,0,-10;3,0,-3]/32;
Ax = imfilter(RawFrame,Hx,'replicate'); Ay =
imfilter(RawFrame,Hx','replicate');
Axx = Ax.*Ax; Ayy = Ay.*Ay; Axy = Ax.*Ay;
Jxx = imfilter(Axx,fspecial('average',LPBlockSize),'replicate');
Jyy = imfilter(Ayy,fspecial('average',LPBlockSize),'replicate');
Jxy = imfilter(Axy,fspecial('average',LPBlockSize),'replicate');

c = sqrt((Jyy - Jxx).^2 + 4*Jxy.^2)./(Jxx + Jyy); % confidence function
c2 = reshape(c,1,pixsize^2); % value falls within 0 to 1
chist = hist(c2,linspace(0,1,20));

% initialize the filter
break_of_sigma = 3; filtersize = break_of_sigma*sigma_g;
% compute the Gaussian and first Gaussian derivatives at scale sigma_g for
orientation
    % compute the Gaussian and first Gaussian derivatives at scale sigma_g
    [y x] = ndgrid(-filtersize:filtersize,-filtersize:filtersize);
    Gg      = 1/(2 * pi * sigma_g^2)* exp(-(x.^2 + y.^2)/(-2 * sigma_g *
sigma_g) );
    Gg_x    = 1/(sigma_g^2)* x .* Gg; Gg_y    = 1/(sigma_g^2)* y .* Gg;

    % Compute the (moment generating) filters at scale sigma_a
    filtersize = break_of_sigma*sigma_a;
    [y x] = ndgrid(-filtersize:filtersize,-filtersize:filtersize);
    Ga      = 1/(2 * pi * sigma_a^2) * exp(-(x.^2 + y.^2)/(-2 * sigma_a *
sigma_a));
    Ga_x    = x .* Ga; Ga_y    = y .* Ga;
    Ga_xy   = x .* Ga_y; Ga_xx = x .* Ga_x; Ga_yy = y .* Ga_y;

% orientation_imation Estimation

```

```

Fx = imfilter(RawFrame, Gg_x, 'replicate'); Fy = imfilter(RawFrame,
Gg_y, 'replicate');
Fxx = Fx .* Fx; Fxy = Fx .* Fy; Fyy = Fy .* Fy;

% theta values from J (gradient angle)
orientation_im = 1/2 * atan2(2 * imfilter(Fxy, Ga, 'replicate'), imfilter((Fxx
- Fyy), Ga, 'replicate'));
orientation_im2 = reshape(orientation_im, 1, pixsize^2);

% theta values from DT (gradient angle)
theta = atan2(2*Jxy, -Jyy+Jxx)/2; % I change the sign of Jyy and Jxx from DT,
it means gradient now
theta2 = reshape(theta, 1, pixsize^2);

% magnitude of orientation vector
% BandNum = 61;
mag = sqrt(double((2*Jxy).^2) + double((Jyy-Jxx).^2));
mag2 = reshape(mag, 1, pixsize^2); MaxMag = max(mag2);
mag2 = mag2/MaxMag; % the value falls within 0 to 1
maghist = hist(mag2, linspace(1/BandNum/2, 1-1/BandNum/2, BandNum));

HsvImage = ones(pixsize, pixsize, 3);
HsvImage(:, :, 1) = (theta + pi/2)/pi;
HsvImage(:, :, 3) =
double(PhotonC)/double(max(max(PhotonC))) .* mag/max(max(mag));
RgbImage = hsv2rgb(HsvImage);

HsvImage(:, :, 1) = (orientation_im + pi/2)/pi;

Mask1 = PhotonC2>0.1; Mask2 = mag2>0.1;
Mask3 = PhotonC>0.1; Mask4 = mag>0.1;
theta2(~(Mask1&Mask2)) = [];
orientation_im2(~(Mask1&Mask2)) = [];
orientation_im = Mask3.*orientation_im; orientation_im =
Mask4.*orientation_im;
thetahist = hist(theta2, linspace(-pi/2+pi/BandNum/2, pi/2-
pi/BandNum/2, BandNum));
thetahistnorm = thetahist ./ (sum(thetahist));
orientation_im_hist = hist(orientation_im2, linspace(-pi/2+pi/BandNum/2, pi/2-
pi/BandNum/2, BandNum));

% plots the distribution
bar(linspace(-pi/2, pi/2, BandNum)/pi*180, orientation_im_hist);

xlim([-90 90]); ylim([0 12000]); xlabel('fiber orientation (^o)');
ylabel('counts');

end

```


Appendix IV Derivation of System of Non-dimensionalized Partial Differential Equations for Reaction-Diffusion Model

Start with the original set of PDE's:

$$\frac{\partial C_{\ominus}}{\partial t} = \frac{D}{r'} \frac{\partial}{\partial r'} \left(r' \frac{\partial C_{\ominus}}{\partial r'} \right) - k_f C_{\ominus} C_{\Phi} + k_r C_{\Omega} C_{\Psi} \quad (1)$$

$$\frac{\partial C_{\Phi}}{\partial t} = -k_f C_{\ominus} C_{\Phi} + k_r C_{\Omega} C_{\Psi} \quad (2)$$

$$\frac{\partial C_{\Omega}}{\partial t} = k_f C_{\ominus} C_{\Phi} - k_r C_{\Omega} C_{\Psi} \quad (3)$$

$$\frac{\partial C_{\Psi}}{\partial t} = k_f C_{\ominus} C_{\Phi} - k_r C_{\Omega} C_{\Psi} \quad (4)$$

Non-dimensionalize radius: (r' is the original radius, r the non-dimensionalized one)

$$r = \frac{r'}{L} \quad r' = rL$$

and use equilibrium constant definition

$$K = \frac{k_f}{k_r} \quad k_r = \frac{k_f}{K}$$

Substitute in for r' and k_r , so that

$$\frac{\partial C_{\ominus}}{\partial t} = \frac{D}{L^2 r} \frac{\partial}{\partial r} \left(r \frac{\partial C_{\ominus}}{\partial r} \right) - k_f C_{\ominus} C_{\Phi} + \frac{k_f}{K} C_{\Omega} C_{\Psi} \quad (5)$$

$$\frac{\partial C_{\Phi}}{\partial t} = -k_f C_{\ominus} C_{\Phi} + \frac{k_f}{K} C_{\Omega} C_{\Psi} \quad (6)$$

$$\frac{\partial C_{\Omega}}{\partial t} = k_f C_{\ominus} C_{\Phi} - \frac{k_f}{K} C_{\Omega} C_{\Psi} \quad (7)$$

$$\frac{\partial C_{\Psi}}{\partial t} = k_f C_{\ominus} C_{\Phi} - \frac{k_f}{K} C_{\Omega} C_{\Psi} \quad (8)$$

Non-dimensionalize time by diffusion time constant:

$$\tau = \frac{t}{t_D} = \frac{tD}{L^2} \quad t = \frac{\tau L^2}{D}$$

Replace time and multiplies by $\frac{L^2}{D}$ on both sides of all equations:

$$\frac{\partial C_{\ominus}}{\partial \tau} = \frac{1}{r} \frac{\partial}{\partial r} \left(r \frac{\partial C_{\ominus}}{\partial r} \right) - \frac{L^2}{D} k_f C_{\ominus} C_{\Phi} + \frac{L^2}{D} \frac{k_f}{K} C_{\Omega} C_{\Psi} \quad (9)$$

$$\frac{\partial C_{\Phi}}{\partial \tau} = -\frac{L^2}{D} k_f C_{\ominus} C_{\Phi} + \frac{L^2}{D} \frac{k_f}{K} C_{\Omega} C_{\Psi} \quad (10)$$

$$\frac{\partial C_{\Omega}}{\partial \tau} = \frac{L^2}{D} k_f C_{\Theta} C_{\Phi} - \frac{L^2 k_f}{D K} C_{\Omega} C_{\Psi} \quad (11)$$

$$\frac{\partial C_{\Psi}}{\partial \tau} = \frac{L^2}{D} k_f C_{\Theta} C_{\Phi} - \frac{L^2 k_f}{D K} C_{\Omega} C_{\Psi} \quad (12)$$

Non-dimensionalize all concentrations

$$\Theta = \frac{C_{\Theta}}{C_{o,\Theta}} \quad \Phi = \frac{C_{\Phi}}{C_{o,\Phi}} \quad \Omega = \frac{C_{\Omega}}{C_{o,\Omega}} \quad \Psi = \frac{C_{\Psi}}{C_{o,\Psi}}$$

$$C_{o,\Theta} \frac{\partial \Theta}{\partial \tau} = \frac{1}{r} \frac{\partial}{\partial r} \left(r \frac{\partial \Theta}{\partial r} C_{o,\Theta} \right) - \frac{L^2}{D} k_f C_{o,\Theta} C_{o,\Phi} \Theta \Phi + \frac{L^2 k_f}{D K} C_{o,\Omega} C_{o,\Psi} \Omega \Psi \quad (13)$$

$$C_{o,\Phi} \frac{\partial \Phi}{\partial \tau} = -\frac{L^2}{D} k_f C_{o,\Theta} C_{o,\Phi} \Theta \Phi + \frac{L^2 k_f}{D K} C_{o,\Omega} C_{o,\Psi} \Omega \Psi \quad (14)$$

$$C_{o,\Omega} \frac{\partial \Omega}{\partial \tau} = \frac{L^2}{D} k_f C_{o,\Theta} C_{o,\Phi} \Theta \Phi - \frac{L^2 k_f}{D K} C_{o,\Omega} C_{o,\Psi} \Omega \Psi \quad (15)$$

$$C_{o,\Psi} \frac{\partial \Psi}{\partial \tau} = \frac{L^2}{D} k_f C_{o,\Theta} C_{o,\Phi} \Theta \Phi - \frac{L^2 k_f}{D K} C_{o,\Omega} C_{o,\Psi} \Omega \Psi \quad (16)$$

Set reference concentrations of Ψ the same as that of Φ , i.e., $C_{o,\Psi} = C_{o,\Phi}$, (as they are the polymeric reactant and product and have stoichiometric ratio of 1), divide all equations by $C_{o,\Phi}$ on both sides,

$$\frac{C_{o,\Theta}}{C_{o,\Phi}} \frac{\partial \Theta}{\partial \tau} = \frac{C_{o,\Theta}}{C_{o,\Phi}} \frac{1}{r} \frac{\partial}{\partial r} \left(r \frac{\partial \Theta}{\partial r} \right) - \frac{L^2}{D} k_f C_{o,\Theta} \Theta \Phi + \frac{L^2}{D} \frac{k_f}{K} C_{o,\Omega} \Omega \Psi \quad (17)$$

$$\frac{\partial \Phi}{\partial \tau} = -\frac{L^2 k_f}{D} C_{o,\Theta} \Theta \Phi + \frac{L^2 k_f}{DK} C_{o,\Omega} \Omega \Psi \quad (18)$$

$$\frac{C_{o,\Omega}}{C_{o,\Phi}} \frac{\partial \Omega}{\partial \tau} = \frac{L^2}{D} k_f C_{o,\Theta} \Theta \Phi - \frac{L^2}{D} \frac{k_f}{K} C_{o,\Omega} \Omega \Psi \quad (19)$$

$$\frac{\partial \Psi}{\partial \tau} = \frac{L^2}{D} k_f C_{o,\Theta} \Theta \Phi - \frac{L^2}{D} \frac{k_f}{K} C_{o,\Omega} \Omega \Psi \quad (20)$$

Define Damköhler number with respect to the forward reaction and reference concentration of Θ ,

$$\text{Da} = \frac{k_f C_{o,\Theta} L^2}{D}, \text{ and let the ratios of reference concentrations be } \alpha = \frac{C_{o,\Phi}}{C_{o,\Theta}} \text{ and } \beta = \frac{C_{o,\Phi}}{C_{o,\Omega}},$$

$$\frac{1}{\alpha} \frac{\partial \Theta}{\partial \tau} = \frac{1}{\alpha} \frac{1}{r} \frac{\partial}{\partial r} \left(r \frac{\partial \Theta}{\partial r} \right) - \text{Da} \Theta \Phi + \frac{\text{Da}}{K} \frac{\alpha}{\beta} \Omega \Psi \quad (21)$$

$$\frac{\partial \Phi}{\partial \tau} = -\text{Da} \Theta \Phi + \frac{\text{Da}}{K} \frac{\alpha}{\beta} \Omega \Psi \quad (22)$$

$$\frac{1}{\beta} \frac{\partial \Omega}{\partial \tau} = \text{Da} \Theta \Phi - \frac{\text{Da}}{K} \frac{\alpha}{\beta} \Omega \Psi \quad (23)$$

$$\frac{\partial \Psi}{\partial \tau} = \text{Da} \Theta \Phi - \frac{\text{Da}}{K} \frac{\alpha}{\beta} \Omega \Psi \quad (24)$$

Further set the reference concentrations of the small molecular reactant and product to be the same, so that $\alpha = \beta$,

$$\frac{\partial \Theta}{\partial \tau} = \frac{1}{r} \frac{\partial}{\partial r} \left(r \frac{\partial \Theta}{\partial r} \right) + \alpha \left[-\text{Da} \Theta \Phi + \frac{\text{Da}}{K} \Omega \Psi \right] \quad (25)$$

$$\frac{\partial \Phi}{\partial \tau} = -\text{Da} \Theta \Phi + \frac{\text{Da}}{K} \Omega \Psi \quad (26)$$

$$\frac{\partial \Omega}{\partial \tau} = \alpha \left[\text{Da} \Theta \Phi - \frac{\text{Da}}{K} \Omega \Psi \right] \quad (27)$$

$$\frac{\partial \Psi}{\partial \tau} = \text{Da} \Theta \Phi - \frac{\text{Da}}{K} \Omega \Psi \quad (28)$$

Appendix V MATLAB Code for the Reaction-Diffusion Model

System

```
function RxnDiffModel
% No input or output variables.

Karray = [inf 100 1 0.1];
N = 31; % Number of discretized Da points
Da_array = logspace(-4, 2, N)';
tau_array = linspace(0.001, 100, 21); % Target tau values

Nr = 20; % Number of points in r direction

Theta = zeros(length(Da_array), length(tau_array), Nr); %initialize
Phi = zeros(length(Da_array), length(tau_array), Nr);
Omega = zeros(length(Da_array), length(tau_array), Nr);
Psi = zeros(length(Da_array), length(tau_array), Nr);

C_initial = zeros(4*Nr,1) ;
C_initial(Nr) = 1;
C_initial(Nr+1:2*Nr) = 1; % initial conditions
C_initial(2*Nr+1:3*Nr) = 0;
C_initial(3*Nr+1:4*Nr) = 0;

for l = 1 : length(Karray)
    K = Karray(l);

    figure
    for j = 1 : N
        Da = Da_array(j);

        for k = 1 : length(tau_array)
            [t,C] = odel5s(@(t,C) RxnDiff_PDE(t,C,Da,K,alpha), [0
tau_array(k)], C_initial);
            Theta(j,k,:) = C(length(t),1:Nr);
            Phi(j,k,:) = C(length(t),Nr+1:2*Nr);
            Omega(j,k,:) = C(length(t),2*Nr+1:3*Nr);
            Psi(j,k,:) = C(length(t),3*Nr+1:4*Nr);
        end
    end

    [X,Y] = meshgrid(tau_array, Da_array);
    surf(X, Y, RoR)
    %hold on;
    %contour3(X, Y, RoR)
```

```

        ylabel('Da');
        xlabel('\tau'); xlim([0 100]); zlim([0 1]); zlabel('R_0/R_f');
        title(['K = ' num2str(K)]);
        shading interp
        set(gca,'yscale','log')
        colormap autumn
    end
end

%%%%%%%%%%%%%%%%%%%%%%%%%%%%%%%%%%%%%%%%%%%%%%%%%%%%%%%%%%%%%%%%%%%%%%%%

%%%%%%%%%%%%%%%%%%%%%%%%%%%%%%%%%%%%%%%%%%%%%%%%%%%%%%%%%%%%%%%%%%%%%%%%
function dCdt = RxnDiff_PDE(t, C, Da, K, alpha)
% Describes the system of ODE's
%
% Input Variables:
%     t           time vector, tau in nondimensional form
%     C           vector of concentrations
%
% Output Variables:
%     dCdt        vector of time derivatives of C
%
dCdt = zeros(size(C));      % Initialize
Nr = length(C)/4;
delr = 1/(Nr-1);
r = linspace(0,1,Nr);

dCdt(1) = (4/3*C(1)-1/3*C(2) - 2*C(1) + C(2)) / (delr^2) + alpha*(-
Da*C(1)*C(Nr+1) + Da/K*C(2*Nr+1)*C(3*Nr+1));
dCdt(Nr) = (1 - 2*C(Nr) + C(Nr-1)) / (delr^2) + (1 - C(Nr-1)) /2/delr +
alpha*(- Da*C(Nr)*C(2*Nr) + Da/K*C(3*Nr)*C(4*Nr));

for j = 2 : Nr-1
    dCdt(j) = (C(j+1) - 2*C(j) + C(j-1)) / (delr^2) + (C(j+1) - C(j-1))
/2/delr + alpha*(- Da*C(j)*C(Nr+j) + Da/K*C(2*Nr+j)*C(3*Nr+j));
end

for j = 1 : Nr
    dCdt(Nr+j) = - Da*C(j)*C(Nr+j) + Da/K*C(2*Nr+j)*C(3*Nr+j);
    dCdt(2*Nr+j) = alpha * (Da*C(j)*C(Nr+j) - Da/K*C(2*Nr+j)*C(3*Nr+j));
    dCdt(3*Nr+j) = Da*C(j)*C(Nr+j) - Da/K*C(2*Nr+j)*C(3*Nr+j);
end

end

```